



ELSEVIER

Contents lists available at ScienceDirect

## Progress in Materials Science

journal homepage: [www.elsevier.com/locate/pmatsci](http://www.elsevier.com/locate/pmatsci)

## Electric field-induced transformations in bismuth sodium titanate-based materials

Giuseppe Viola<sup>a,\*</sup>, Ye Tian<sup>b</sup>, Chuying Yu<sup>c</sup>, Yongqiang Tan<sup>d</sup>, Vladimir Koval<sup>e</sup>, Xiaoyong Wei<sup>f</sup>, Kwang-Leong Choy<sup>a,\*</sup>, Haixue Yan<sup>g,\*</sup>

<sup>a</sup> Institute for Materials Discovery, University College London, Malet Place, London WC1E 7JE, UK

<sup>b</sup> School of Materials Science & Engineering, Shaanxi University of Science & Technology, Xi'an 710021, China

<sup>c</sup> College of Materials Science and Engineering, Hunan University, Changsha 410082, China

<sup>d</sup> Innovation Research Team for Advanced Ceramics, Institute of Nuclear Physics and Chemistry, China Academy of Engineering Physics, Mianyang 621900, China

<sup>e</sup> Institute of Materials Research, Slovak Academy of Sciences, Watsonova 47, 040 01 Kosice, Slovakia

<sup>f</sup> Electronic Materials Research Laboratory, Key Laboratory of the Ministry of Education & International Center for Dielectric Research, School of Electronic Science and Engineering, Faculty of Electronic and Information Engineering, Xi'an Jiaotong University, Xi'an 710049, China

<sup>g</sup> School of Engineering and Materials Science, Queen Mary University of London, E1 4NS London, UK

### ARTICLE INFO

#### Keywords:

Bismuth-sodium titanate  
Electric field-induced transformations  
Lead-free perovskites

### ABSTRACT

Electric field-induced transformations occur in a myriad of systems with a variegated phenomenology and have attracted widespread scientific interest due to their importance in many applications. The present review focuses on the electric field-induced transformations occurring in bismuth sodium titanate (BNT)-based materials, which are considered an important family of lead-free perovskites and represent possible alternatives to lead-based compounds for several applications. BNT-based systems are generally classified as relaxor ferroelectrics and are characterized by complex structures undergoing various electric field-driven phenomena. In this review, changes in crystal structure symmetry, domain configuration and macroscopic properties are discussed in relation to composition, temperature and electrical loading characteristics, including amplitude, frequency and DC biases. The coupling mechanisms between octahedral tilting with polarization and strain, and other microstructural features are identified as important factors mediating the local and overall electric field-induced response. The role of field-induced transformations on electrical fatigue is discussed by highlighting the effects of ergodicity on domain evolution and fatigue resistance in bipolar and unipolar cycles. The relevance of field-induced transformations in key applications, including energy storage capacitors, actuators, electrocaloric systems and photoluminescent devices is comprehensively discussed to identify materials design criteria. The review is concluded with an outlook for future research.

\* Corresponding authors.

E-mail addresses: [g.viola@ucl.ac.uk](mailto:g.viola@ucl.ac.uk) (G. Viola), [k.choy@ucl.ac.uk](mailto:k.choy@ucl.ac.uk) (K.-L. Choy), [h.x.yan@qmul.ac.uk](mailto:h.x.yan@qmul.ac.uk) (H. Yan).

<https://doi.org/10.1016/j.pmatsci.2021.100837>

Received 18 January 2021; Received in revised form 22 June 2021; Accepted 22 June 2021

## 1. Introduction

### 1.1. Definition

The notion of “electric field-induced transformations” (EFITs) indicates the whole variety of processes that can be induced by the application of static and/or dynamic electric fields in a wide range of material systems. These phenomena can occur via different mechanisms that are active at various scales and can be triggered by electric fields of different magnitudes depending on the characteristic thresholds existing in the respective systems.

### 1.2. Overview of electric field-induced transformations in different systems.

Electric field-induced transformations have been observed in crystalline materials of various bulk forms, such as single crystals, polycrystals, thin films and heterostructures [1,2], as well as in nanostructured systems, including nanotubes [3], nanosheets [4], nanorods [5], nanowires [6] and nanodots [7]. Additionally, EFITs have been detected in glass-like phases [8,9], liquid crystals [10], as well as gels [11], plasmas [12], electrorheological fluids [13], liquids [14], suspensions [15] and biological systems [16]. EFITs manifest themselves with a very rich phenomenology and widely diversified features, depending on the particular systems in which they take place.

The underlying mechanisms of EFITs include different physical phenomena that can occur at the atomic and molecular scale, and can be often associated with: (i) atom and ion displacements; (ii) alterations of chemical bonds; and (iii) phonon instabilities, as examples of key mechanisms. These microscopic processes produce measurable effects at larger scales, as evidenced by the observation of crystal structure modifications, morphological changes at the mesoscale, macroscopic volumetric variations, and modifications of various physical and chemical properties.

EFITs attract considerable research interests, not only from an academic perspective, but also from a technological standpoint for their significant implications in different fields of applications. For instance, EFITs could be driven to stabilize a particular phase during processing [17,18], to generate oriented microstructures with anisotropic properties [19–21], to control crystallization processes [18,22] and to manipulate wetting properties of solid–liquid interfaces [23]. Moreover, as reported in a number of previous reviews, EFITs in electro-active materials can be suited to engineer various types of devices, including energy storage capacitors [24–26], strain actuators [27–29] and electrocaloric solid refrigerants [30].

Due to the broad range of phenomena that EFITs entail, it is opportune to review the most important aspects of the electric field-induced processes that take place in systems of technological relevance. In this context, the main attention is focused on EFITs occurring in electroceramics, with particular interest in important prototypes of lead-free perovskites.

### 1.3. Electric field-induced transformations in electroceramics

The notion of “electroceramics” here refers to all polycrystalline ceramics, thin films and single crystals that experience different types of electric field-induced processes and exhibit specific responses under the application of an electric field. These phenomena include: (i) dipole reorientation (occurring in dielectrics) [31]; (ii) domain wall motion and domain switching (fundamental characteristics of ferroelectrics) [32]; (iii) reorientation/growth of polar nanoregions (in relaxor ferroelectrics) [33]; tunability of dielectric permittivity (observed in ferroelectrics and relaxor ferroelectrics) [34]; (iv) colossal electroresistance (observed in several manganites) [35]; (v) magnetoelectric coupling (observed in magnetoelectric materials) [36]. Besides, various electroceramics experience modifications of the crystal structure when subjected to external electric fields, as observed in ferroelectric, relaxor and antiferroelectric systems.

The general effect of an electric field applied to a dielectric material is to induce a polar order via the alignment of electric dipoles along the direction of the applied field [37]. In the particular case of ferroelectrics, the electric field forces the polarization vectors in different domains to align along the electric field direction, leading to a macroscopic net polarization. A remnant polarization state persists after removing the applied field, yielding piezoelectric activity [37]. Additionally, in some ferroelectric materials, the electric field can also induce changes in the crystal structure, as, for instance, revealed in the case of BaTiO<sub>3</sub>-based materials [38–40]. In the case of relaxors under electrical loading, the polarization vectors of polar nanoregions (PNRs) align along the external field, and the size of the PNRs increases when the applied field exceeds specific characteristic threshold values [37], which vary in different systems. These processes can be reversible or irreversible, as generally verified for the case of ergodic or non-ergodic relaxors, respectively. Similar to ferroelectrics, relaxors can also experience structural transformations under electrical loading [41]. For the case of anti-ferroelectrics (AFE), it is well known that several AFE materials experience EFITs from the antiferroelectric to the ferroelectric state [42]. These transformations lead to characteristic double electric displacement (D)/polarization (P)-electric field (E) hysteresis loops, as observed in various AFE-like systems, such as PbZrO<sub>3</sub>- [42] and AgNbO<sub>3</sub>-based ceramics [42–48]. Irreversible structural changes and a progressive increase of polarization and strain upon electric field cycling, known as “wake-up behavior”, have been observed in various rare earth-modified BiFeO<sub>3</sub> ceramics, some of which are also regarded as AFE-like systems [49–51]. It is often the case where changes in the crystal structure and polarization reorientation during electrical loading are superimposed, and it is difficult to separate their contributions to the macroscopic behavior. This makes the entire phenomenology highly fascinating and has triggered the motivation for compiling the present review.

### 1.4. Scope and structure of this review

The main purpose of this review is to summarize and categorize the existing knowledge of a series of electric field-induced phenomena reported for the most widely studied relaxor ferroelectric systems over the last decade, namely  $\text{Bi}_{0.5}\text{Na}_{0.5}\text{TiO}_3$ -based materials. This would provide a general understanding of the electric field-driven transformations experienced by these materials and allow more precise interpretations of their behaviour to ultimately improve their performance for a variety of applications.

The present review is organized as follows. The initial part is dedicated to  $\text{Bi}_{0.5}\text{Na}_{0.5}\text{TiO}_3$  (BNT) with a detailed review of the fabrication process, crystal structure, dielectric properties and electric field-induced transitions. Thereafter, a series of electric field-induced phenomena observed in different BNT-based systems are discussed to provide a broader view of the entire phenomenology of EFITs occurring in this materials class.

## 2. Bismuth-Sodium titanate

### 2.1. Generalities of $\text{Bi}_{0.5}\text{Na}_{0.5}\text{TiO}_3$

Bismuth-sodium titanate was discovered at the beginning of the '60s by Smolenskii and co-workers [52], and it is still drawing significant research interest for various types of applications.

Although the understanding of the electrical behaviour of BNT is still incomplete, there is a general consensus that BNT undergoes electric field-induced transitions that result in the stabilization of a ferroelectric state characterized by a large remnant polarization (over  $35 \mu\text{C}/\text{cm}^2$ ) and a large coercive field (over  $70 \text{ kV}/\text{cm}$ ) [53].

In principle, BNT can exhibit competitive properties with lead-based ferroelectrics, but various obstacles have limited its widespread in piezoelectric applications. The main inconveniences are represented by the difficulty of poling and the low piezoelectric constants [54]. Both issues are related to various reasons, including: (i) increased leakage currents related to the stoichiometry imbalance possibly arising from the evaporation of volatile elements during processing; (ii) low breakdown strength in poorly sintered ceramics; (iii) high coercive field. These drawbacks can be reduced and eventually avoided by choosing appropriate processing conditions that would produce BNT with the desired high density and stoichiometric integrity.

#### 2.1.1. General effects of the processing methods

Bismuth sodium titanate ceramics can be fabricated using different processing techniques, with remarkable effects on structure and properties. The most common powder synthesis method is based on the solid-state process through a reaction between  $\text{Bi}_2\text{O}_3$ ,  $\text{Na}_2\text{O}$  and  $\text{TiO}_2$  weighed in appropriate stoichiometric amounts, according to the ternary phase diagram initially outlined by Uchida and Kikuchi [55] and subsequently updated by Spreitzer et al. [56], as shown in Fig. 1.

Other powder preparation techniques are based on chemical methods, including sol-gel [57–63], hydrothermal [64–66], stearic acid gel [67] and combustion synthesis [68]. A systematic study on the effects of the processing route has been reported by Cilaveni et al., who compared structure, microstructure and properties of ceramics prepared using powders obtained via solid-state reaction, sol-gel, hydrothermal and combustion methods [69]. All ceramics were sintered at  $1150^\circ\text{C}$  for 3 h in air; these conditions enabled achieving about 95% relative density and prevented severe stoichiometry imbalance, according to the energy dispersive spectroscopy analysis [69]. It was found that BNT ceramics produced by solid-state reaction showed pure rhombohedral structure  $R3c$ , while ceramics fabricated using

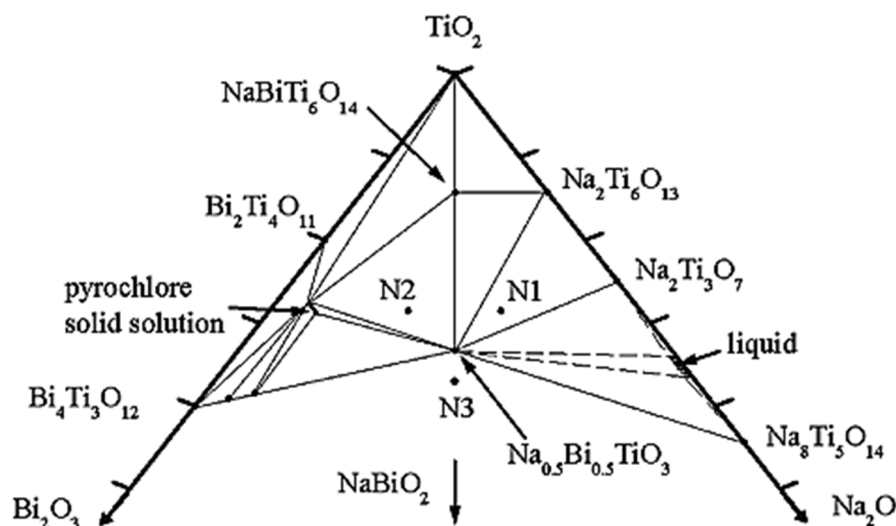


Fig. 1. Equilibrium phases in the ternary phase diagram of  $\text{Bi}_2\text{O}_3$ - $\text{Na}_2\text{O}$ - $\text{TiO}_2$  at  $1000^\circ\text{C}$ . N1, N2 and N3 correspond to bismuth-, sodium- and titanium-deficient compositions with respect to the stoichiometric  $\text{Na}_{0.5}\text{Bi}_{0.5}\text{TiO}_3$ . [Reproduced with permission from Ref. [56] Copyright 2007 Royal Society of Chemistry].

sol-gel, hydrothermal and combustion techniques, showed minor presence of the monoclinic structure Cc, coexisting with the rhombohedral phase [69]. The solid-state reaction route determined the largest crystallite size (43.3 nm), followed by the ceramics obtained by the combustion and sol-gel routes with fairly similar crystallite size (estimated as 38.8 nm in both cases), and those produced by the hydrothermal method that had the smallest crystallite size (33.6 nm). A similar trend was found for the grain size, which ranged from 5.6  $\mu\text{m}$  (in ceramics prepared by solid-state reaction) to 1  $\mu\text{m}$  (in ceramics prepared by hydrothermal method) [69]. Dielectric and ferroelectric properties were also found to be significantly affected by the processing route [69]. In particular, the variation of the coercive field did not follow the expected dependence on grain size (decreasing with increasing grain size), suggesting that other mechanisms have contributed to the observed variations. The ceramics fabricated by the hydrothermal method showed relaxor-like features, with more slanted polarization–electric field hysteresis loops, lower coercive field and more diffuse dielectric peak [69].

Based on these observations, it could be concluded that alterations of the crystal structure, microstructure and electrical properties are not only due to the morphology of domains, crystallites and grains, but also to possible disruption of the nominal stoichiometry emerging during processing.

### 2.1.2. General effects of stoichiometry imbalance

The stoichiometric balance is particularly important to obtain reliable properties and it can be eventually preserved by better understanding the effect of raw materials on the kinetics of the chemical reactions occurring during the chosen processing route. Stoichiometry imbalance could be avoided by taking into account the hygroscopic behaviour of some precursors and the effects of the processing environment on the generation of impurities that might be forming at different processing stages. Careful analysis on the effects of the hygroscopic nature of the precursors on phase, structure and properties have been carried out for BNT [70] and  $0.94\text{Bi}_{0.5}\text{Na}_{0.5}\text{TiO}_3\text{-}0.06\text{BaTiO}_3$  ( $0.94\text{BNT-}0.06\text{BT}$ ) [71]. Li et al. reported that  $\text{Na}_2\text{CO}_3$  experiences an irreversible weight loss of about 1.0 wt% during heating, which could also vary depending on powder batch and storing conditions [70]. BNT samples obtained without pre-drying treatment of  $\text{Na}_2\text{CO}_3$  showed sodium deficiency with a composition estimated as  $\text{Na}_{0.495}\text{Bi}_{0.50}\text{TiO}_{2.9975}$ ; meanwhile, samples obtained using dried  $\text{Na}_2\text{CO}_3$  showed composition closer to stoichiometric  $\text{Na}_{0.50}\text{Bi}_{0.50}\text{TiO}_3$  [70]. In  $0.94\text{BNT-}0.06\text{BT}$ , it was noticed that a pre-drying treatment of all precursors  $\text{Bi}_2\text{O}_3$ ,  $\text{Na}_2\text{CO}_3$  and  $\text{TiO}_2$  at  $400\text{ }^\circ\text{C}$  for 24 h increased the  $R3c/P4bm$  phase fraction ratio, with remarkable effects on the dielectric properties and hysteresis loops [71]. The volatility of bismuth and sodium during high-temperature processing has been reported in several studies, and various strategies have been applied, including the addition of an excess amount of volatile precursors and the coverage of pellets with calcined powder during sintering. Although the exact quantification of Bi and Na volatilization during processing reported in different studies is different, there is a general agreement that Bi is more volatile than Na, and that Bi evaporation during the processing of BNT and derived materials becomes considerable above  $1000\text{ }^\circ\text{C}$ . Thermogravimetric experiments performed by Park and Chung for the preparation of BNT single crystals revealed a weight loss rate of 4.2 wt%/h during dwell at  $1300\text{ }^\circ\text{C}$  [72]. Weight losses of less than 1 wt% were detected during sintering of BNT ceramics at  $1100\text{ }^\circ\text{C}$  [73]. The actual composition of BNT ceramics calcined at  $800\text{ }^\circ\text{C}$  and  $850\text{ }^\circ\text{C}$  for 2 h and sintered at  $1150\text{ }^\circ\text{C}$  for 2 h was estimated as  $\text{Na}_{0.5}\text{Bi}_{0.4983}\text{TiO}_{2.9975}$ , implying that the evaporation of Bi is more severe than Na in the conditions reported [74]. Similar conclusions were reported by Naderer et al. [75], and further supported by Mishra et al [76], who reported a loss of  $1.64 \pm 0.02\%$  and  $0.85 \pm 0.03\%$  for Bi and Na, respectively, in BNT-based ceramics sintered at  $1175\text{ }^\circ\text{C}$  for 3 h.

In BNT-derived compounds, a critical quantity is represented by the Bi/Na molar ratio, which significantly affects important structural characteristics such as lattice parameters, grain size, transition temperatures and various physical properties including electrical conductivity, dielectric permittivity and loss. In particular, it has been reported that Na-deficiency leads to a shift of the (202) and (006) Bragg peaks towards larger d-spacing. Meanwhile, Na-excess and Bi-deficiency decrease the d-spacing [77]. The octahedral tilting angle increases with increasing sodium content, while it hardly changes with Bi non-stoichiometry [77]. The grain size was reported to decrease, either by Na-excess or Na-deficiency [78], as well as by Bi-excess [79]. A-site non-stoichiometry can also result in significant changes in the conduction mechanisms, as reviewed by Yang et al. [80]. For Bi/Na nominal ratios equal or smaller than 1, BNT shows high oxide-ion conductivity, while for Bi/Na greater than 1, electronic conduction becomes predominant. For large Bi-excess, a combination of ionic-electronic conduction mechanisms was found [80]. A departure from Bi/Na nominal ratio also causes an increase in dielectric loss [78,79]. The leakage current is more sensitive to Bi non-stoichiometry, probably due to the higher valence of Bi than Na [81]. The piezoelectric constant  $d_{33}$  increases from Bi-deficient to Bi-rich stoichiometry [79,82] and from Na-excess to Na-deficiency, until 4 mol% deficiency, beyond which the  $d_{33}$  dramatically drops [78]. A systematic increase of  $d_{33}$  from 82 pC/N to 97 pC/N was reported by Spreitzer et al. with increasing Na deficiency until 3 mol% as compared to the stoichiometric composition [56].

Together with A-site non-stoichiometry, the effects of Ti off-stoichiometry should be also considered. It was reported that segregations of  $\text{TiO}_2$  start forming from 1% excess of Ti and increase with increasing Ti content [83]. Deficiency of Ti up to 5% would not produce significant phase modifications. Ceramics with 1% Ti excess exhibited the largest grain size, while the grain size monotonically decreased with increasing Ti deficiency. The coercive field, as well as the maximum and remnant polarization, did not exhibit the usual dependence on the grain size. The smallest remnant polarization was found in samples with 5% Ti deficiency due to the generation of oxygen vacancies, and in samples with 5% Ti excess due to the presence of non-ferroelectric  $\text{TiO}_2$ . In the case of 5% Ti deficiency, the hysteresis loop appeared visibly slanted, with lower remnant polarization and unexpected lower coercive field [83].

### 2.1.3. Stoichiometry assessment and testing

After processing, it is very important to assess the quality of the product obtained to ensure that the processing method is appropriate and reliable. Important tests include the density measurement, the inspection of the microstructure and the analysis of the chemical composition and element distribution, to detect eventual impurities and possible departure from the nominal stoichiometry. It is important to note that in BNT only small stoichiometric imbalances can be accommodated (i.e. 0.17–0.33% for bismuth and

0.25–0.5% for oxygen [84]) without forming secondary phases [70,74,84]. Although the deviations from stoichiometry are often too small to be detected by the commonly-used energy dispersive spectroscopy, stoichiometry imbalance produces remarkable effects on the electrical conductivity and dielectric loss, whose measurements become important techniques to assess not only the electrical characteristics, but also the stoichiometry of BNT [80].

#### 2.1.4. Reproducibility issues and implications for large-scale processing

The hygroscopic and volatile nature of bismuth and sodium precursors, the purity of raw materials and the kinetics of their mutual reactions often result in variations from batch-to-batch powders and scattering in physical properties of the final products, limiting the commercial development of BNT and derived materials. In fact, there are only few commercial products based on bismuth-sodium titanate; these include the PIC700 and PIC701 piezoceramics developed by PI Ceramic GmbH for sonar and hydrophonic applications, and those produced by Honda Electronics Co. Ltd for ultrasonic cleaners [85]. In order to increase the reliable production at industrial scale and widen the applications of BNT-based materials, highly reproducible properties should be attained. Detailed discussions on reproducibility issues, and industrial production of BNT-derived products, can be found in previous reviews [85–87]. These surveys recommend that various processing variables should be considered, including the purity, granulometry and hygroscopicity of the starting materials, the mixing procedure, and calcination and sintering conditions. The latter should avoid undesired reactions and volatilization, whilst obtaining high density and optimum microstructures. Additionally, variations of the processing environment conditions (e.g. humidity, temperature, atmosphere, tools, equipment, etc) should be minimized to enhance reproducibility. It has been reported that improved particles homogeneity and more precise stoichiometry control in BNT and derived materials can be achieved by sol–gel processing [57–63]. This involves lower processing temperatures, and therefore, it allows reducing the evaporation of volatile elements, minimizing stoichiometry imbalance. Besides, a variation of the traditional sol–gel process, named “solution-sol–gel”, can reduce the processing costs, being based on bismuth oxide and sodium carbonate dissolved in nitric acid, and titanium tetraisopropoxide in ethylene glycol, rather than relying on the use of expensive metal alkoxides [57,58]. Additionally, the development of appropriate aqueous routes to avoid the costly use of organic solvents, and the setup of processing environments with constant conditions that would minimize inhomogeneity in large-scale batches, are essential for upscaling production. Examples of aqueous synthesis routes that could be suitable for large-scale processing of BNT thin films have been recently reported in Ref. [63]. Furthermore, for mass production of BNT-based components, the availability and sustainability of the raw materials and the materials for electrodes and firing conditions should be carefully considered [85–87].

## 2.2. Complexity of room-temperature structure of unpoled $\text{Bi}_{0.5}\text{Na}_{0.5}\text{TiO}_3$

Despite the large number of investigations conducted on BNT since its discovery, the average and local structure are still under debate. Structural investigations via neutron and X-ray diffraction are mainly based on Rietveld refinement techniques, which employ pre-existing structural models that cannot satisfactorily account for the peculiar characteristics of the local structure. This is attributed to different factors, such as (i) a small distortion from the parent cubic perovskite structure; (ii) a complicated A-site environment containing aliovalent Bi and Na ions; (iii) different characteristics of Na–O and Bi–O bonds, with the former being ionic and the latter being highly covalent due to the presence of lone pair  $6s^2$  electrons in  $\text{Bi}^{3+}$ ; (iv) a strong diffuse scattering occurring during diffraction experiments.

The presence of a small structural distortion in BNT was already reported in early studies [52,88–90]. In particular, Smolenskii et al. and Buher et al. agreed that the structure exhibits a pseudo-cubic symmetry [52,88,89], while studies from Ivanova et al. supported the presence of a rhombohedral structure [90]. About twenty years later, based on X-ray studies, Zvirgzds et al. proposed that the structure of BNT is the polar  $R3m$  phase, which does not present octahedral tilting ( $a^0a^0a^0$  in the Glazer notation) [91]. Subsequently, Vakhrushev et al. performed neutron diffraction experiments and identified the room-temperature structure of BNT as polar rhombohedral with  $R3c$  space group [92]. More recently, comprehensive neutron diffraction studies on BNT powders carried out by Jones, Kreisel and Thomas confirmed that the room temperature structure is the polar rhombohedral  $R3c$  (lattice parameters  $a_H = 5.488 \text{ \AA}$ ,  $c_H = 13.504 \text{ \AA}$ ,  $V = 352.33 \text{ \AA}^3$ ,  $Z = 6$ , in the hexagonal representation in relation to the pseudo-cubic cell), with the following specific characteristics: (i) a similar A-site occupancy degree of Bi and Na cations, exhibiting underbonding and overbonding, respectively; (ii) cooperative displacements of Bi, Na (larger for Bi than for Na) and Ti cations parallel to the  $[1\ 1\ 1]_{\text{pc}}$  direction in the pseudo-cubic cell, which give rise to a ferroelectric-type polarity; (iii) an antiphase  $\bar{a}\bar{a}\bar{a}$  tilting system (tilting angle  $\omega = 8.24^\circ$ ), identified by opposite rotations of oxygen octahedra about their threefold pseudo-cubic axes, resulting into unit cell doubling as evidenced by the presence of superlattice reflections in the diffraction patterns [93,94].

#### 2.2.1. Rhombohedral vs monoclinic symmetry

Possible inconsistencies with the presence of a pure rhombohedral phase were early identified by Isuyov et al. via the temperature dependence of birefringence and opalescence of BNT, which suggested a structure with lower symmetry than rhombohedral [95]. Other studies have proposed that BNT's structure at room temperature can be identified with the monoclinic  $Cc$  space group [96–100]. Additionally, to better fit the diffraction patterns, biphasic structural models have been used, such as monoclinic  $Cc$ -cubic  $Pm\bar{3}m$  [101], and monoclinic  $Cc$ -rhombohedral  $R3c$  [102,103]. Further support to the monoclinic structure was given by a study from Gorfman et al. on BNT crystals, which showed inhomogeneous optical anisotropy and domain walls with orientations different from those typically observed in rhombohedral phases. [104]. The uncertainty between rhombohedral  $R3c$  and monoclinic  $Cc$  structures can be mainly attributed to the fact that the splitting of the  $(1\ 1\ 0)$  diffraction peak, characteristic of the monoclinic  $Cc$  structure, may disappear due to the presence of various peak-broadening effects [98].

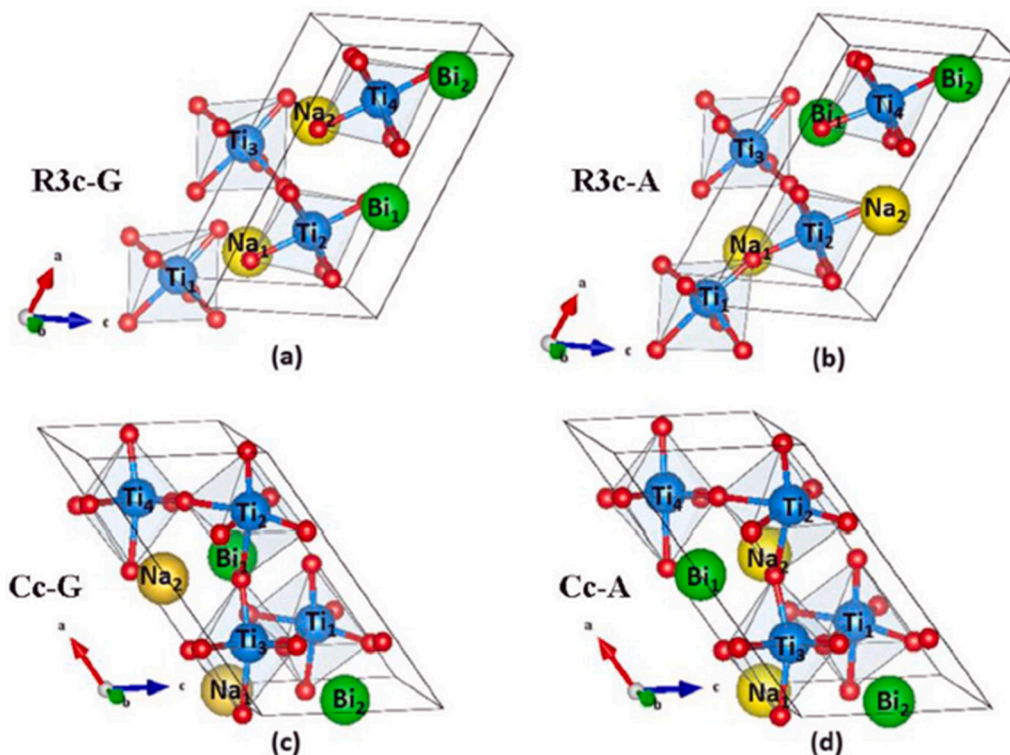


**Fig. 2.** Rhombohedral and monoclinic structures of  $\text{Bi}_{0.5}\text{Na}_{0.5}\text{TiO}_3$ : (a)  $R3c$ -G structure; (b)  $R3c$ -A structure; (c)  $Cc$ -G structure; and (d)  $Cc$ -A structure. [Reproduced from Ref. [105] <https://aip.scitation.org/doi/10.1063/1.4944473> with the permission of AIP Publishing].

Recent ab-initio simulations [105] have investigated the energetics of two structural configurations, indicated as *A*- and *G*-type (see Fig. 2) that possibly exist in both the rhombohedral  $R3c$  and monoclinic  $Cc$  structures. While the lattice parameters of both the relaxed structures did not show significant variations in the *A*- and *G*-type configurations, the  $R3c$  *A*-type showed the lowest energy. The small energy difference with the  $Cc$  *A*-type structure justifies the competition between the rhombohedral and monoclinic phases.

Additional insights on the room temperature structure of BNT have been obtained by infrared and Raman spectroscopy. In the rhombohedral structure, the irreducible representation of the vibrational modes of BNT can be written as  $\Gamma = 4A_1 + 5A_2 + 9E$ , where  $A_1$  and  $E$  are both infrared and Raman active (13 modes in total), while  $A_2$  are silent modes (5 modes in total). The Raman spectrum of BNT displays broad bands, which have been recently deconvoluted in seven modes located at 135, 275, 489, 531, 587, 765 and 840  $\text{cm}^{-1}$  (see Fig. 3) [106]. The number of modes in the deconvolution was lower than that in the irreducible representation, most likely because of the low intensity of some of the modes. Additionally, the deconvolution was purposefully carried out by using the minimum

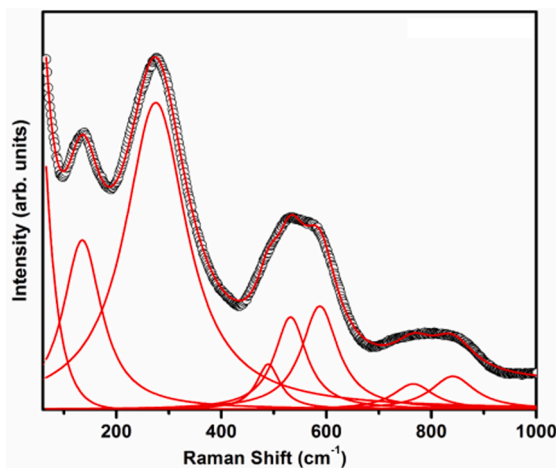


**Fig. 3.** Raman spectrum of  $\text{Bi}_{0.5}\text{Na}_{0.5}\text{TiO}_3$  and deconvolution. [Reproduced from Ref. [106] <https://iopscience.iop.org/article/10.1088/1361-648X/aaf405/meta> with permission from © IOP Publishing].

possible amount of peaks to simplify the interpretation of the fitting parameters [106].

In the low-frequency regime, the Raman mode at  $135\text{ cm}^{-1}$  is related to A—O vibrations [106,107]; the most intense band at around  $275\text{ cm}^{-1}$  is assigned to the Ti—O vibrations, while the modes in the range  $400\text{--}600\text{ cm}^{-1}$  are linked to the vibrations of the  $\text{TiO}_6$  octahedra. Finally, the high-frequency modes between  $650$  and  $950\text{ cm}^{-1}$  are related to vibrations involving oxygen displacement in  $\text{TiO}_6$  octahedra [106].

The vibrational frequencies of BNT have been simulated in the rhombohedral  $R3c$  and monoclinic  $Cc$  structures with both the *A-type* and *G-type* configurations (see Fig. 2) [105]. The different vibrational frequencies identified in the different polymorphs might be used to establish the exact nature of BNT structure. In particular, the *A-type* monoclinic structure  $Cc$  shows a low-frequency phonon mode at about  $40\text{ cm}^{-1}$  that is absent in the other structural configurations [105]. This mode has been identified in the Raman spectra reported by Siny et al. [108]. Despite the broadness of the experimental vibrational spectra and the small differences between the vibrational frequencies in the rhombohedral and monoclinic structures, the presence of the Raman active modes of the two phases in BNT is supportive of the mixed ( $R3c + Cc$ ) structure [105], in agreement with X-ray diffraction studies [101,102].

### 2.2.2. Local structures

The ambiguity on the average structure discussed above is also due to the high complexity of the local structure and has led to a vibrant debate in the literature. In order to closely inspect the local structure, various investigative techniques, such as high energy X-Ray diffraction, X-ray and neutron scattering, transmission electron microscopy (TEM), pair distribution function analysis, Raman spectroscopy and extended X-ray absorption fine structure (EXAFS) spectroscopy have been employed, and different structural models for the room-temperature structure of BNT have been proposed. These have put forward the possible existence of different local structures, including: (i) Guinier-Preston-like zones (GPZs) consisting of either Bi- and/or Na-rich areas, or clusters with monoclinic symmetry, randomly dispersed within the rhombohedral matrix, characterized by a random occupancy of Bi and Na on the A-sites (Fig. 4a–d) [109]; (ii)  $\text{Bi}^{3+}\text{TiO}_3/\text{Na}^+\text{TiO}_3$  clusters with the accumulation of Bi and Na in certain locations (Fig. 4e) [107,110]; (iii) criss-cross structures characterized by the alignment of Bi and Na cations along alternate rows perpendicular to the  $[0\ 0\ 1]$  direction as shown in Fig. 4f [111]; (iv) local monoclinic regions in which Na experiences a displacement along the  $[1\ 1\ 1]_{\text{pc}}$  pseudo-cubic direction and a displacement along one of the six  $[1\ 0\ 0]_{\text{pc}}$  pseudo-cubic directions [96]; (v) tetragonal nanoplatelets with  $a^0a^0c^+$  octahedral tilting, non-homogeneously dispersed within the rhombohedral  $R3c$  matrix (Fig. 4g) [112,113]. In particular, the presence of regions with a high density of tetragonal platelets has further supported the identification of the average structure with the monoclinic  $Cc$  space group, as proposed by Gorfman et al. for BNT single crystals (lattice parameters obtained as  $a = 9.529\text{ \AA}$ ,  $b = 5.480\text{ \AA}$ ,  $c = 5.514$

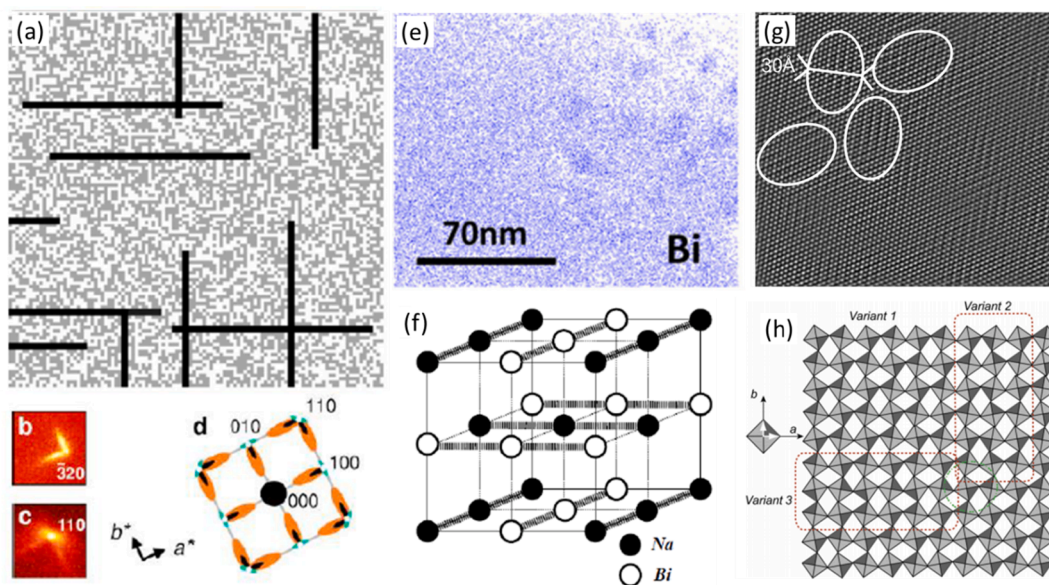


**Fig. 4.** Local structures in BNT: (a) structural model based on Guinier-Preston zones (black bars), immersed in a random distribution of Bi (grey cells) and Na (white cells); (b) asymmetric, L-shaped diffuse scattering around the  $3\bar{2}0$  reflection; (c) superposition of various asymmetric scattering shown in (d), including asymmetric scattering (black part), thermal scattering (green part) and the large underlying scattering (orange part) for the 110 reflection [reproduced with permission from Ref. [109] <https://journals.aps.org/prb/abstract/10.1103/PhysRevB.68.014113> Copyright 2003 by the American Physical Society]; (e) distribution of Bi (blue dots) with evident presence of Bi-rich zones [reproduced with permission from Ref. [110] with permission from Taylor & Francis <https://www.tandfonline.com/doi/abs/10.1080/14786435.2019.1637550?journalCode=tpm20>]; (f) criss-cross structures [reproduced from Ref. [111] <https://www.tandfonline.com/doi/abs/10.1080/00150190211198> with permission from Taylor & Francis]; (g) tetragonal nanoplatelets non-homogeneously dispersed within the rhombohedral matrix [reproduced with permission from Ref. [112] Copyright 2008 by Elsevier]; (h) coexistence of three variants of ( $a^0a^0c^+$ ) in-phase tilting [reproduced with permission from Ref. [114] Copyright 2012 by John Wiley and Sons].

$\text{\AA}$ ,  $\beta = 125.43^\circ$ ) [97]. The identification of the monoclinic structure  $Cc$  in BNT ceramics has been alternatively rationalized by Levin and Reaney [114] based on the coexistence of three variants of in-phase tilting ( $\bar{a}^- \bar{a}^+ c^+$ ), which span within a short range (1–2 nm) along the three axes (Fig. 4h), superimposed on long-range ordered sections with anti-phase tilting, which span for a longer range (>5 nm). The strain arising at the interface between regions with different tilting could be accommodated by a continuous variation of magnitude and direction of octahedral tilting. It was argued that the presence of these microstructural features resulted in the appearance of a monoclinic structure on average [114]. The “continuous tilting” model proposed by Levin and Reaney [114] has been supported by subsequent studies based on nuclear magnetic resonance and ab-initio calculations reported by Groszewicz et al. [115]. Octahedral tilting was found to be the predominant contribution to the electric field gradient extrapolated from the  $^{23}\text{Na}$  NMR spectra, which indicate a continuous tilting mode, rather than the coexistence of separate in-phase and anti-phase tilt systems.

The presence of the monoclinic  $Cc$  was discounted by Ge et al. based on neutron elastic scattering measurements on BNT single crystals [116]. They proposed that the very weak intensity of the  $\{\frac{1}{2}, \frac{1}{2}, \frac{1}{2}\}$  superlattice reflections (allowed in the monoclinic  $Cc$  symmetry, but forbidden in the rhombohedral  $R3c$ ) could be attributed to the existence of a skin region with monoclinic symmetry  $Cc$  on the surface of the crystal [116]. The presence of a monoclinic  $Cc$  space group on average was again reported in a later study by Aksel et al. based on the Rietveld refinement of X-ray and neutron diffraction patterns obtained on calcined powder and sintered pellets [117]. However, atomic pair distribution functions (PDFs), obtained from X-ray and neutron total scattering experiments, allowed identifying local deviations from the average  $Cc$  structure; the calcined powder showed a larger deviation than the sintered pellets. The PDF analysis suggested that A-site ordering does not represent the reason for these local deviations [117]. The application of the so-called “box car fitting” model and the reverse Monte Carlo method indicated that in the average structure, Bi and Na cations locally undergo small shifts from their ideal crystallographic positions, with Bi locally forming asymmetric Bi—O bonds, and Na establishing nearly-symmetric Na—O bonds [117]. Further information about the local Bi environment have been obtained by Keeble et al. via neutron scattering experiments performed on BNT ceramics ground into powder after sintering [118]. The analysis carried out suggested that the local structure emerges from competing monoclinic and orthorhombic symmetries on the A-site, and by the rhombohedral symmetry of the Ti cations in the B-site. It was noticed that Bi and Na cations occupy different lattice locations. In particular, Bi displaces along two possible directions, one lying in the monoclinic plane (indicated as Bi(I)), and the other leaning towards the orthorhombic  $[0\ 1\ 1]_{pc}$  pseudo-cubic direction (labelled Bi(II)), with the former being dominant. Instead, Na cations show displacements only in the monoclinic plane. In this structural configuration, the average structure could be described as rhombohedral [118].

TEM investigations based on selected area diffraction technique reported by Ma et al. support the existence of the monoclinic  $Cc$  structure [100]. On the contrary, Rao et al. reported that the monoclinic phase does not represent an equilibrium state, but the monoclinic distortion is related to the presence of heterogeneities at the nanoscale, including localized in-phase tilting, which lead to an accumulated strain in the global lattice [119]. Additional experiments based on advanced electron diffraction techniques (digital large angle convergent beam electron diffraction) carried out by Beanland and Thomas on BNT single crystals have demonstrated that in defect-free regions, the structure of BNT is rhombohedral  $R3c$  [120]. The refined technique allowed establishing a clear criterion to distinguish  $Cc$  and  $R3c$  phases based on the presence/absence of mirror symmetry and superstructure spots in electron diffraction patterns obtained in twin regions. In particular, considering the electron diffraction patterns taken along the  $[1\ 1\ 0]_{pc}$  direction in two neighbouring regions separated by  $(1\ 1\ 0)_{pc}$  twin planes, the presence of the  $R3c$  was ascertained by the presence of superstructure spots in one of the patterns, together with the presence of a mirror symmetry [120]. Besides, a series of interacting defect structures were observed, including antiphase boundaries, domain walls, and tetragonal platelets; these ultimately lead to the formation of nanotwins and to  $\bar{a}^- \bar{a}^+ c^+$  tilting in their vicinity that can be responsible for the observation of the monoclinic  $Cc$  structure [120].

Additional information on the local structure can be obtained by Raman spectroscopy and EXAFS technique, which can probe the local ionic configurations on a shorter length scale than XRD. Raman spectroscopy allowed identifying the presence of nanosized  $\text{Bi}^{3+}\text{TiO}_3$  and  $\text{Na}^+\text{TiO}_3$  clusters [121], while EXAFS has confirmed the positional disorder of A-site cations in unpoled BNT [122]. This is related to the different characteristics of Bi—O and Na—O bonds that induce local in-phase tilting, which is a characteristic of the monoclinic structure [122].

### 2.2.3. Effect of grain size

Apart from the effects of processing methods, stoichiometry, defects and the intrinsic limitations of the measurements technique, the crystal structure of BNT ceramics has been found to be significantly dependent also on the grain size. Khatua et al. reported that BNT ceramics with grains of about 40  $\mu\text{m}$  exhibit the monoclinic  $Cc$  phase. Meanwhile, in ceramics with grains below  $\approx 2.5\ \mu\text{m}$ , the monoclinic distortion vanishes and the structure becomes nearly cubic [123]. This grain size threshold is much larger than that found in canonical ferroelectric  $\text{BaTiO}_3$  in which a cross-over from the tetragonal to the cubic structure was found at a grain size of approximately 100 nm [124]. The monoclinic distortion in the average structure of BNT was attributed to the presence of heterogeneities at the nanoscale (i.e. nanosized twinned domains) [123]. Based on the absence of clear splitting of  $(1\ 1\ 0)_{pc}$  peak in ceramics with grain size of about 2.3  $\mu\text{m}$ , the skin effect proposed by Ge et al. [116] was discounted by Khatua et al. [123]. However, a skin region of about 20  $\mu\text{m}$  with anisotropic and textured structure was found in  $0.94\text{Bi}_{0.5}\text{Na}_{0.5}\text{TiO}_3\text{-}0.06\text{BaTiO}_3$  by Kong et al. [125] and attributed to two main factors: (i) a biaxial stress state at the ceramic surface; and (ii) oxygen vacancies, which exert an internal chemical pressure producing a lattice expansion. More recently, Luo et al. reported that BNT ceramics with small grain size present the coexistence of monoclinic and rhombohedral phases, while ceramics with larger grains are characterized by the dominance of the rhombohedral phase and the appearance of local structures. These local features include round-shaped nano-regions rich in bismuth, whose size was found to increase under TEM beam irradiation [110].

### 2.3. Temperature-induced structural changes and dielectric behaviour of $\text{Bi}_{0.5}\text{Na}_{0.5}\text{TiO}_3$

Besides the complexity of the room-temperature structure, BNT undergoes a series of structural modifications as a function of temperature, which have yet to be fully clarified. There is a general agreement that above 540 °C, the structure is cubic paraelectric with  $Pm\bar{3}m$  space group, as reported in a previous review [84]. However, depending on the experimental technique used, different structure evolutions upon heating/cooling have been proposed. According to neutron diffraction data obtained on powdered BNT crystals [93], a tetragonal phase with  $P4bm$  space group appears during cooling at 540 °C, and it coexists with the cubic  $Pm\bar{3}m$  phase until 500 °C, where the cubic phase disappears. During further cooling, the coexistence of the tetragonal  $P4bm$  and the rhombohedral  $R3c$  phases was found at least in the range  $\approx 320\text{--}300$  °C, and the stabilization of the rhombohedral phase from approximately 270 °C to  $-250$  °C was identified [93]. A different temperature-induced phase evolution has been proposed based on temperature-dependent X-Ray diffraction during cooling [101]: at 600 °C, the structure is cubic  $Pm\bar{3}m$ ; in the range 400–300 °C, the structure is tetragonal  $P4bm$ , while in the interval 250–25 °C, there is a mixture of monoclinic  $Cc$  and cubic  $Pm\bar{3}m$  phases. Instead, based on electron diffraction experiments, the following structural changes have been identified [126]: (i) below 200 °C, the structure is rhombohedral  $R3c$ ; (ii) in the range 200–280 °C, there is the presence of an antiferroelectric modulated phase made up of  $Pnma$  orthorhombic sheets interspaced between rhombohedral  $R3c$  layers; (iii) in the interval 280–320 °C, the structure is antiferroelectric orthorhombic  $Pnma$ , while it transforms into a paraelectric mixture of  $P4/mbm$  and  $P4_2mm$  tetragonal phases at 320 °C, stable until 520 °C, where the structure becomes cubic paraelectric  $Pm\bar{3}m$  [126]. Based on the studies by Keeble et al., it was realized that two possible types of Bi displacement (Bi(I) and Bi(II)) lead to two possible pathways in the rhombohedral (R) to tetragonal (T) phase transition during heating: Bi(I) is linked to the sequence  $R \rightarrow M_A \rightarrow T$ , while Bi(II) to the path  $R \rightarrow M_B \rightarrow O \rightarrow M_B \rightarrow T$ , with  $M_A$  and  $M_B$  representing different monoclinic segments related to the direction of Bi cation displacement [118].

The temperature-induced transformations are reflected in a peculiar dielectric behaviour. The temperature and frequency dependences of the real and imaginary parts of the dielectric constant are shown in Fig. 5a and b, along with the inverse permittivity (Fig. 5c), neutron scattering and diffuse scattering superimposed on the permittivity (Fig. 5d and e, respectively). It can be seen that on

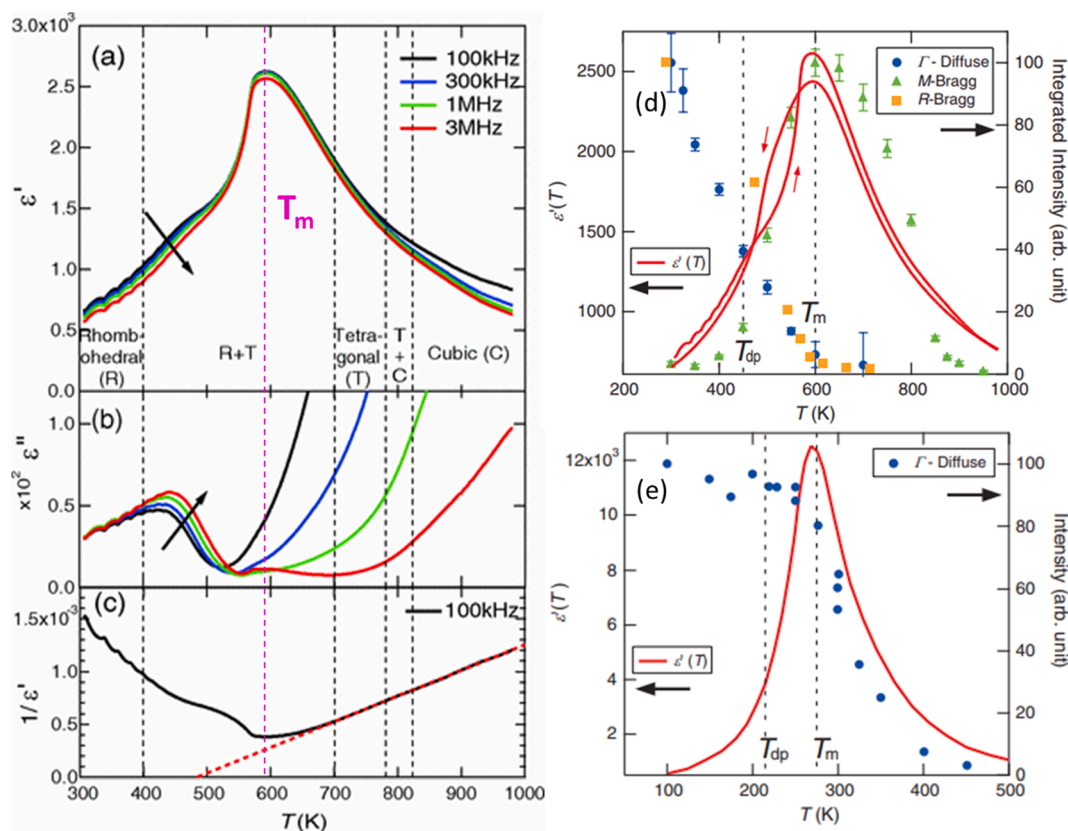


**Fig. 5.** Temperature and dependence of real part (a), imaginary part (b) of dielectric constant and of the inverse of real part of dielectric constant (c) of annealed BNT single crystal along the [100] direction, measured during heating at the frequencies shown in the legends. Temperature dependence of the real part of the dielectric constant at 1 MHz of: (d) BNT plotted along with intensity of diffuse scattering near the  $\Gamma$ -point and of the intensity of superlattice peaks at the M- and R-points; (e) PMN plotted along with intensity of diffuse scattering near the  $\Gamma$ -point. [Reprinted with permission from Ref. [128] <https://journals.aps.org/prb/abstract/10.1103/PhysRevB.87.064109>. Copyright 2013 by the American Physical Society].

cooling from high temperature, the permittivity increases, while there are no visible dielectric anomalies corresponding to the phase transitions at 540 °C and 500 °C (Fig. 5a) identified by Jones and Thomas in their neutron diffraction experiments [93]. Neutron scattering carried out by various researchers has providing further insights into the temperature-induced phase transitions in BNT and the corresponding anomalies in the dielectric permittivity [118,127,128]. The cubic-tetragonal phase transition at 540 °C was found to be related to the condensation of the mode  $M_3$ , which represents the oxygen octahedra tilting around one axis of the cubic lattice [127]. The temperature marked with a line at 700 K (427 °C) corresponds to the emergence of a diffuse scattering peak at the  $\Gamma$ -point of the Brillouin zone [128] and marks the onset of deviation from the Curie-Weiss law (Fig. 5c), attributed to the appearance of the rhombohedral phase [128], in agreement with earlier investigations [129]. However, in other studies, the onset of the rhombohedral phase is identified at about 593 K (320 °C), just below the dielectric maximum at  $T_m \approx 600$  K (327 °C) [130–132], where the intensity of the diffuse scattering showed a small increase [128]. This behaviour is different from that observed in lead-based relaxors (such as PMN), where the intensity of the diffuse scattering continuously grows as the permittivity increases approaching  $T_m$  [128]. Another remarkable difference between BNT and conventional lead-based relaxors is that the frequency dispersion of the dielectric peak at  $T_m$  is negligible in the kHz-MHz range (Fig. 5a), while it becomes evident in the GHz-THz range [132]. In Fig. 5d, it can be also observed that the temperature dependence of the superlattice reflections at the M-point is similar to that of the permittivity, displaying a maximum intensity at  $T_m$ . Additionally,  $T_m$  marks the onset of superlattice reflections at the R-point; however, in a previous study, these were observed from approximately 1020 K (747 °C) [133], indicating the competition between tetragonal and rhombohedral phases in a broad temperature range. Similar to lead-based relaxors,  $T_m$  does not appear to be a distinctive transition point in BNT; however, based on the described observations, it was concluded that the broad dielectric peak is related to a diffusive first-order transition between the tetragonal and rhombohedral phases [128]. This is also supported by the thermal hysteresis observed in the temperature dependence of the permittivity between heating and cooling cycles (see Fig. 5d), as also reported in other studies [134]. An incommensurate modulation near the  $\Gamma$ -point was detected at about 600 K [131], almost concomitantly with the instability related to the appearance of the rhombohedral phase at about 593 K (320 °C) mentioned above. By further lowering the temperature below 550 K (277 °C), the dielectric dispersion increases, the tetragonal phase increasingly disappears, but the incommensurate modulation is still present below 127 °C, and it coexists with the rhombohedral phase until low temperatures [132].

#### 2.4. Electric field-induced transformations in $Bi_{0.5}Na_{0.5}TiO_3$

BNT undergoes intriguing structural transformations when subjected to an external electric field. Rao and Ranjan have reported an irreversible electric field-induced transition from the monoclinic  $Cc$  to rhombohedral  $R3c$  structure, after a DC poling field of 70 kV/cm was applied at room temperature for 10 min on BNT ceramics prepared by solid-state reaction and conventional sintering [99]. The claim was based on the Rietveld refinement of X-ray diffraction patterns, obtained with a laboratory diffractometer on unpoled and poled crushed ceramics. The transition was considered irreversible on the basis of two main observations: (i) the diffraction pattern of a poled sample remained completely unaltered after one month; (ii) the application of an electric field opposite to the poling field did not re-establish the initial monoclinic phase. The latter reappeared at room temperature only after heating the sample at high temperature in the cubic phase range [99]. The  $Cc$ -to- $R3c$  field-induced transition was rationalized according to two possible mechanisms, one based on the rotation of the polarization vector and the other based on an adaptive model of the  $Cc$  monoclinic phase. Regarding the first mechanism, it was argued that in the monoclinic  $Cc$  structure, the polarization vector was contained in the  $(1 \bar{1} 0)_{pc}$  plane and, under the action of the applied electric field, it could rotate towards the  $[1 1 1]_{pc}$  direction by still lying on the  $(1 \bar{1} 0)_{pc}$  plane, leading to the observation of the rhombohedral phase [99]. The second proposed mechanism was derived from the theory of adaptive phases. These are characterized by miniaturized twinned domain structures with small domain wall energies and by lattice parameters that could be obtained from the structures present in differently-oriented domain variants [135]. In this scenario, the monoclinic distortion observed in the diffraction patterns of BNT could be associated to the presence of interacting twinned rhombohedral nanodomains, with smaller size than the X-rays coherence length (adaptive theory). Relying on the consistency between the lattice parameters of the  $Cc$  structure obtained from the Rietveld refinement and those derived from the relationships of the adaptive theory, the  $Cc$ -to- $R3c$  phase transition was attributed to the merging and growth of the rhombohedral twinned nanodomains into polar domains with larger size than the X-rays coherence length [99]. Rao et al. have shown that the P-E loops of BNT ceramics do not present any characteristic signs of electric field-induced transformations, as noticeable in Fig. 6a–d [119]. However, by generating P-E loops at different electric field amplitudes, it was observed that the first saturated loop on initially virgin samples was only obtained when the electric field amplitude was 64 kV/cm (black curve in Fig. 6d). Meanwhile, saturated P-E loops could be obtained at a lower amplitude on samples in which saturation had been previously induced (red curve in Fig. 6c) [119]. Additionally, based on TEM investigations, Rao and co-workers found that the characteristic in-phase octahedral tilting of the  $Cc$  phase and the consequent strain heterogeneity observed in the initial unpoled state are significantly suppressed after poling [119]. The suppression of nanoscale heterogeneities with the applied field was also supported by the smaller frequency dispersion of the permittivity observed in poled samples (Fig. 6e) [103,119,136]. In a separate study coordinated by Ranjan, it was shown that in samples with  $R3c + Cc$  phase coexistence, the monoclinic phase gradually disappears, while the piezoelectric coefficient  $d_{33}$  increases with increasing poling field (Fig. 6f) [102].

The extent of the monoclinic-to-rhombohedral transformation in BNT ceramics sintered by spark plasma sintering was found to decrease with decreasing grain size, being significantly reduced in grains below 2  $\mu$ m in size [123]. By comparing poled bulk ceramics and poled pressed powder, it was concluded that the hindrance to the field-induced transformation in bulk ceramics originates from clamping effects existing between neighbouring grains with different orientations. It was proposed that differently from conventional ferroelectrics, where the electric field mainly acts on ferroelectric domains and their walls, in BNT ceramics, the electric field produces

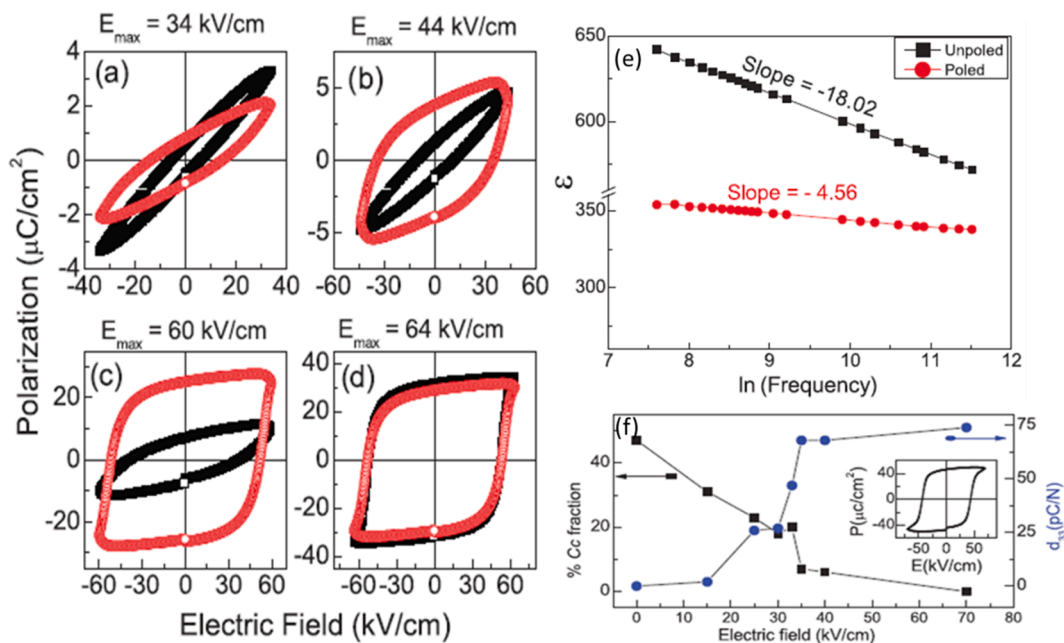


**Fig. 6.** (a)–(d) P-E loops obtained at different electric field amplitudes. Black curves represent the loops obtained on initially unpoled ceramics with increasing the maximum applied field. Red curves represent the loops obtained by decreasing the maximum field applied on the ceramic undergone the electrical history represented by the black curves sequence [Reprinted with permission from Ref. [119] <https://journals.aps.org/prb/abstract/10.1103/PhysRevB.88.224103> Copyright 2013 by the American Physical Society]. (e) Dielectric permittivity as a function of frequency in unpoled and poled samples at room temperature [Reprinted with permission from Ref. [119] <https://journals.aps.org/prb/abstract/10.1103/PhysRevB.88.224103> Copyright 2013 by the American Physical Society]; (f) fraction of the monoclinic Cc phase and piezoelectric coefficient  $d_{33}$  at different poling fields [Reprinted with permission from Ref. [102] <https://journals.aps.org/prb/abstract/10.1103/PhysRevB.87.060102> Copyright 2013 by the American Physical Society].

transformations on the nanoscale heterogeneities, by suppressing the in-phase tilting in favour of the anti-phase tilting, and by driving the growth/merging of twinned nanodomains [123].

Structural differences between unpoled and poled samples have also been identified from their respective room temperature Raman spectra [106,119,137]. It was observed that unpoled samples show broader and more asymmetric A–O and Ti–O bands, due to the additional modes related to the presence of structural heterogeneities before poling. Additionally, a softening of both A–O and

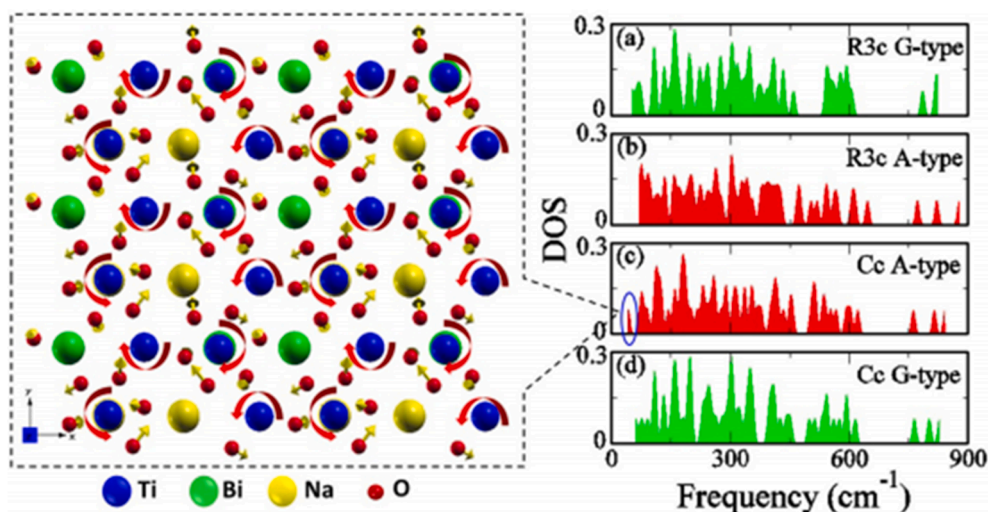


**Fig. 7.** Vibrational density of states in different structures: (a) R3c-G, (b) R3c-A, (c) Cc-A, and (d) Cc-G. The left inset shows a schematic representation of the softest phonon mode identified in the Cc-A structure. [Reproduced from Ref. [105] <https://aip.scitation.org/doi/10.1063/1.4944473> with the permission of AIP Publishing].

Ti—O bands was noticed in the Raman spectra of poled samples [106,137].

Ab-initio studies on A-site cations ordering have provided additional insights into the mechanisms of the *Cc*-to-*R3c* field-driven transition [105]. It was pointed out that the two structures mainly differ in the octahedral tilting system: the *Cc* structure has an  $\bar{a}\bar{a}c$  tilting, while the *R3c* possess an  $\bar{a}\bar{a}\bar{a}$  tilting system. Therefore, the *Cc*-to-*R3c* transition shall involve rotations of the oxygen octahedra around the *c*-axis in the *Cc* structure leading to the  $\bar{a}\bar{a}\bar{a}$  tilting configuration. From the analysis of the simulated vibrational spectra, it was noticed that the lowest frequency phonon mode at about  $40\text{ cm}^{-1}$  in the *Cc* structure with *A-type* configuration involves oxygen displacements that induce the rotation of octahedra around the *c*-axis (Fig. 7), as well as Bi displacements that induce an electrical dipole; due to the latter mechanism, this specific phonon mode can be regarded as a polar mode that actively reacts to the external field, representing a favourable pathway for the *Cc*-to-*R3c* electric field-induced transition [105].

*In-situ* X-ray total scattering experiments during the application of an electric field allowed probing electric field-driven transformations at the sub-Angstrom/nanometre scale through the analysis of the atomic pair distribution functions (PDFs) obtained along different orientations with respect to the applied field direction. The results confirmed the occurrence of a monoclinic-to-rhombohedral field-induced transformation at electric fields greater than  $35\text{ kV/cm}$  [138]. It was observed that the application of the external field produces more isotropic atomic displacement parameters, more isotropic peaks broadening and reduces diffuse scattering [138]. The effect of an applied field on the PDFs and domain process is schemed in Fig. 8. The functions  $G(r)$  plotted in Fig. 8a–d provide the distributions of interatomic distances for Bi—Ti along the  $[1\ 1\ 1]_{pc}$  pseudo-cubic direction (peak approximately in the range  $3.1\text{--}3.4\text{ \AA}$ ), and for Bi—Bi/Ti—Ti along the  $[0\ 0\ 1]_{pc}$  pseudo-cubic direction (peak at about  $3.9\text{ \AA}$ ) and along the pseudo-cubic unit cell face diagonal (peak at about  $5.5\text{ \AA}$ ). These have been determined in absence of an applied field and for grains in which the above-mentioned directions are oriented at  $0^\circ$ ,  $30^\circ$ ,  $45^\circ$ ,  $60^\circ$ ,  $90^\circ$  with respect to the direction of the applied electric field of  $4\text{ kV/mm}$ . The interatomic distances Bi—Ti increase in direction perpendicular to the applied field and decrease in direction parallel to the applied field (Fig. 8a). Meanwhile, Bi—Bi and Ti—Ti distances remain nearly unaltered, showing a negligible directionality (Fig. 8a). The atomic pair distribution functions of the Bi—Ti distances were fitted by considering one short (R1), six intermediate (3 + 3) (R2), and one long (R3) distances in the rhombohedral structure (see Fig. 8f). For an accurate fitting of the Bi—Ti PDFs in the unpoled state, all short, intermediate and long distances had to be used (Fig. 8b). In the poled sample, PDFs in direction parallel to the field could be fitted with the short R1 and long R3 distances (Fig. 8c), while in direction perpendicular to the field only the intermediate distance R2 was used (Fig. 8d). The relationship between interatomic distances and domain process under the influence of an applied field is schemed in Fig. 8e and f [138].

EXAFS studies have shown that the electric field has a significant influence on the bonding environment of Bi, but a lower effect on

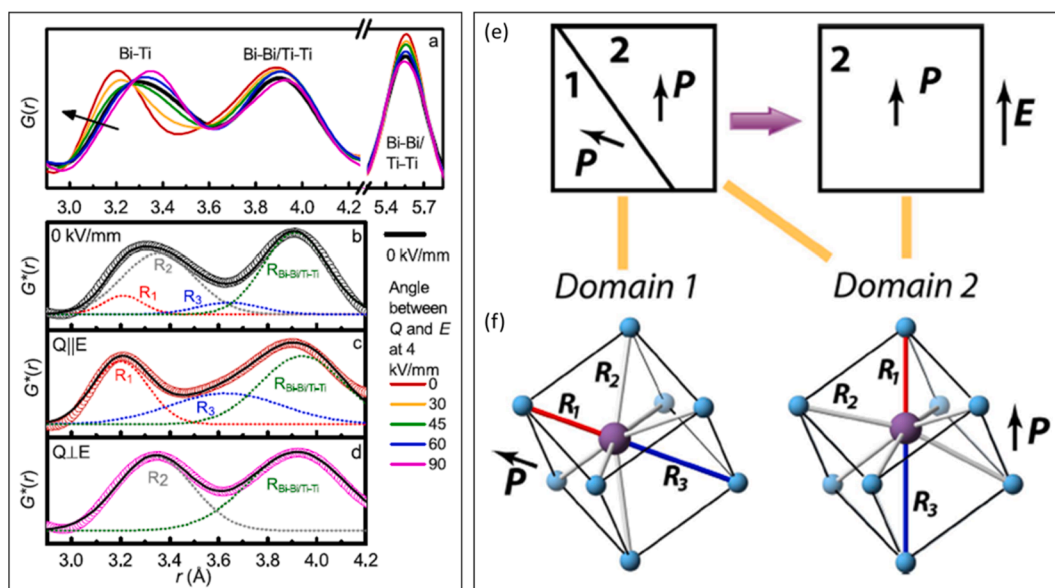


**Fig. 8.** (a) Distribution function  $G(r)$  of interatomic distances for Bi—Ti along the  $[1\ 1\ 1]_{pc}$  pseudo-cubic direction and for Bi—Bi/Ti—Ti along the  $[0\ 0\ 1]_{pc}$  pseudo-cubic direction. The black curve indicates the distribution obtained in absence of an applied field ( $E = 0\text{ kV/mm}$ ); the other curves with different colours indicate the distributions obtained during the application of an electric field of  $4\text{ kV/mm}$ , for different directions of the scattering vector  $Q$ . Following the direction of the black arrow,  $Q$  changes orientation from a direction perpendicular to a direction parallel to the applied field; (b)–(d) fitting of the distribution of interatomic distances in absence of an applied field (b) and under an applied field of  $4\text{ kV/mm}$  in case  $Q \parallel E$  (c) and  $Q \perp E$  (d), using three Bi—Ti distances (R1, R2 and R3) and a single Bi—Bi/Ti—Ti distance all shown in dashed lines; (e) scheme of domain structure evolution from two-domains to one-domain configuration under the applied field  $E$ ; (f) interatomic Bi (purple)-Ti (blue) distances in the BNT rhombohedral structure when Bi atoms displace along the polar axis in the unpoled and poled state. The scheme identifies the three Bi—Ti distances, namely R1 (short), R2 (intermediate) and R3 (long). [Reproduced with permission from Ref. [138]].

G. Viola et al.

the Ti coordination, as it tends to align A-site cations along the polar direction of the R3c structure [122]. Subsequent studies based on PDFs obtained using neutron scattering [139] reported analogous conclusions, ascertaining that BNT undergoes irreversible structural changes at the nanometer scale (few nm) during electrical loading.

Distinctive anomalies in the hysteresis loops at room temperature related to the electric field-induced structural transformations in BNT have been reported in a recent study by Zhou et al. on BNT ceramics [103]. A sharp increase in polarization, strain and electric current was observed under an electric field of approximately 70 kV/cm during the very first poling cycle (Fig. 9a–c). These drastic changes were no longer visible in the subsequent cycle, in which normal ferroelectric behaviour was observed (Fig. 9a–c), with a coercive field of about 60 kV/cm and a remnant polarization of approximately  $40 \mu\text{C}/\text{cm}^2$  (Fig. 9a). It was confirmed that the electric field produced a structural transition from monoclinic Cc to rhombohedral R3c, with the suppression of local microstructural heterogeneities and the transformation of the nanodomains present in the virgin state into wedge-shaped domains in the poled state, as observed by transmission electron microscopy (see Fig. 9d, e). The proximity of the critical electric field inducing the transition and the coercive field suggested that the phase transition was concomitant with domain switching/poling, justifying the strong anomalies observed in the first electrical cycle [103]. These observations confirm that BNT can be regarded as a non-ergodic relaxor that irreversibly transforms to a ferroelectric state under the application of an electric field, via irreversible structural and microstructural transformations.

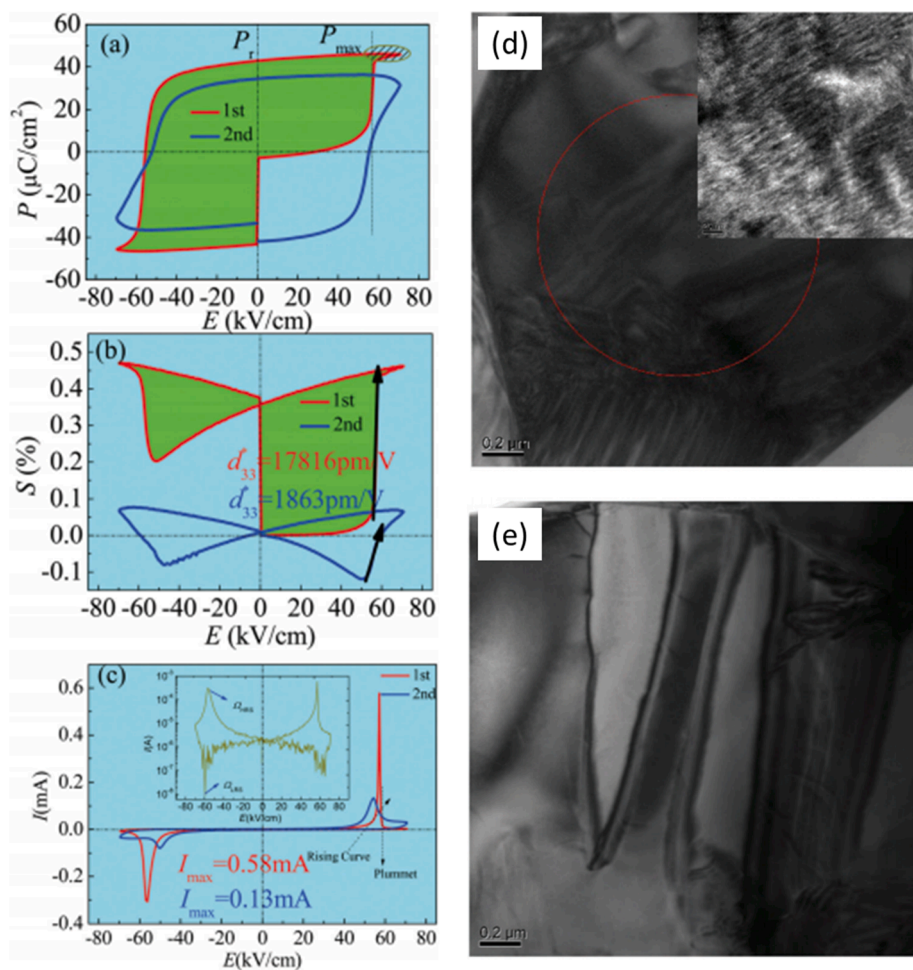


**Fig. 9.** Hysteresis loops obtained during two successive electric field cycles: (a) polarization–electric field; (b) strain–electric field; (c) current–electric field; domain structure in unpoled (d) and poled (e) state. [Reproduced with permission from Ref. [103] Copyright 2019 Royal Society of Chemistry].

### 3. Generalities on Bi<sub>0.5</sub>Na<sub>0.5</sub>TiO<sub>3</sub>-based solid solutions and electric field-induced transformations

#### 3.1. Phase diagrams of relevant systems

Electroceramics based on bismuth-sodium titanate have attracted large research interest over the last decade, in the search of potential candidates to replace lead-based compounds in a wide range of applications. In order to improve various functional properties, a vast amount of chemical modifications of the parent compound BNT have been conducted by substitution and doping, leading to significant variations of structures and properties. The most important progress on understanding the effects of composition and processing on crystal structure, and piezoelectric, ferroelectric and relaxor properties have been summarized in various reviews [54,140–144]. In this section, several examples of BNT-based solid solutions are introduced with the main purpose of illustrating the

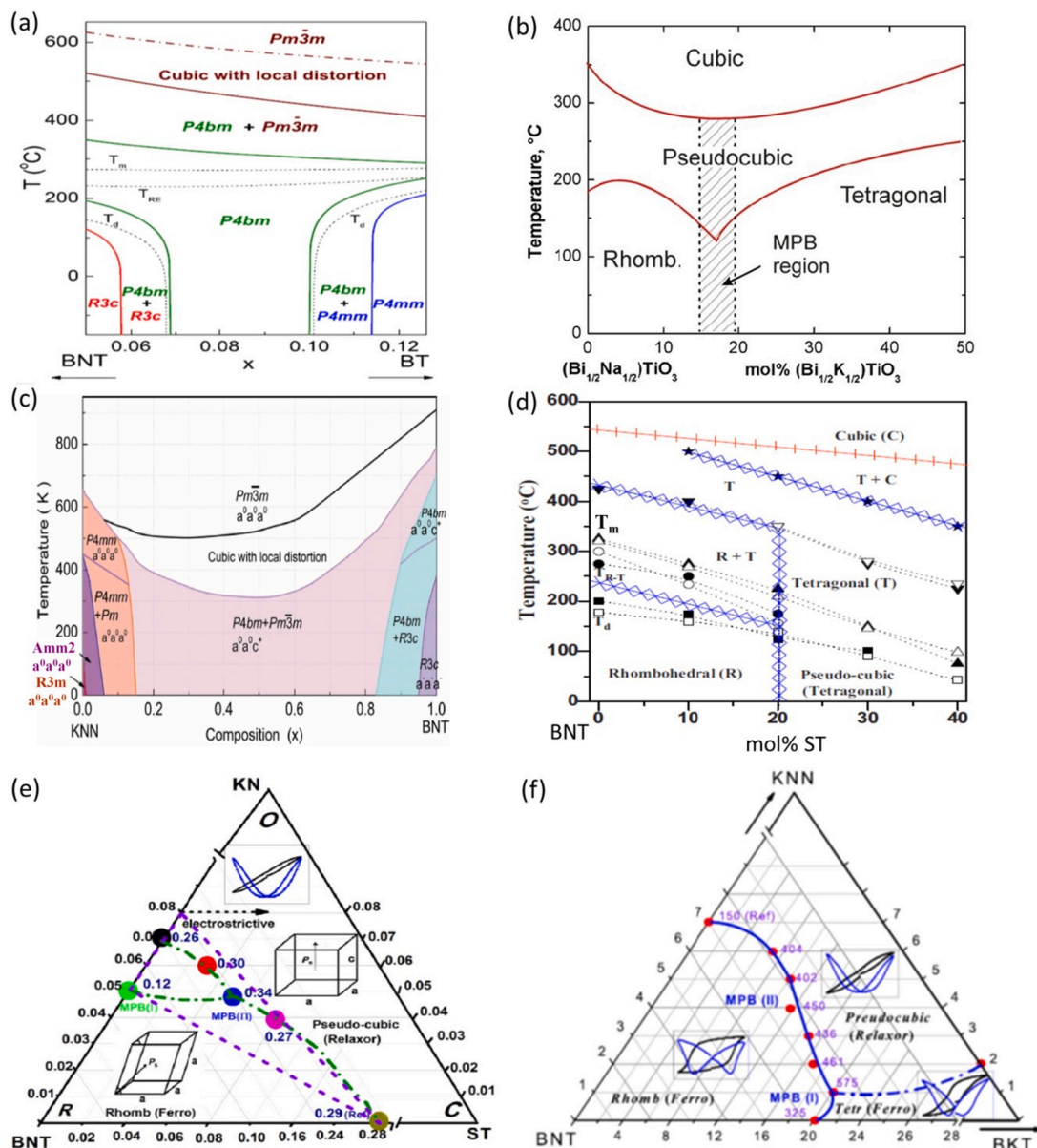


Fig. 10. Phase diagrams of different BNT-based materials: (a) BNT-BT [Reproduced with permission from Ref. [145] Copyright 2011 John Wiley and Sons]; (b) BNT-BKT [Reproduced with permission from Ref. [146] <https://iopscience.iop.org/article/10.1088/1468-6996/11/4/044302/meta> with permission from Taylor & Francis]; (c) BNT-KNN [Reproduced with permission from Ref. [147]]; (d) BNT-ST [Reproduced from Ref. [148] <https://aip.scitation.org/doi/10.1063/1.3490781> with the permission of AIP Publishing]; (e) BNT-ST-KN [Reproduced with permission from Ref. [150], Copyright 2015 Elsevier]; (f) BNT-BKT-KNN [Reproduced from Ref. [151] <https://aip.scitation.org/doi/10.1063/1.4795511> with the permission of AIP Publishing].

**Table 1**  
Summary of BNT-based compounds undergoing electric field-induced transformations.

Composition details	Initial Structure	E-induced structure	Critical electric field [kV/cm]	Type of transition	Reference
0.945(Bi <sub>0.5</sub> Na <sub>0.5</sub> )TiO <sub>3</sub> -0.055Ba(Al <sub>0.5</sub> Nb <sub>0.5</sub> )O <sub>3</sub>	<i>Pseudo-cubic</i>	<i>Rhombohedral</i>	57	Reversible.	[152]
0.96Bi <sub>0.5</sub> Na <sub>0.5</sub> TiO <sub>3</sub> -0.04BaTiO <sub>3</sub> (Single crystal)	<i>R3c</i>	<i>R3c</i>	46	Irreversible suppression of stacking faults with tetragonal symmetry and growth of rhombohedral domains.	[153]
0.948Bi <sub>0.5</sub> Na <sub>0.5</sub> TiO <sub>3</sub> -0.052BaTiO <sub>3</sub> (Single crystal)	<i>Pseudo-cubic-Rhombohedral with traces of tetragonal</i>	<i>Tetragonal</i>	20 along (001) pseudo-cubic direction		[154]
0.94Bi <sub>0.5</sub> Na <sub>0.5</sub> TiO <sub>3</sub> -0.06BaTiO <sub>3</sub>	<i>R3c + P4bm</i>		46	Irreversible suppression of a <sup>0</sup> a <sup>0</sup> c <sup>+</sup> octahedral tilting in favour of <i>a'a'</i> .	[155]
0.93Bi <sub>0.5</sub> Na <sub>0.5</sub> TiO <sub>3</sub> -0.07BaTiO <sub>3</sub>	<i>Pseudo-cubic</i>	<i>Tetragonal</i>	30	Irreversible.	[156,157]
0.925Bi <sub>0.5</sub> Na <sub>0.5</sub> TiO <sub>3</sub> -0.075BaTiO <sub>3</sub>	<i>R3c with traces of P4bm</i>	<i>Tetragonal</i>	>20	Irreversible.	[158]
0.93Bi <sub>0.5</sub> Na <sub>0.5</sub> TiO <sub>3</sub> -0.07BaTiO <sub>3</sub> -xPr (x = 0, 0.001, 0.003, 0.005, 0.007, 0.008, 0.010)	<i>Pseudo-cubic</i>	<i>Rhombohedral + tetragonal</i>	40 (DC poling)	Irreversible. Reversible for x ≥ 0.008.	[159]
0.95[(Bi <sub>0.5</sub> Na <sub>0.5</sub> ) <sub>0.99</sub> (Li <sub>0.5</sub> Nd <sub>0.5</sub> ) <sub>0.01</sub> TiO <sub>3</sub> ]-0.05BaTiO <sub>3</sub>	<i>Pseudo-cubic</i>	<i>Rhombohedral</i>	20	Irreversible ordering and coalescence of nanodomains into ferroelectric domains.	[160]
0.95[(Bi <sub>0.5</sub> Na <sub>0.5</sub> ) <sub>0.9</sub> (Li <sub>0.5</sub> Nd <sub>0.5</sub> ) <sub>0.1</sub> TiO <sub>3</sub> ]-0.05BaTiO <sub>3</sub>	<i>Pseudo-cubic</i>	<i>No change due to weak correlation of nanodomains</i>		Irreversible ordering and coalescence of nanodomains into ferroelectric domains.	[161]
0.93[(Bi <sub>0.5</sub> Na <sub>0.5</sub> ) <sub>1-x</sub> (Li <sub>0.5</sub> Sm <sub>0.5</sub> ) <sub>x</sub> TiO <sub>3</sub> ]-0.07BaTiO <sub>3</sub> (x = 0, 0.01, 0.02, 0.03, 0.04, 0.05)	<i>Pseudo-cubic</i>	<i>Tetragonal</i>	60 (DC poling)		[162]
[(Bi <sub>0.5</sub> Na <sub>0.5</sub> ) <sub>0.95</sub> Ba <sub>0.05</sub> ] <sub>1-x</sub> La <sub>x</sub> TiO <sub>3</sub> (x = 0.01, 0.02, 0.025)	<i>Pseudo-cubic (R3c + P4bm)</i>	Mainly <i>R3c</i>		Irreversible alignment of polar nanodomains.	[163]
[(Bi <sub>0.5</sub> Na <sub>0.5</sub> ) <sub>0.95</sub> Ba <sub>0.05</sub> ] <sub>1-x</sub> La <sub>x</sub> TiO <sub>3</sub> (x = 0.03, 0.04, 0.05, 0.06)	<i>Pseudo-cubic</i>			Reversible due to presence of thermally fluctuating PNRs.	[163]
0.99[(Bi <sub>0.5</sub> Na <sub>0.5</sub> ) <sub>0.935</sub> Ba <sub>0.065</sub> TiO <sub>3</sub> ]-0.01SrZrO <sub>3</sub>	<i>Tetragonal</i>	<i>Rhombohedral + tetragonal</i>	30-60 (DC poling)	Irreversible.	[164]
(1-x)[(Bi <sub>0.5</sub> Na <sub>0.5</sub> )TiO <sub>3</sub> -0.06BaTiO <sub>3</sub> ]-xBi(Ni <sub>0.5</sub> Ti <sub>0.5</sub> )O <sub>3</sub> (x > 0.035)	<i>Pseudo-cubic</i>	<i>Rhombohedral</i>		Reversible.	[165]
(Bi <sub>0.5</sub> Na <sub>0.5</sub> ) <sub>0.93</sub> Ba <sub>0.07</sub> Ti <sub>1-x</sub> (Al <sub>0.5</sub> Nb <sub>0.5</sub> ) <sub>x</sub> O <sub>3</sub> (x = 0.005-0.015)	<i>Pseudo-cubic</i>	<i>Rhombohedral+tetragonal</i>	40 (DC poling)	Irreversible.	[166]
(Bi <sub>0.5</sub> Na <sub>0.5</sub> ) <sub>1-x</sub> Ba <sub>x</sub> Ti <sub>0.98</sub> (Fe <sub>0.5</sub> Ta <sub>0.5</sub> ) <sub>0.02</sub> O <sub>3</sub> (x = 0.045-0.055)	<i>Pseudo-cubic</i>	<i>Tetragonal</i>		Irreversible.	[167]
(Bi <sub>0.5</sub> Na <sub>0.5</sub> ) <sub>1-x</sub> Ba <sub>x</sub> Ti <sub>0.98</sub> (Fe <sub>0.5</sub> Sb <sub>0.5</sub> ) <sub>0.02</sub> O <sub>3</sub> (x = 0.045-0.055)	<i>Pseudo-cubic</i>	<i>Tetragonal</i>		Irreversible.	[168]
0.92(Bi <sub>0.5</sub> Na <sub>0.5</sub> )TiO <sub>3</sub> -0.06BaTiO <sub>3</sub> -0.02BiAlO <sub>3</sub>	<i>Pseudo-cubic</i>	<i>Rhombohedral</i>	60 (DC poling)	Irreversible.	[169]
0.92Bi <sub>0.5</sub> Na <sub>0.5</sub> TiO <sub>3</sub> -0.06BaTiO <sub>3</sub> -0.02K <sub>0.5</sub> Na <sub>0.5</sub> NbO <sub>3</sub> (Single crystals)	<i>Pseudo-cubic</i>	<i>Pseudo-cubic + tetragonal</i>	≥14	Reversible. Formation of domain texture during the transition.	[170]
0.92Bi <sub>0.5</sub> Na <sub>0.5</sub> TiO <sub>3</sub> -0.06BaTiO <sub>3</sub> -0.02K <sub>0.5</sub> Na <sub>0.5</sub> NbO <sub>3</sub>	<i>P4bm</i>	<i>P4bm + R3c</i>	60	Reversible.	[171]
0.91Bi <sub>0.5</sub> Na <sub>0.5</sub> TiO <sub>3</sub> -0.06BaTiO <sub>3</sub> -0.03K <sub>0.5</sub> Na <sub>0.5</sub> NbO <sub>3</sub>	<i>P4bm + R3c</i>		50	Reversible formation of domains.	[172,173]
0.88Bi <sub>0.5</sub> Na <sub>0.5</sub> TiO <sub>3</sub> -0.12Bi <sub>0.5</sub> K <sub>0.5</sub> TiO <sub>3</sub>	<i>R3c</i>	<i>R3c</i>			[151]
0.8Bi <sub>0.5</sub> Na <sub>0.5</sub> TiO <sub>3</sub> -0.2Bi <sub>0.5</sub> K <sub>0.5</sub> TiO <sub>3</sub>	<i>R3c</i>	<i>R3c + Tetragonal (P4mm or P4bm)</i>	20	Irreversible.	[174,175]
0.7Bi <sub>0.5</sub> Na <sub>0.5</sub> TiO <sub>3</sub> -0.3Bi <sub>0.5</sub> K <sub>0.5</sub> TiO <sub>3</sub>	<i>P4mm</i>	<i>P4mm</i>			[174,175]
Bi <sub>0.5</sub> (Na <sub>0.82</sub> K <sub>0.18</sub> ) <sub>0.5</sub> [1-x]La <sub>x</sub> TiO <sub>3</sub> (0 < x ≤ 0.03)	<i>Rhombohedral + tetragonal</i>		50 (DC poling)		[176]

(continued on next page)

Table 1 (continued)

Composition details	Initial Structure	E-induced structure	Critical electric field [kV/cm]	Type of transition	Reference
$[\text{Bi}_{0.5}(\text{Na}_{0.82}\text{K}_{0.18})_{0.5}]_{0.98}\text{Li}_{0.02}\text{TiO}_3$	<i>Pseudo-cubic</i>	<i>Rhombohedral</i>	50 (DC poling)		[177]
$\text{Bi}_{0.48}(\text{Na}_{0.85}\text{K}_{0.15})_{0.48}\text{Sr}_{0.04}[\text{Ti}_{0.977}\text{Nb}_{0.023}]_2\text{O}_3$	<i>Pseudo-cubic</i>	<i>Tetragonal</i>	30	Reversible.	[178]
$0.98(\text{Bi}_{0.5}\text{Na}_{0.5}\text{TiO}_3\text{-Bi}_{0.5}\text{K}_{0.5}\text{TiO}_3)\text{-}0.02\text{Ba}(\text{Zr}_{0.05}\text{Ti}_{0.95})_2\text{O}_3$	<i>Pseudo-cubic</i>	<i>Rhombohedral</i>	40		[179]
$0.99[\text{Bi}_{0.5}(\text{Na}_{0.4}\text{K}_{0.1})(\text{Ti}_{1-x}\text{Nb}_x)]_2\text{O}_3\text{-}0.01(\text{Ba}_{0.7}\text{Sr}_{0.3})_2\text{TiO}_3$ ( $x = 0\text{-}0.02$ )	<i>Pseudo-cubic</i>	<i>Rhombohedral</i> + <i>tetragonal</i>	60 (DC poling)		[179]
$0.99[\text{Bi}_{0.5}(\text{Na}_{0.4}\text{K}_{0.1})(\text{Ti}_{1-x}\text{Nb}_x)]_2\text{O}_3\text{-}0.01(\text{Ba}_{0.7}\text{Sr}_{0.3})_2\text{TiO}_3$ ( $x = 0\text{-}0.02$ )	<i>Pseudo-cubic</i>	<i>Rhombohedral</i> – <i>tetragonal</i>	40	Reversible.	[180]
$0.99[(\text{Bi}_{0.5}\text{Na}_{0.4}\text{K}_{0.1})_{0.98}\text{La}_{0.02}\text{TiO}_3]\text{-}0.01[\text{Ba}_{0.7}\text{Sr}_{0.3}\text{TiO}_3]$	<i>Pseudo-cubic</i>	<i>Rhombohedral</i> – <i>tetragonal</i>			[181]
$(1-x)(0.81\text{Bi}_{0.5}\text{Na}_{0.5}\text{TiO}_3\text{-}0.19\text{Bi}_{0.5}\text{K}_{0.5}\text{TiO}_3)\text{-}x\text{BiZn}_{0.5}\text{Ti}_{0.5}\text{O}_3$ ( $x = 0.02, 0.04, 0.06$ )	<i>Pseudo-cubic</i>	<i>Rhombohedral</i> -like		Irreversible.	[182]
$0.98(0.8\text{Bi}_{0.5}\text{Na}_{0.5}\text{TiO}_3\text{-}0.2\text{Bi}_{0.5}\text{K}_{0.5}\text{TiO}_3)\text{-}0.02\text{BiZn}_{0.5}\text{Ti}_{0.5}\text{O}_3$	<i>Pseudo-cubic</i>	<i>Rhombohedral</i> + <i>tetragonal</i>	40 (DC poling)	Irreversible.	[183]
$0.99[0.8\text{Bi}_{0.5}\text{Na}_{0.5}\text{TiO}_3\text{-}0.2\text{Bi}_{0.5}\text{K}_{0.5}\text{TiO}_3]\text{-}0.01\text{K}_{0.5}\text{Na}_{0.5}\text{NbO}_3$	<i>Rhombohedral</i> + <i>pseudo-cubic</i>	<i>Rhombohedral</i> + <i>distorted pseudo-cubic</i>	40		[151]
$0.98[0.83\text{Bi}_{0.5}\text{Na}_{0.5}\text{TiO}_3\text{-}0.17\text{Bi}_{0.5}\text{K}_{0.5}\text{TiO}_3]\text{-}0.02\text{K}_{0.5}\text{Na}_{0.5}\text{NbO}_3$	<i>Rhombohedral</i> + <i>pseudo-cubic</i>	<i>Rhombohedral</i> + <i>distorted pseudo-cubic</i>	40		[151]
$0.94(\text{Bi}_{0.5}\text{Na}_{0.5})_2\text{TiO}_3\text{-}0.06\text{Ba}(\text{Zr}_{0.02}\text{Ti}_{0.98})_2\text{O}_3$	<i>Pseudo-cubic</i>	<i>Tetragonal</i> ; <i>Tetragonal</i> + <i>Rhombohedral</i> <i>after few electric fields cycles</i>	≈30	Irreversible.	[184]
$0.94(\text{Bi}_{0.5}\text{Na}_{0.5})_2\text{TiO}_3\text{-}0.06\text{Ba}(\text{Zr}_x\text{Ti}_{1-x})_2\text{O}_3$ ( $x = 0.02, 0.1, 0.15$ )	<i>Pseudo-cubic</i>	<i>Rhombohedral</i> / <i>tetragonal</i>	20–50 (DC poling)	Reversible for $x = 0.15$ .	[185]
$0.86\text{Bi}_{0.5}\text{Na}_{0.5}\text{TiO}_3\text{-}0.14\text{K}_{0.5}\text{Na}_{0.5}\text{NbO}_3$	<i>Pseudo-cubic</i>	<i>Distorted Pseudo-cubic</i>	10	Reversible.	[157]

structural changes induced by the chemical substitutions, helping the reader to better following the description of the electric-field-induced structural transformations discussed in the subsequent sections.

Fig. 10 shows the phase diagrams of various binary BNT-based solid solutions realized in combination with other compounds, namely barium titanate ( $\text{BaTiO}_3$  (BT) [145]), bismuth-potassium titanate ( $\text{Bi}_{0.5}\text{K}_{0.5}\text{TiO}_3$  (BKT) [146]), potassium-sodium niobate ( $\text{K}_{0.5}\text{Na}_{0.5}\text{NbO}_3$  (KNN) [147]) and strontium titanate ( $\text{SrTiO}_3$  (ST) [148]). These materials undergo significant modifications of the crystal structure depending on the particular composition and display the presence of morphotropic phase boundaries, where dielectric and piezoelectric properties are usually maximized.

The phase diagram relative to the unpoled (1-x)BNT-xBT system [145] reported in Fig. 10a indicates the presence of a polar rhombohedral  $R3c$  phase in the range  $x < 0.04$  at temperatures below 150 °C. In the range  $0.05 < x < 0.07$ , the system exhibits a morphotropic phase boundary (MPB), characterized by the coexistence of the polar  $R3c$  phase with the weakly-polar tetragonal  $P4bm$  structure. For  $x > 0.07$ , the rhombohedral phase is no longer present and the  $P4bm$  structure remains the only stable phase until  $x \approx 0.10$ , where the polar structure  $P4mm$  appears. This phase coexists with the  $P4bm$  phase until  $x \approx 0.11$ , where the latter phase disappears, leaving room only for the  $P4mm$  structure (Fig. 10a).

The (1-x)BNT-xBKT system [146] also shows a cross-over from rhombohedral to tetragonal phase by increasing the amount of BKT at room temperature, with the presence of a morphotropic phase boundary in the range  $0.1 < x < 0.2$  (Fig. 10b). With increasing temperature, the tetragonal system first transforms to a pseudo-cubic and then to a cubic structure in the entire compositional range, with the transition temperatures strongly dependent on the composition.

The phase diagram of the (1-x)KNN-xBNT system [147] highlights various transformations and the presence of MPBs (Fig. 10c). With increasing KNN amount, the structure initially moves towards a less polar and less distorted structure, up to about 85% KNN, where the system becomes again more polar, with a mixture of  $P4mm$  and  $Pm$  phases. At higher BNT content ( $>0.15\%$ ), the system transforms into a mixture of tetragonal  $P4bm$  and cubic  $Pm\bar{3}m$  phases, and subsequently shows the coexistence of tetragonal  $P4bm$  and rhombohedral  $R3c$ , until becoming purely rhombohedral  $R3c$ . The temperature-induced structure variations strongly depend on the initial composition, but generally reflect the stabilization of a weakly-polar and less-distorted structure with increasing temperature.

The phase diagram in Fig. 10d [148] indicates that the addition of  $\text{SrTiO}_3$  (ST) determines a transformation from rhombohedral to pseudo-cubic (tetragonal) structure at about 20 mol% of ST at room temperature. By increasing the amount of ST, the transformation temperatures ( $T_b$ ,  $T_{R-T}$  and  $T_m$ ) continuously decrease, indicating that the addition of ST favours the transformation to a weakly-polar/non-polar state. The phase boundaries have been traced based on the identifications of the characteristic temperatures from dielectric (open symbols) and Raman spectroscopy (solid symbols). These could be susceptible to variations, due to the data scatter caused by different processing conditions and by different techniques and analyses employed. For instance, a different structural evolution at room temperature has been reported by Kim et al. [149] and can be also observed on the horizontal axis of the ternary phase diagram in Fig. 10e [150].

The phase diagrams of BNT-ST-KN (Fig. 10e) [150] and BNT-BKT-KNN (Fig. 10f) [151] have been selected as examples of ternary phase diagrams reported for BNT-based compounds, with the purpose of illustrating two types of MPBs, labelled as MPB(I) and MPB(II) in Fig. 10e and f. In particular, MPB(I) is located between the rhombohedral and tetragonal ferroelectric phases, where the system shows maximized dielectric permittivity and piezoelectric coefficients. MPB(II) instead separates rhombohedral ferroelectric and pseudo-cubic/tetragonal relaxor phases. The compositions around MPB(II) exhibit a small piezoelectric constant, but they experience large strain under the application of an electric field.

### 3.2. Summary of $\text{Bi}_{0.5}\text{Na}_{0.5}\text{TiO}_3$ -based materials undergoing electric field-induced transformations

The selection of BNT-based systems considered above is not exhaustive of all the compositions in which electric field-induced transformations have been observed. Table 1 lists a much larger number of BNT-based materials undergoing EFITs. It summarizes the initial structures and the electric field-induced structures at room temperature, along with the critical electric fields and the characteristics of the field-induced transitions, wherever these information have been reported in the quoted references.

## 4. Electric field-induced phenomena in BNT-based perovskites

This section describes a series of electric field-driven transformations observed in different BNT-based perovskites. Initially, a detailed summary of the possible effects of temperature and frequency on EFITs is given, with a thorough description of the hysteresis loops features. Subsequently, a number of phenomena observed in BNT-based compounds are comprehensively discussed. These have been identified as: (i) bias field-induced shifts of characteristic temperatures; (ii) creation and destruction of morphotropic phase boundaries; (iii) ferroelectric-to-relaxor-like reverse transformations; (iv) metastable electric field-induced domain structures; (v) large piezoelectricity by poling below the coercive field; (vi) deviations from Rayleigh-type behaviour; (vii) cascade phenomena during under DC electric fields; (viii) heterogeneous electric field-induced transitions discussed in relation to the effect of grain orientation and core-shell microstructures; (ix) rotostriction, rotopolarization and polarization twist; (x) criticality phenomena; and (xi) acoustic emissions during electric field-induced transitions. The section is concluded with a discussion on the role of electric field-induced transitions on the fatigue behaviour of BNT-based materials.

#### 4.1. Temperature dependence of electric field-induced transformations

As extensively discussed for the case of undoped BNT, a general effect of the temperature on the structure of BNT-based compounds is represented by thermally-induced transformations from a non-ergodic relaxor/ferroelectric state to an ergodic relaxor state during heating. This is also shown in the phase diagrams of the BNT-based solid solutions reported in Fig. 10. Several characteristic temperatures corresponding to various thermally-driven events occurring during heating/cooling can be identified by the temperature dependence of dielectric, piezoelectric, and mechanical properties, as well as from the characteristics of the hysteresis loops.

For the temperature dependence of dielectric permittivity and loss, the focus is given to the system (1-x)BNT-xBT. Fig. 11a–d [186] refer to four different unpoled compositions in the range  $0.04 \leq x \leq 0.11$ . During heating, the first anomaly observed in  $x = 0.04$  and  $x = 0.11$  occurs at similar temperatures in both compositions, which both lie outside the MPB region. This anomaly corresponds to a sharp and frequency-independent peak in permittivity and loss factor (see blue dashed lines in Fig. 11a and d). Beyond this peak, significant frequency dispersion arises in the permittivity. This anomaly is not observed in the compositions  $x = 0.07$  and  $x = 0.09$ , which show a much greater frequency dispersion and a frequency-dependent local maximum in the permittivity, identified with  $T_{LM}$  (see green dashed lines in Fig. 11b and c). A similar anomaly is observed also in the compositions  $x = 0.04$ , and  $0.11$  at higher temperatures (see green dashed lines in Fig. 11a and d). Upon further heating, the frequency dispersion drops at a particular temperature  $T_{RE}$ , which does not significantly vary with the composition (Fig. 11a–d). Similarly to undoped BNT, all compositions exhibit a maximum value of the permittivity at the temperature  $T_m$ , whose position does not show a visible dependence on the composition (see pink dashed lines in Fig. 11a–d) [186]. Based on TEM studies, it was demonstrated that both the temperatures  $T_{RE}$  and  $T_m$  do not identify structural transformations [145]. It is widely accepted that the temperature dependence of dielectric permittivity and loss in BNT-BT can be rationalized by the thermal evolution and reversible mutual transformations of polar nanoregions with  $R3c$  and  $P4bm$  symmetries, as initially reported in Ref. [187].

Fig. 11e and 11f show the difference between the temperature dependence of permittivity and loss of unpoled and poled samples for the composition  $x = 0.06$  [188]. It can be seen that the poled sample shows a sharp and frequency-independent anomaly in the low-temperature range, similar to that observed in  $x = 0.04$  and  $x = 0.11$ . This temperature is identified as the *ferroelectric-relaxor transition temperature*  $T_{F-R}$ .

Another important characteristic temperature in relaxors is the so called *freezing temperature*  $T_f$ , which is identified via the application of the Vogel-Fulcher (VF) relationship [189,190]:  $\omega = \omega_0 \exp\left[-\frac{E_A}{k_B(T_m - T_f)}\right]$ , where  $\omega$  is the angular frequency,  $\omega_0$  the pre-exponential factor,  $T_m$  the temperature corresponding to the permittivity maximum at the frequency  $\omega$ ,  $E_A$  the activation energy

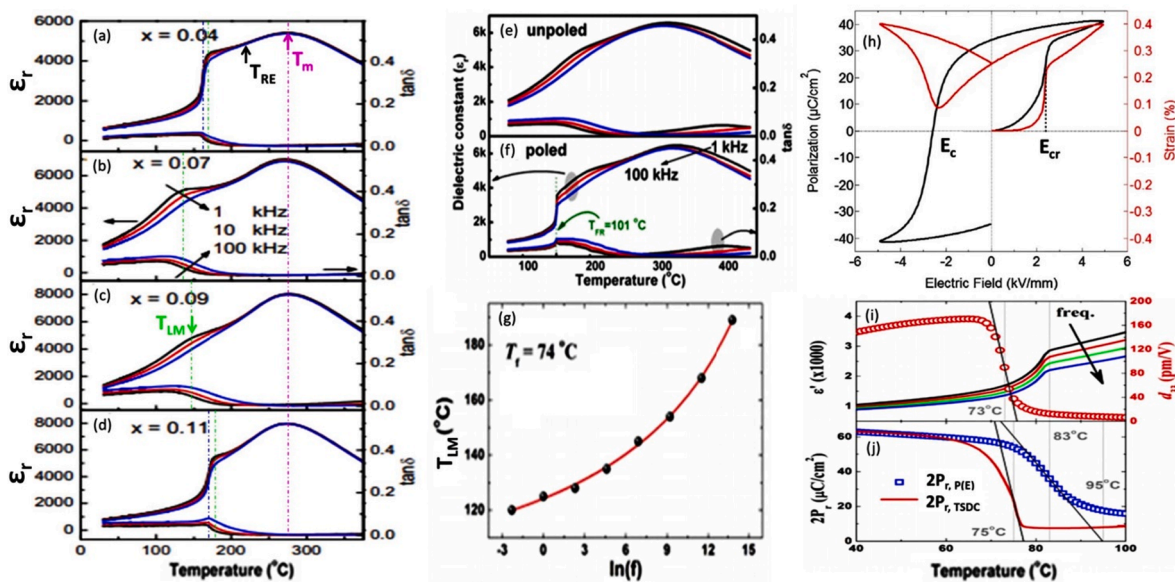


Fig. 11. (a)–(d) temperature dependence of dielectric permittivity and loss at different frequencies for various compositions (1-x)BNT-xBT [Reproduced from Ref. [186] <https://aip.scitation.org/doi/10.1063/1.3514093> with the permission of AIP Publishing]; dielectric properties and hysteresis loops of 0.94BNT-0.06BT: temperature dependence of dielectric permittivity and loss at different frequencies of unpoled (e) and poled (f) samples [Reproduced from Ref. [188] <https://aip.scitation.org/doi/10.1063/1.4983029> with the permission of AIP Publishing]; (g) Vogel-Fulcher fitting of the frequency shift of the temperature  $T_{LM}$  [Reproduced from Ref. [191] <https://aip.scitation.org/doi/10.1063/1.4805360> with the permission of AIP Publishing]; (h) polarization- and strain-electric field loops [Reproduced with permission from Ref. [192] Copyright 2019 Elsevier]; temperature dependence of permittivity (at different frequencies) and piezoelectric constant  $d_{33}$  (i); and remnant polarization obtained from P-E loops and thermally stimulated depolarization current measurements (j) [Reproduced with permission from Ref. [191] <https://aip.scitation.org/doi/10.1063/1.4805360> with the permission of AIP Publishing].

and  $k_B$  the Boltzmann constant. The VF fitting carried out considering the shift of the temperature  $T_{LM}$  observed in 0.94BNT-0.06BT gave a value of  $T_f = 74$  °C (see Fig. 11g) [191]. Below  $T_f$ , relaxor systems present a non-ergodic state, where polar nanoregions are “frozen”; nevertheless, these can grow in size, leading to the formation of ferroelectric domains during the application of an external field with sufficient magnitude. Once a long-range ferroelectric order is irreversibly induced by the applied field, the material starts to effectively behave as a proper ferroelectric, exhibiting piezoelectric activity, and similar hysteresis loops to those observed in conventional ferroelectrics. Typical examples of P-E and S-E loops reflecting an irreversible electric field-induced transition from non-ergodic relaxor to ferroelectric phase are shown in Fig. 11h. The electric field-induced transition occurs during the very first electrical cycle at the critical field indicated as  $E_{cr}$ . Once the ferroelectric phase is formed, an increase of the applied field beyond  $E_{cr}$  determines a further increase of polarization and strain in the induced ferroelectric state, mainly via a mechanism based on domain wall motion. By unloading the applied field, the macroscopic polarization reduces, until it reaches zero during field reversal at a particular field identified as the coercive field ( $-$ )  $E_C$ , similarly to the case of normal ferroelectrics. The coercive field can differ slightly or significantly from the field  $E_{cr}$ , depending on the kinetics of the field-induced transition that occurred during the first electrical cycle and of the domain switching process taking place during the successive cycles in the field-induced ferroelectric phase, as described in Ref. [192].

The field-induced long-range ferroelectric order can be destabilized during heating, above a specific temperature commonly defined as *depolarization temperature*  $T_d$ , where the system depolarizes, losing its overall piezoelectric response. The depolarization temperature is usually more preferably identified from the temperature dependence of the piezoelectric constant, or from the temperature dependence of the pyroelectric current, rather than from the temperature dependence of the dielectric permittivity and loss, as extensively discussed by Anton et al. [193]. This is shown in Fig. 11i, where  $T_d$  is identified with the temperature corresponding to the largest decrease of the piezoelectric constant ( $T_d = 73$  °C) and remnant polarization obtained from the thermally-stimulated depolarization current  $2P_{F,TSDC}$  ( $T_d = 75$  °C), as shown in Fig. 11j. Based on the results shown in Fig. 11i and 11j, Jo et al. concluded that in 0.94BNT-0.06BT,  $T_d$  coincides with the freezing temperature  $T_f$  [191]. The depolarization temperature  $T_d$  should not be confused with the temperature  $T_{F-R}$ , which represents the temperature where relaxor systems enter into the ergodic state during heating. The temperature  $T_{F-R}$  is usually higher than  $T_d$  [193], as also visible in Fig. 11i and j, where  $T_{F-R}$  is identified from the frequency-independent permittivity peak and from the largest drop of  $P_r$ . However, exceptional cases where  $T_{F-R}$  is lower than  $T_d$  have been also reported [194]. The thermally-induced depolarization processes should be distinguished between a loss of alignment of ferroelectric domains at  $T_d$ , and a miniaturization of detexturized ferroelectric domains at  $T_{F-R}$ . Based on Raman spectroscopy studies, it was demonstrated that the depolarization process in BNT-based materials occurs through the disruption of the hybridization in the Bi—O bonds [195]. Additional factors that influence the thermal depolarization process might be represented by the stresses developed at the interfaces between different crystallographic phases, which promote depolarization, and by the chemical pressure, which tends to stabilize the domain structure [196]. Various strategies have been developed to enhance the temperature stability of the piezoelectric properties in BNT-based ceramics [143], including composition variations [82,197–201], grain size modification [202] and quenching treatments after sintering [201,203,204]. A-site non-stoichiometry and chemical modifications in BNT ceramics determine significant changes in the characteristic temperatures of the thermal depolarization process [82]. The depolarization temperature  $T_d$  of

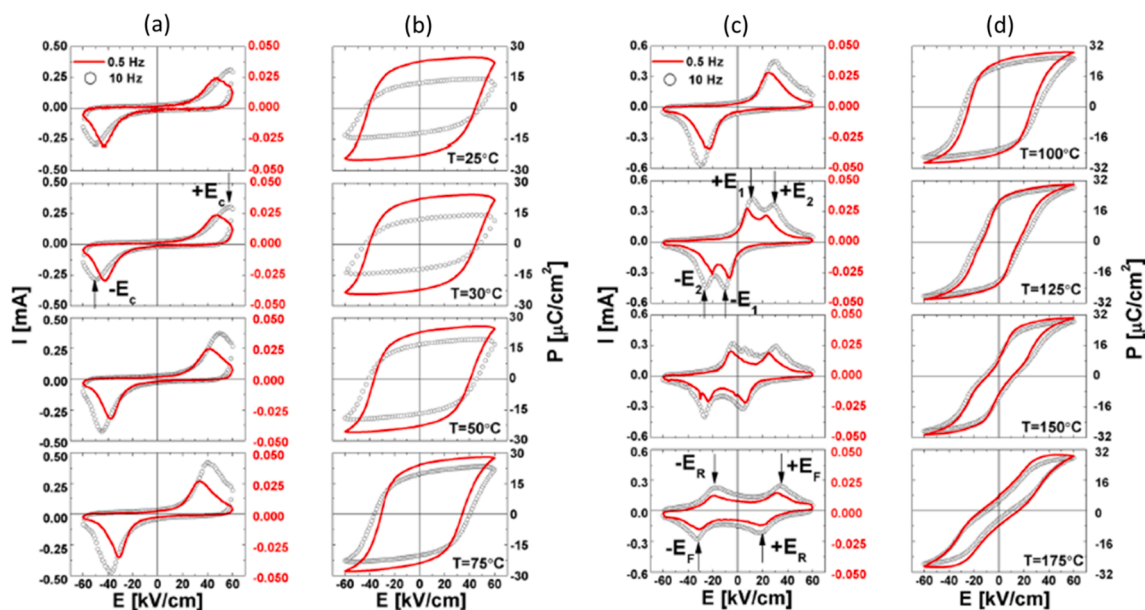
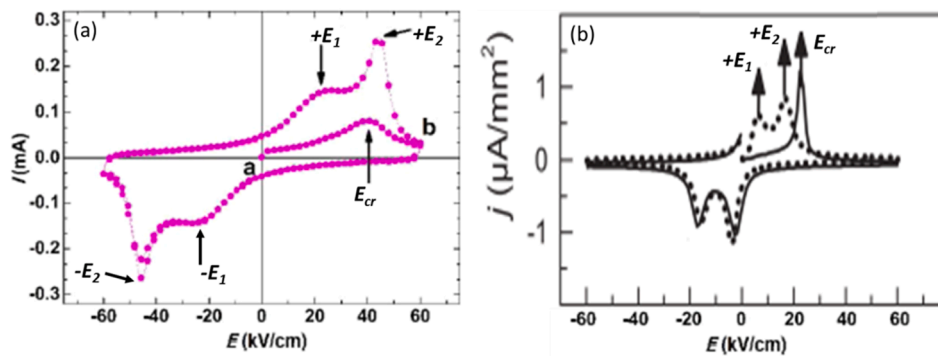


Fig. 12. Temperature and frequency dependence of I-P-E loops in the range 25 °C–75 °C (a)–(b) and 100 °C–175 °C (c)–(d) for 0.95[0.94(Bi<sub>0.5</sub>Na<sub>0.5</sub>)TiO<sub>3</sub> – 0.06BaTiO<sub>3</sub>] – 0.05CaTiO<sub>3</sub>. [Reproduced from Ref. [205] <https://aip.scitation.org/doi/full/10.1063/1.4812383> with the permission of AIP Publishing].



**Fig. 13.** Current-electric field hysteresis loops from the very first cycle of (a)  $0.95[0.94(\text{Bi}_{0.5}\text{Na}_{0.35}\text{Li}_{0.15})\text{TiO}_3 - 0.06\text{BaTiO}_3] - 0.05\text{CaTiO}_3$  [Reproduced with permission from Ref. [206] Copyright 2014 American Chemical Society] and (b)  $0.97(\text{Bi}_{0.5}\text{Na}_{0.5})\text{TiO}_3 - 0.03\text{BaTiO}_3$  doped with 0.5 mol% of Mn [Reproduced from Ref. [207] <https://aip.scitation.org/doi/full/10.1063/1.4876746?ver=pdfcov> with the permission of AIP Publishing].

(1-x)BNT-xBT ceramics was found to initially decrease with small additions of Ba (up to  $x = 0.06$ ) and to start increase again with larger Ba content (from  $x = 0.08$ ) [197]. Small additions of Fe and Mn (0.5–1.0 at.%) to BNT ceramics increase the depolarization temperature  $T_d$ , while larger additions ( $>1.5$  at.%) decrease  $T_d$  [198]. The introduction of Zn in 0.94BNT-0.06BT ceramics determines an increase of the depolarization temperature  $T_d$  [199–201]. An increase in grain size was found to increase  $T_d$  in BNT and 0.94BNT-0.06BT ceramics due to an increase in the unit cell distortion [202]. Similar retarding effects on the distortion-driven thermal depoling are produced by quenching treatments, as reported for various BNT-based ceramics [203,204].

The typical temperature dependence of the hysteresis loops observed in BNT-based materials is shown in Fig. 12a–d, which are relative to  $0.95[0.94(\text{Bi}_{0.5}\text{Na}_{0.5})\text{TiO}_3 - 0.06\text{BaTiO}_3] - 0.05\text{CaTiO}_3$  [205]. It can be noticed that the coercive field  $E_c$  of the field-induced ferroelectric phase decreases with increasing temperature, as observed in normal ferroelectrics. During heating, there is a particular temperature at which the current-electric field loops begin to show four current peaks, two along the positive electrical loading direction (indicated with  $+E_1$  and  $+E_2$ ) and two along the negative electrical loading direction (indicated with  $-E_1$  and  $-E_2$ ), as shown in Fig. 12c. This behaviour is observed in the range  $T_d \leq T < T_{F-R}$ .

It is essential to note that in order to not miss important electric field-induced events, it is necessary to monitor the signals during the entire electrical history, starting from the very first electrical cycle. Fig. 13 shows the current-electric field hysteresis loops of  $0.95[0.94(\text{Bi}_{0.5}\text{Na}_{0.35}\text{Li}_{0.15})\text{TiO}_3 - 0.06\text{BaTiO}_3] - 0.05\text{CaTiO}_3$  (Fig. 13a) [206] and  $0.97(\text{Bi}_{0.5}\text{Na}_{0.5})\text{TiO}_3 - 0.03\text{BaTiO}_3$  doped with 0.5 mol% of Mn (Fig. 13b) [207], including also the data recorded during the very first poling cycle (see for instance branch a-b in Fig. 13a).

It can be observed that the I-E loops of both materials show only one current peak in the first electrical cycle at  $E_{cr}$ , which identifies the critical field of the field-driven transformation from the non-ergodic relaxor to the ferroelectric state, and it may include also a contribution of domain switching. During field reversal, the first current peak at  $-E_1$  corresponds to the backward transition from the ferroelectric to the relaxor state. This is also supported by the fact that the polarization returns to zero nearby the field corresponding to the current peak. The second current peak at higher electric field  $-E_2$  is related to the forward relaxor-to-ferroelectric transformation along the negative direction. The described sequence of transitions repeats in the subsequent electrical cycle, and the I-E loops show the two current peaks at  $+E_1$  (ferroelectric-relaxor) and  $+E_2$  (relaxor ferroelectric) along the positive direction. By further increasing the temperature at  $T > T_{F-R}$ , the forward relaxor-to-ferroelectric transition reverses during unloading, as evidenced by the position of the current peaks: two peaks appear during loading at  $\pm E_F$  and two during unloading at  $\pm E_R$  (see Fig. 12d). The current peaks observed during loading at  $\pm E_F$  correspond to the transition from the ergodic relaxor to the ferroelectric state, while the current peaks during unloading at  $\pm E_R$  correspond to reverse transition from the metastable ferroelectric state to the ergodic relaxor phase.

The schemes reported in Fig. 14a–d provide the identification of additional characteristic fields of the described transition at  $T > T_{F-R}$  [208]. These include: (i) the field  $E_{ZP}$  (zero polarization field) indicating the field that reduces to zero the polarization induced during the previous electrical cycle (Fig. 14c, d); (ii) the field  $E_d$  (depoling field) that identifies the field corresponding to the crossing point of the tangents to the P-E loop at the initial and intermediate unloading stage (Fig. 14c, d); and (iii) the field  $E_{F-R}$  (ferroelectric-relaxor field) where the tangent to the P-E loop in the final unloading stage crosses the tangent to the first loading stage along the reverse direction (Fig. 14c, d). It should be noted that the characteristic fields  $\pm E_{F-R}$  are slightly different from the fields  $\pm E_R$  shown in Fig. 11d, as the latter are identified directly from the current peak position. The temperature dependence of the characteristic field  $E_d$  and  $E_{F-R}$  can be also used to identify  $T_d$  and  $T_{F-R}$  as the temperatures at which  $E_d = 0$  and  $E_{F-R} = 0$ , respectively (see Fig. 14e and f relative to 0.94BNT-0.06BT) [208].

The effect of temperature on the electric field-induced transitions can be observed also in the temperature dependence of the strain-electric field loops, which has been described in details in a previous review [27]. This has highlighted the significant difference between a *butterfly-like* shape with a sizeable remnant strain in the non-ergodic/ferroelectric phase, and the *sprout-like* shape with negligible remnant strain in the ergodic phase, for which BNT-based piezoceramics have been also classified as “incipient piezoelectrics” [27].

Detailed investigations by dynamical-mechanical analysis (DMA), differential scanning calorimetry (DSC) and dielectric

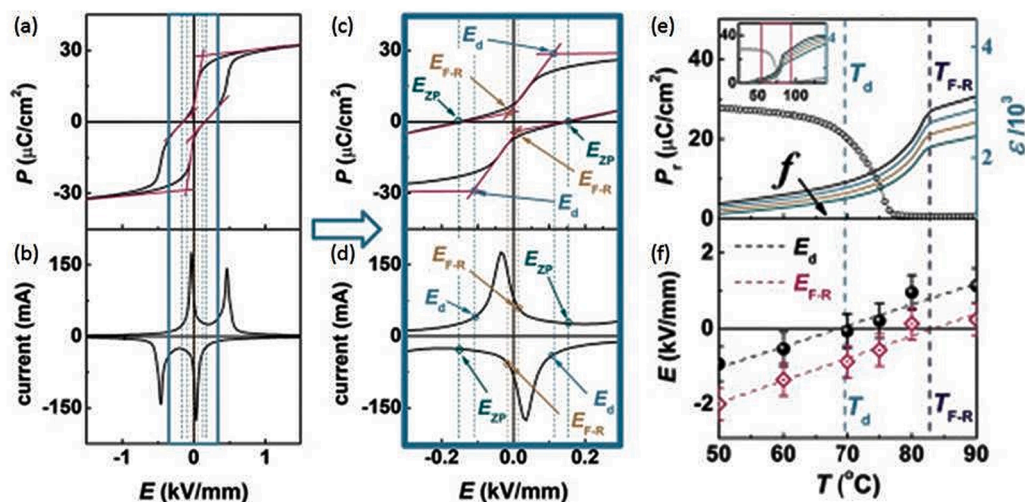


Fig. 14. Identification of characteristic fields from hysteresis loops (a)–(d); identification of  $T_d$  and  $T_{F-R}$  using the temperature dependence of remnant polarization and permittivity (e); and characteristic fields  $E_d$  and  $E_{F-R}$ . [Reproduced with permission from Ref. [208] Copyright 2019 Elsevier].

measurements on unpoled (1-x)BNT-xBT systems have identified additional characteristic temperatures (Figs. 15 and 16), and have contributed to enrich the BNT-BT phase diagram, as depicted in Fig. 16e, 16f [209].

The temperature  $T_C$  (indicated with  $T_{C+}$  and  $T_{C-}$  in the heating and cooling cycle, respectively) corresponds to the tetragonal-cubic phase transition and is identified from a local minimum in the storage modulus and a peak in the mechanical loss factor (Fig. 15a). The temperature  $T_S$  (indicated with  $T_{S+}$  and  $T_{S-}$  in the heating and cooling cycle, respectively), identified from a minimum in the storage modulus, a maximum in the mechanical loss factor (Fig. 15a, b), peaks in the DSC signal and by anomalies in the dielectric permittivity below the temperature corresponding to the dielectric maximum  $T_m$  (Fig. 16a–c), is linked to the tetragonal-rhombohedral transition [209]. It can be noticed that during heating, the temperature  $T_{S+}$  decreases with increasing BT content, and the corresponding

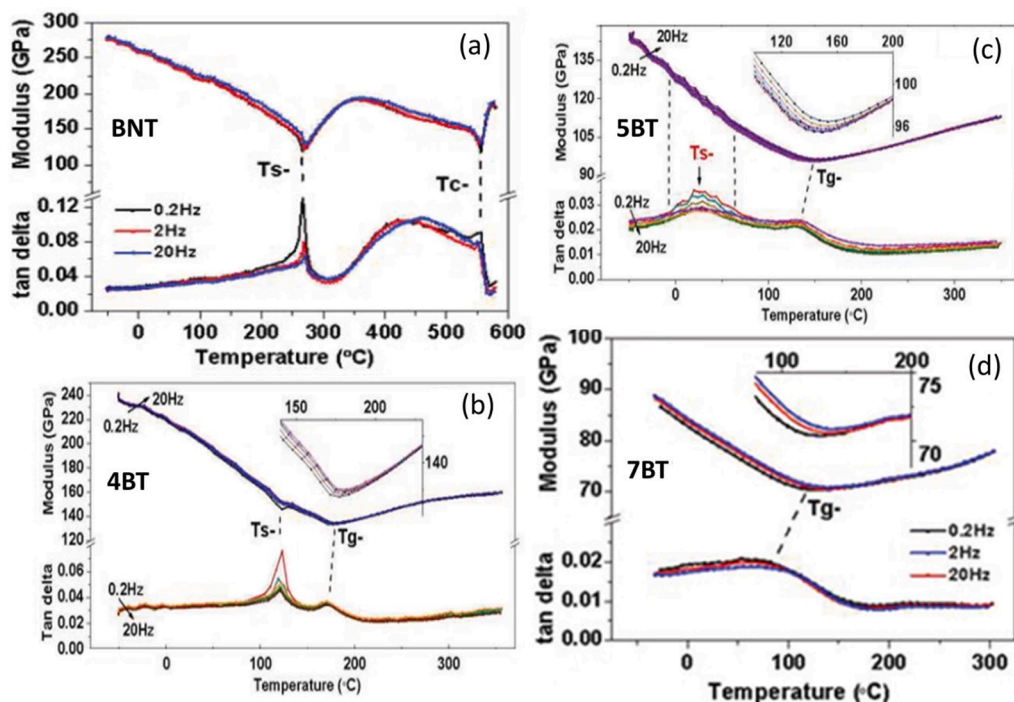
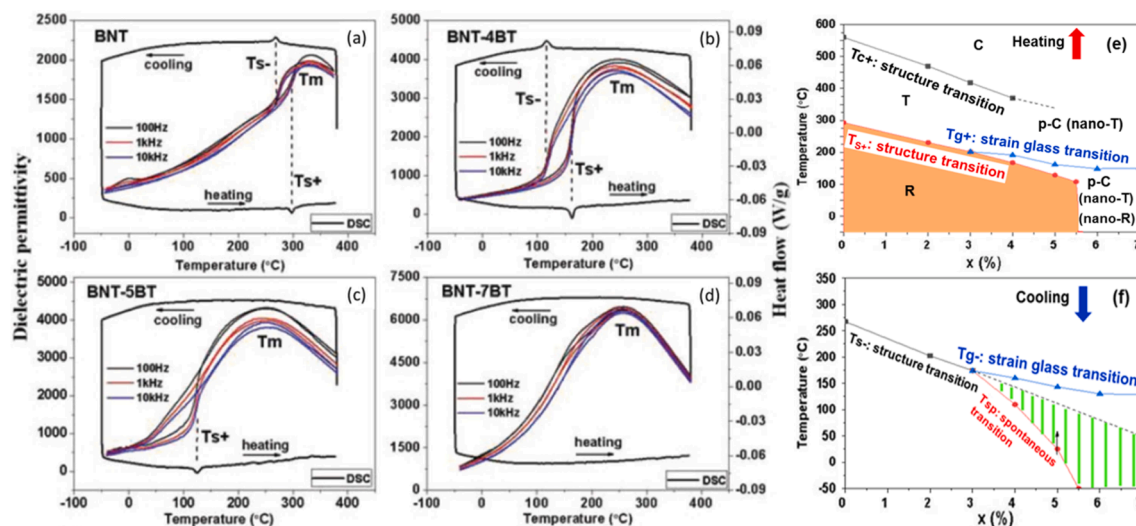


Fig. 15. Temperature dependence at different frequencies of storage modulus and mechanical loss factor for (a) BNT; (b) 0.96BNT-0.04BT; (c) 0.95BNT-0.05BT; and (d) 0.97BNT-0.03BT. [Reproduced from Ref. [209] <https://www.tandfonline.com/doi/pdf/10.1088/1468-6996/14/3/035008?needAccess=true> with permission from Taylor & Francis].



**Fig. 16.** (a)–(d): temperature dependence of dielectric permittivity and differential scanning calorimetry thermograms of BNT (a), 0.96BNT-0.04BT (b), 0.95BNT-0.05BT (c), and 0.93BNT-0.07BT (d). [Reproduced from Ref. [209] <https://www.tandfonline.com/doi/pdf/10.1088/1468-6996/14/3/035008?needAccess=true> with permission from Taylor & Francis]; (e)–(f) Phase diagrams of  $(1-x)\text{BNT}-x\text{BT}$  ( $0 \leq x \leq 0.07$ ) during heating (e) and cooling (f). [Data obtained from the authors of Ref. [209]].

anomalies in the permittivity are absent for  $x > 0.05$  (Fig. 16d). During cooling, the temperature  $T_S$  also decreases with increasing BT content until  $x = 0.04$ , where the largest hysteresis on the temperature  $T_S$  can be observed (Fig. 16b). At  $x > 0.04$ , the temperature  $T_S$  could not be detected in the DSC and in the permittivity during cooling (Fig. 16c, 16d), while it could be identified in the DMA tests at low frequencies in ceramics with  $x = 0.05$ , but not at larger  $x$  (Fig. 15c, d). Additionally, compositions with  $x \geq 0.03$  display another characteristic temperature  $T_g$  (indicated with  $T_{g+}$  and  $T_{g-}$  in the heating and cooling cycle, respectively), corresponding to a broad and frequency-dispersive anomaly in the storage modulus and loss factor (Fig. 15b–d). This temperature has been defined as “strain glass transition temperature” [209], below which domains with short-range ordering are kinetically frozen, identifying the transition into a non-ergodic state during cooling and into an ergodic state during heating. For compositions with  $x > 0.04$ , the transition temperature  $T_S$  is not easily detected during cooling (Fig. 16c, d) because the “strain freezing” occurring at  $T_{g-}$  makes the kinetics of the T-R transition much slower [209]. A linear extrapolation allows identifying the ideal temperatures  $T_{S-}$  during cooling (see dashed red line in Fig. 16f) so that they can be distinguished from the temperatures obtained in the DMA tests at different frequencies. The latter are labelled as  $T_{sp}$  (spontaneous transition temperature), below which the short-range non-ergodic relaxor state spontaneously transforms into a long-range ordered state. The presence of the strain glass transition during cooling with  $T_{g-} > (T_{S-}, T_{sp})$  is the reason why there are no anomalies in the permittivity and DSC data at  $T_S$  during cooling, and justifies the presence of the anomalies at  $T_{S+}$  during the heating cycles. The area of the phase diagram with green lines indicates a metastable strain glass state, which evolves towards a long-range ordered state, if sufficient time is given for the transition to occur under isothermal conditions [209]. The temperature  $T_g$  was proved to coincide with the temperature corresponding to the minimum value of the elastic modulus identified in previous studies [210]. Subsequent investigations on unpoled and poled 0.93BNT-0.07BT have shown that the unpoled sample exhibits a broad minimum in the storage modulus at the temperature corresponding to the shoulder in the dielectric permittivity ( $T_{LM}$ ), while no peak was found in the DSC thermogram (Fig. 17a–c) [211]. On the contrary, the poled sample showed a sharp minimum in the storage modulus and in the heat flow, along with a maximum in the mechanical loss factor at approximately 25 °C above the temperature  $T_{F-R}$  (Fig. 17d–e) [211]. It should be noticed that in the poled sample, the temperature corresponding to the minimum storage modulus does not coincide with the temperature of the permittivity local maximum  $T_{LM}$ .

More recent studies based on the measurement of the Young’s modulus on  $(1-x)\text{BNT}-x\text{BT}$  have further elucidated the intriguing interconnections between the anomalies in the mechanical and dielectric behaviour and the thermal evolution of the structure [212]. For  $x = 0.03$ , the Young’s modulus shows only one minimum in both unpoled and poled samples, at a temperature coincident with  $T_{F-R}$  (Fig. 18a, 18b). On the other hand, the temperature corresponding to the maximum of the Young’s modulus was identified as the Burn’s temperature  $T_B$  ( $T_B = 723$  °C). In the composition  $x = 0.06$ , the Young’s modulus of the poled sample showed an additional sharp minimum at a temperature slightly higher than  $T_{F-R}$  (Fig. 18c, d) [212]. Additionally, a broad local minimum was observed in both the unpoled and poled samples at a temperature  $T_{me} > T_{F-R}$  coincident with the temperature corresponding to the permittivity shoulder (Fig. 18c, d). The temperature  $T^*$  located above the dielectric shoulder indicates the particular temperature beyond which the temperature dependence of the Young’s moduli of unpoled and poled samples becomes undistinguishable (Fig. 18c, d). In the composition  $x = 0.12$ , the temperature corresponding to the minimum value of the elastic modulus in the poled samples is visibly larger than that of the unpoled sample (Fig. 18e, f). It should be also noticed that  $T_{me}$  does not coincide with the temperature corresponding to the local maximum in the dielectric permittivity [212].

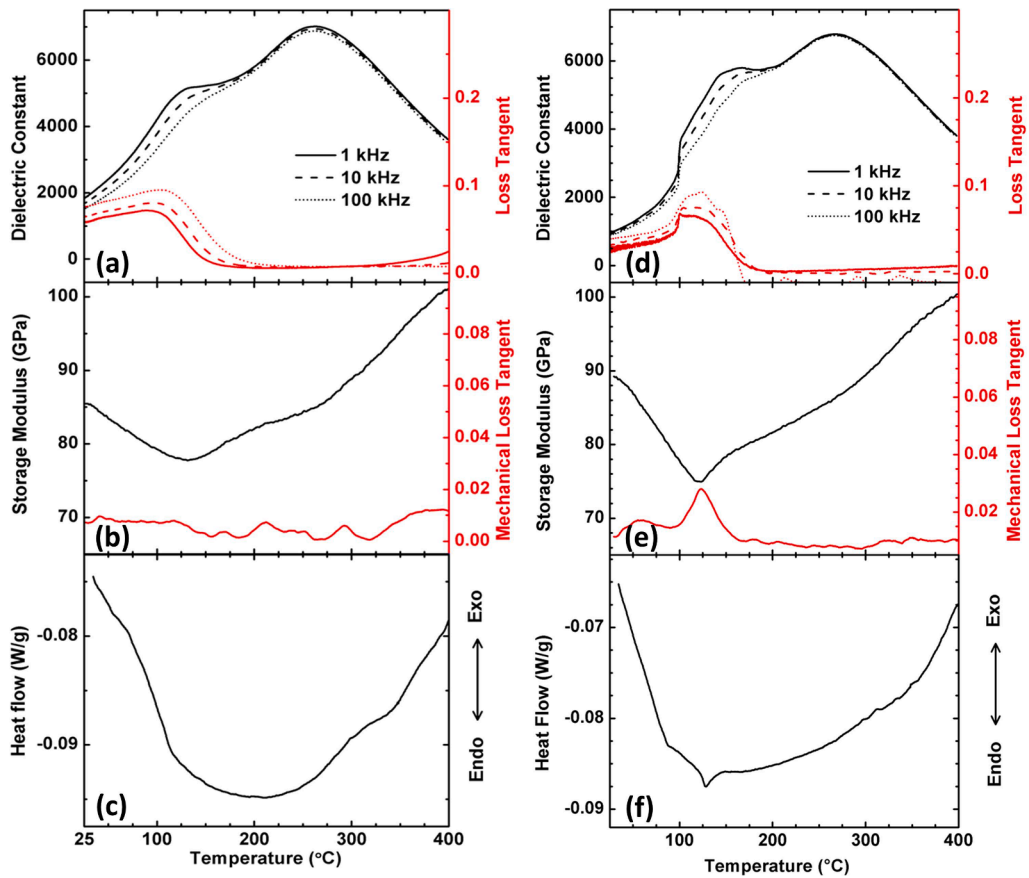


**Fig. 17.** Temperature dependence of dielectric permittivity and loss, storage modulus and mechanical loss, and heat flow in a DSC thermogram for unpoled (a)–(c) and poled (d)–(f) 0.93BNT-0.07BT ceramics. [Reproduced with permission from the authors of Ref. [211]].

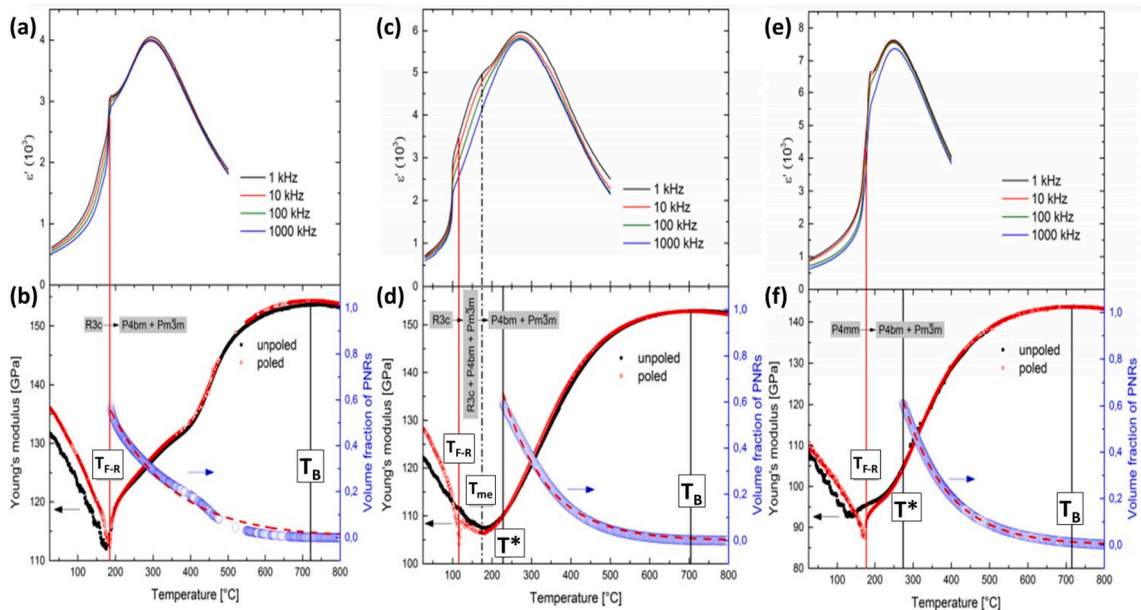


**Fig. 18.** Correspondence between anomalies identified in the temperature dependence of permittivity and Young's modulus for the (1-x)BNT-xBT systems: (a)–(b)  $x = 0.03$ ; (c)–(d)  $x = 0.06$ ; and (e)–(f)  $x = 0.12$ . The dielectric data are relative to poled samples, while mechanical data relative to both unpoled and poled samples. The latter plots contain also the thermal evolution of the volume fraction of polar nanoregions. [Reproduced with permission from Ref. [212] <https://journals.aps.org/prb/abstract/10.1103/PhysRevB.95.024104> Copyright 2017 American Physical Society].

#### 4.2. Frequency/rate dependence of electric field-induced transformations

It is well known that domain switching in ferroelectric/ferroelastic materials is a rate-dependent process, as demonstrated by the frequency dependence of polarization, coercive field, strain and coercive stress in polarization–electric field and strain–stress curves [213,214]. Generally, in P-E, S-E and S- $\sigma$  plots, both the coercive field and coercive stress increase, while the maximum polarization and maximum strain decrease with increasing the frequency/rate of the applied field. This is due to the fact that domain switching is a thermally-activated phenomenon and therefore longer exposure to applied electric fields leads to a large extent of the switching process [213].

The effect of frequency/rate in BNT-based materials undergoing EFITs presents specific features worthy of discussion. The critical field  $E_{cr}$  in the very first electrical loading in the non-ergodic phase and the coercive field  $E_c$  in the field-induced ferroelectric phase have both been found to increase with increasing the frequency of the alternating field in different BNT-based materials [27,215].

When the relaxor-to-ferroelectric transition can be reversed by reversing the applied field, both the characteristic fields  $\pm E_1$  and  $\pm E_2$ , respectively corresponding to the reverse and forward transition, increase with increasing the frequency of the applied field [205]. Nonetheless, it was argued that domain switching/back switching may occur concurrently to the field-induced transitions and that both processes have different kinetics [37]. However, it is still unclear which of the two phenomena occurs faster, as evidenced by two contradicting views reported in the literature. In a study on  $0.94(\text{Bi}_{0.5}\text{Na}_{0.5})\text{TiO}_3\text{-}0.06\text{Ba}(\text{Zr}_{0.02}\text{Ti}_{0.98})\text{O}_3$ , Glaum et al. have proposed that the reverse ferroelectric-to-relaxor transition occurs faster than domain switching [184]. Meanwhile, in a subsequent study on the system  $[(\text{Bi}_{0.5}\text{Na}_{0.5})_{0.95}\text{Ba}_{0.05}]_{0.98}\text{La}_{0.02}\text{TiO}_3$ , Han et al. proposed that domain switching occurs relatively fast, while the phase transitions have slower kinetics; therefore, the relaxor/weakly-polar phase appears during field reversal (between the fields  $E_1$  and  $E_2$ ) only during electrical cycles with low loading rate [37], as also reported for various antiferroelectric systems [216,217]. Hence, under slow loading rates, the field required for the E-induced transitions should be smaller than the field inducing domain switching, and therefore, polarization reversal was believed to mainly occur through the sequence of two phase transitions (ferroelectric-to-relaxor and relaxor-to-ferroelectric), rather than through domain switching [37].

When the relaxor-to-ferroelectric transition reverses just during field unloading (in ergodic relaxors), the characteristic fields  $\pm E_F$  and  $\pm E_R$  corresponding to the forward and reverse E-induced transitions were found to respectively increase and decrease with increasing frequency, as reported for the case of  $0.95[0.94\text{Bi}_{0.5}\text{Na}_{0.5}\text{TiO}_3\text{-}0.06\text{BaTiO}_3]\text{-}0.05\text{CaTiO}_3$  [205]. In ergodic relaxors, the maximum polarization and strain usually decrease with increasing frequency [27,205,215,218,219]. However, it was observed that the maximum polarization in the ergodic phase has a smaller frequency dependence than in the ferroelectric/non-ergodic relaxor phase [205]. On the other hand, the remnant polarization and remnant strain have shown inconsistent trends in both non-ergodic and ergodic phases, sometimes increasing [215,220], while other times decreasing with increasing frequency [219]. These variations can be probably attributed to the competing kinetics of the reverse transitions and domain back-switching.

An anomalous rate effect was reported for  $0.8\text{Bi}_{0.5}\text{Na}_{0.5}\text{TiO}_3\text{-}0.2\text{Bi}_{0.5}\text{K}_{0.5}\text{TiO}_3$  [220], in which an electric field-induced transformation from a purely rhombohedral phase to a mixed rhombohedral-tetragonal phase was only observed at electrical loading rates greater than  $2.5\text{ kV mm}^{-1}\text{ s}^{-1}$ , but not below this threshold. This was attributed to the presence of residual stresses that would inhibit the transition at lower rates, and to the fact that at lower rates, the coercive field might have been smaller than the critical field inducing the rhombohedral-to-tetragonal transformation [220]. However, the complete electrical history was not reported and definite conclusions could not be drawn. On the contrary, recent experiments carried out on  $0.88\text{Bi}_{0.53}\text{Na}_{0.47}\text{TiO}_3\text{-}0.12\text{BaTiO}_3$  by varying the frequency of the applied field in the range  $10^{-4}\text{-}10^2\text{ Hz}$ , evidenced a gradual suppression of the relaxor-to-ferroelectric transition with increasing frequency [221]. The experiments were carried out on freestanding samples and did not allow heat dissipation since the samples were not in contact with metal parts as occurs in common testing setup. The suppression of the phase transition was mainly attributed to kinetic effects and partially to the self-heating of the sample, whose temperature exponentially increased with increasing frequency and further prevented a long-range ferroelectric state to be established [221]. However, recent experiments have demonstrated that the application of THz electric field pulses of about  $155\text{ kV/cm}$  intensity at  $200\text{ K}$  for a time duration as short as  $20\text{ ps}$  on BNT ceramics produces detectable changes in reflectivity that are due to a structural transition from the monoclinic weakly-polar phase  $Cc$  to the strongly polar phase  $R3c$  [222]. Although, the extent of the THz field-induced transition is lower than that driven under DC poling conditions, these results indicate that the BNT structure is also able to transform under THz irradiation [222].

Additional rate effects on the electric field-induced processes occurring in non-ergodic and ergodic states in BNT-based materials have been studied through the dependence of the hysteresis loops area ( $\langle A \rangle$ ) on the frequency ( $f$ ) at different electric field amplitude ( $E_0$ ), via empirical laws of the type [223–226]:

$$\langle A \rangle \propto f^\alpha E_0^\beta \quad (1)$$

where  $\alpha$  and  $\beta$  are fitting parameters. This approach is based on the idea that the hysteresis loop area is related to the energy dissipation caused by the underlying process; therefore, modifications of the scaling law may reflect different electric field-induced processes. The dependence of  $\ln \langle A \rangle$  on  $\ln E_0$  has shown common features in BNT [226],  $0.94\text{BNT}\text{-}0.06\text{BT}$  [223,224] and  $0.96(\text{Bi}_{0.5}\text{Na}_{0.5})\text{TiO}_3\text{-}0.04\text{BiAlO}_3$  [225]. These features are characterized by a linear trend at low amplitudes  $E_0 \leq E_{c1}$  and high amplitudes  $E_0 \geq E_{c2}$ , and by a non-linear behaviour for intermediate values of  $E_0$  ( $E_{c1} \leq E_0 \leq E_{c2}$ ) at room temperature (Fig. 19a, b). In BNT, these dependences have been observed at a frequency of  $0.1\text{ Hz}$  (Fig. 19a) [226], while in  $0.96(\text{Bi}_{0.5}\text{Na}_{0.5})\text{TiO}_3\text{-}0.04\text{BiAlO}_3$  at  $1\text{ Hz}$  [225], and in  $0.94\text{BNT}\text{-}0.06\text{BT}$  at  $1\text{ Hz}$  (Fig. 19b) and  $10\text{ Hz}$  [223,224]. In the latter, when the frequency was lowered to  $0.01\text{ Hz}$ , only two stages with a linear  $\ln \langle A \rangle \text{-} \ln E_0$  trend were found at room temperature (Fig. 19c) [223]. It was observed that the field  $E_{c1}$  had a negligible frequency dependence, while the field  $E_{c2}$  significantly decreased with decreasing frequency. Therefore, the linear scaling in the low  $E_0$

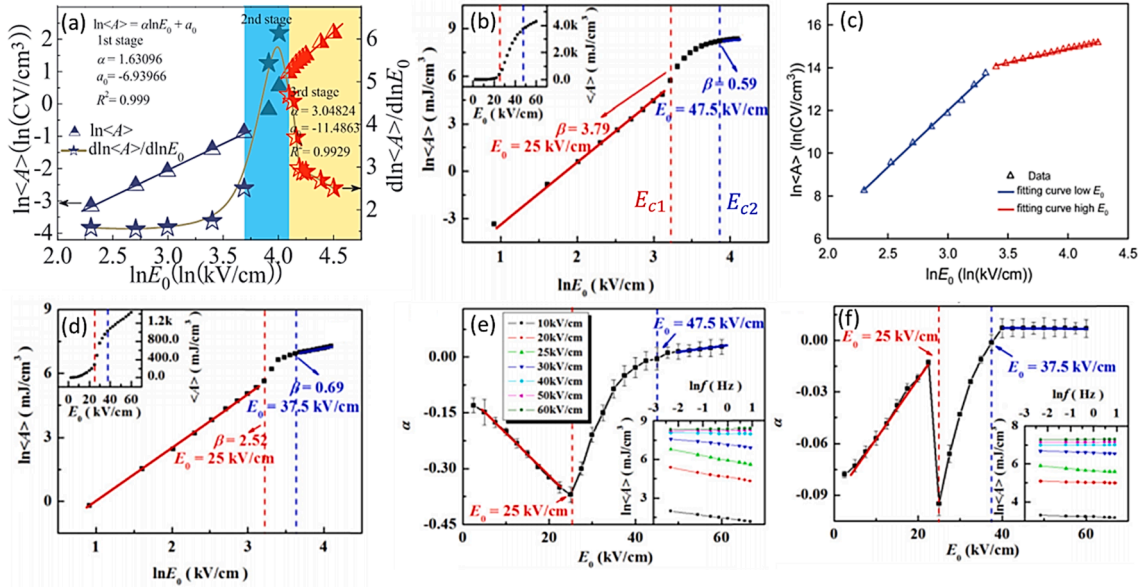


**Fig. 19.** (a)–(d) Dependence of the ferroelectric characteristics on the electric field amplitude and frequency in: (a) BNT at room temperature and 0.1 Hz [Reproduced with permission from Ref. [226] Copyright 2019 Elsevier]; (b) 0.94BNT-0.06BT at room temperature and 1 Hz [Reproduced with permission from Ref. [223] Copyright 2014 John Wiley and Sons]; (c) 0.94BNT-0.06BT at room temperature and 0.01 Hz [Reproduced with permission from Ref. [224] Copyright 2016 Royal Society of Chemistry]; (d) 0.94BNT-0.06BT at 110 °C and 1 Hz. (e)–(f) Dependence of the exponent  $\alpha$  on the electric field amplitude, as obtained from the plots in the insets, for: (e) 0.94BNT-0.06BT at room temperature; and (f) 0.94BNT-0.06BT at 110 °C. [Figures d to f are reproduced with permission from Ref. [223] Copyright 2014 John Wiley and Sons].

region ( $E_0 \leq E_{c1}$ ) was attributed to the reversible motion of 180° domain walls. By increasing the amplitude  $E_0$ , the switching of 180° and non-180° domains can occur, with the latter proceeding at a greater extent at lower frequencies. If the frequency is low enough, the field  $E_{c2}$  approaches  $E_{c1}$  and the second non-linear stage disappears [223]. Three-stage behaviour was also found in the ergodic phase of 0.94BNT-0.06BT at 110 °C and 1 Hz (Fig. 19d) [223]. Additionally, the slope  $\alpha$  of the plot  $\ln \langle A \rangle - \ln f$  in 0.94BNT-0.06BT has also shown three stages, depending on the amplitude  $E_0$  [223]. At room temperature and low  $E_0$ ,  $\alpha$  linearly increases toward negative values with increasing  $E_0$  until 25 kV/cm, above which a non-linear increase towards positive values, followed by a linear increase above 47.5 kV/cm, can be observed (Fig. 19e) [223]. At 110 °C, in the ergodic relaxor phase, the parameter  $\alpha$  showed also a three-stage dependence on the field amplitude  $E_0$ . By increasing  $E_0$ ,  $\alpha$  linearly increases towards the positive side until  $E_0 = 25$  kV/cm. In the range 25–37.5 kV/cm,  $\alpha$  increases non-linearly, while beyond 37.5 kV/cm, it remains constant with further increase of  $E_0$  (Fig. 19f). The first stage was attributed to the rotation and alignment of nanodomains; the second stage to growth of nanodomains within ferroelectric domains, and the third stage to polarization extension mechanisms. The values of  $\alpha$  at 110 °C are smaller than those obtained at room temperature, indicating a smaller sensitivity to the frequency at higher temperature, which is in agreement with the previously-discussed observations in 0.95[0.94Bi<sub>0.5</sub>Na<sub>0.5</sub>TiO<sub>3</sub>-0.06BaTiO<sub>3</sub>]-0.05CaTiO<sub>3</sub> [205].

#### 4.3. Bias field-induced shifts of characteristic temperatures

In BNT-based materials, the application of an electric field bias, even smaller than the critical field, could cause a shift of the characteristic temperatures of the thermally-induced transformations during heating. Experiments on poled  $(1-x)\text{Bi}_{0.5}\text{Na}_{0.5}(\text{Ti}_{0.995}\text{Mn}_{0.005})\text{O}_3-x\text{Ba}(\text{Ti}_{0.995}\text{Mn}_{0.005})\text{O}_3$  piezoceramics with  $x = 0.03, 0.06,$  and  $0.09$  (BNT-100xBT:Mn) have shown a constant increase of the depolarization temperature  $T_d$  by increasing the magnitude of an external bias applied along the poling direction, in all of the three compositions examined [227]. A similar trend was shown by the ferroelectric-to-relaxor transition temperature  $T_{F-R}$ , except for the composition BNT-3BT:Mn, in which  $T_{F-R}$  remained unchanged with increasing bias field (Fig. 20a). The increase of  $T_d$  was attributed to the stabilization of the macroscopic polarization by the applied bias field. The absence of a shift of  $T_{F-R}$  (temperature related to the loss of long-range interaction between dipoles) with increasing bias field in BNT-3BT:Mn was imputed to the presence of rhombohedral domains, as opposed to BNT-6BT:Mn and BNT-9BT:Mn, which had a higher presence of domains with tetragonal structure [227]. A recent study on the effect of bias fields in 0.94BNT-0.06BT single crystals has reported a linear increase of  $T_d$  of about 160 °C with increasing bias field from 0 kV/cm to 0.40 kV/cm [228]. Additionally, it was found that the temperature  $T_{LM}$ , corresponding to the permittivity local maximum, exhibits a V-type dependence on the field bias (Fig. 20b). This phenomenon, which is analogous to that shown by the variation of the temperature  $T_m$  in conventional lead-based relaxors [229], was attributed to the presence of random fields, which oppose the applied bias and reduce  $T_{LM}$  until a minimum value at the threshold bias  $E_{th}$ . At larger bias fields, the random fields can be overcome and  $T_{LM}$  starts increasing with increasing bias field (Fig. 20b) [228].

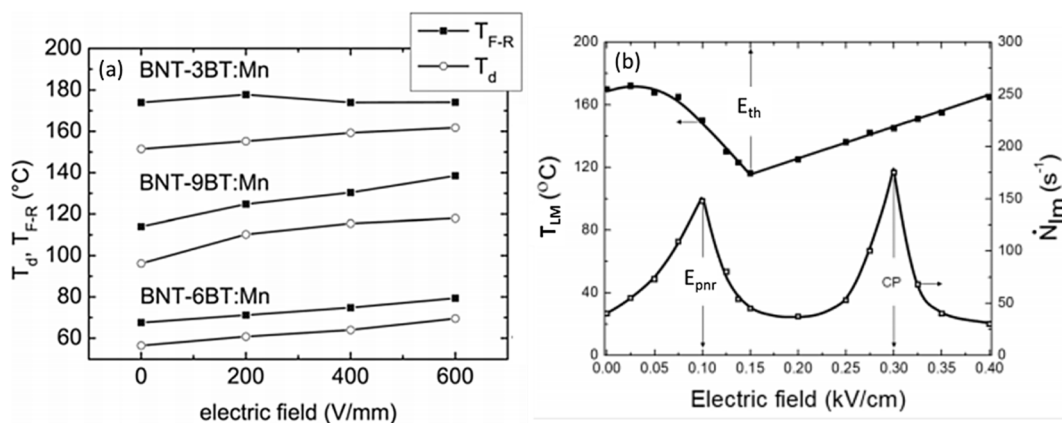


**Fig. 20.** Dependence of characteristic temperatures on electric field bias: (a)  $T_d$  and  $T_{F-R}$  in  $(1-x)\text{Bi}_{0.5}\text{Na}_{0.5}(\text{Ti}_{0.995}\text{Mn}_{0.005})\text{O}_3-x\text{Ba}(\text{Ti}_{0.995}\text{Mn}_{0.005})\text{O}_3$  [Reproduced from Ref. [227] <https://aip.scitation.org/doi/10.1063/1.3674275> with the permission of AIP Publishing]; and (b)  $T_{LM}$  and acoustic emission count rate in 0.94BNT-0.06BT [Reproduced from Ref. [228] <https://aip.scitation.org/doi/10.1063/1.5009326> with the permission of AIP Publishing].

#### 4.4. Creation and destruction of morphotropic phase boundaries

*In-situ* TEM microscopy has provided important insights into the evolution of the structure and domain configuration in BNT-based ceramics with co-existing polymorphs. Key experiments were performed by Ma et al. on  $(100-x)\text{BNT}-x\text{BT}$  initially unpoled ceramics, with  $x = 5.5, 6, \text{ and } 7$  [230]. Local electron diffraction patterns indicated that in absence of any applied electric field, the composition  $x = 5.5$  exhibited the coexistence of  $R3c$  and  $P4bm$  phases in most grains. The composition  $x = 6$  had a mixture of  $R3c + P4bm$  phases in about 40% of the grains, with the remaining grains showing the  $P4bm$  phase; meanwhile,  $x = 7$  had a pure tetragonal  $P4bm$  phase (Fig. 21). During electrical loading, it was observed that the fraction of  $P4bm$  phase in  $x = 5.5$  irreversibly transformed to the  $R3c$  phase, suggesting a suppression of the  $R3c/P4bm$  morphotropic phase boundary configuration initially present (Fig. 21a, e). As a result of the transformation, the  $d_{33}$  coefficient increases until a plateau value of about 120 pC/N (Fig. 21a). In the composition  $x = 6$ , the phase evolution during electrical loading in grains with  $P4bm$  phase followed a different transformation pathway [230]. At 32 kV/cm, the  $P4bm$  phase disappeared and the coexistence of domains with  $R3c$  and  $P4mm$  symmetries was observed (creation of the  $R3c-P4mm$  MPB from the initial  $P4bm$  phase). With increasing field, the  $P4mm$  phase transformed to the  $R3c$  phase at about 40 kV/cm, destroying the metastable  $P4mm/R3c$  MPB configuration (Fig. 21b, e). The  $d_{33}$  evolution displayed in Fig. 21b shows an initial increase due to the formation of the  $R3c/P4mm$  MPB, and a subsequent decrease when the  $R3c/P4mm$  MPB is wiped away at higher electric fields [230]. In

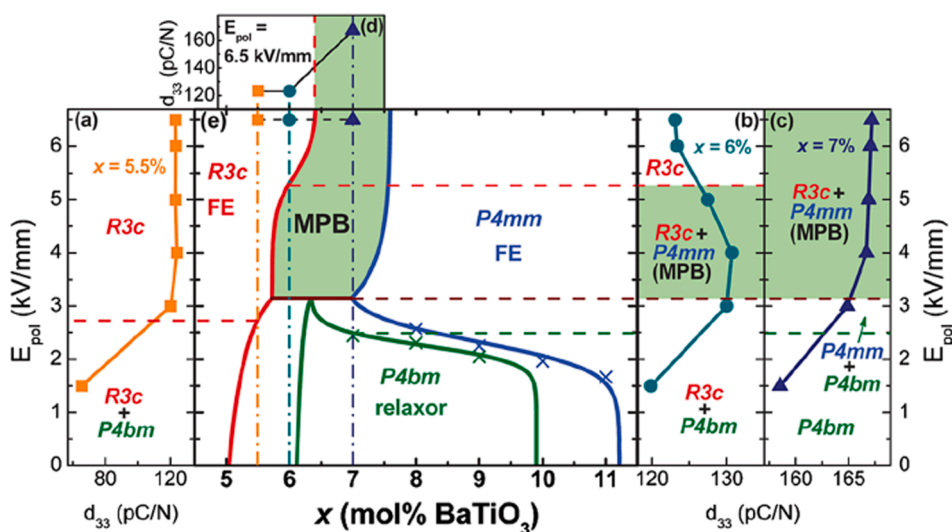


**Fig. 21.** Effect of the electric field on structure and piezoelectric coefficient for different  $(1-x)\text{BNT}-x\text{BT}$  compositions across the morphotropic phase boundary range. Green areas indicate the presence of  $R3c + P4mm$  MPB. Evolution of  $d_{33}$  as a function of the poling field for  $x = 0.055$  (a),  $x = 0.06$  (b) and  $x = 0.07$  (c); (d): evolution of  $d_{33}$  as a function of composition in the range  $0.055 \leq x \leq 0.07$  after poling at 6.5 kV/mm; and (e) variation of the crystal structure as a function of the poling field for different values of  $x$ . [Reproduced with permission from Ref. [230] <https://journals.aps.org/prl/abstract/10.1103/PhysRevLett.109.107602> Copyright 2012 American Physical Society].

the composition  $x = 7$ , which initially shows only the  $P4bm$  phase, the application of the electric field produced a transition of  $P4bm$  nanodomains into  $P4mm$  lamellar domains at about 25 kV/cm, and subsequently, a partial transformation of the  $P4mm$  phase into the  $R3c$  phase (Fig. 21c, e). The newly-created  $P4mm/R3c$  MPB was stable up to  $E > 40$  kV/cm and exhibited the largest  $d_{33}$  values, until the maximum *ex-situ* poling field of 65 kV/cm (Fig. 21d). It was suggested that the transition from  $P4bm$  to  $R3c$  or  $P4mm$  is directly driven by the applied electric field and it closely resembles an antiferroelectric-to-ferroelectric transformation. Meanwhile, the  $P4mm$  to  $R3c$  ferroelectric-to-ferroelectric transition is facilitated by the piezoelectric strain developed during electrical loading [230].

#### 4.5. Ferroelectric-to-relaxor-like reverse transformations

This type of transformation occurs in a large number of BNT-based materials in which the ferroelectric phase induced during the first electrical cycle is metastable, and the application of a reverse electric field causes the return to the initial relaxor-like phase, as discussed above in Section 4.1. Insightful experiments on the microscopic mechanisms of these peculiar electric field-driven transitions were performed on  $[(\text{Bi}_{0.5}\text{Na}_{0.5})_{0.95}\text{Ba}_{0.05}]_{0.98}\text{La}_{0.02}\text{TiO}_3$ , whose polarization-strain-electric field loops (Fig. 22a) were intimately linked to the evolution of the domain structure obtained by *in-situ* TEM at room temperature (Fig. 22b–o) [37]. Virgin samples exhibited a mixed  $R3c + P4bm$  phase with the presence of nanodomains (see state  $Z_0$  in Fig. 22b, c). The application of an electric field produced an initial increase of polarization and the appearance of lamellar domains, without a significant increase in strain (stage  $Z_1$  in Fig. 22a). The increase of the electric field until 45 kV/cm determined a remarkable increase of both polarization and strain, with the formation of larger lamellar domains and the stabilization of a single  $R3c$  phase, indicated as stage  $Z_2$  in Fig. 22a, with the relative domain structure and diffraction pattern shown in Fig. 22d and e, respectively [37]. A large remnant polarization and remnant strain can be observed in the hysteresis loops, along with the presence of ferroelectric domains in the TEM image (see stage  $Z_3$  in Fig. 22a and f). By reversing the field, the ferroelectric domains start to break apart and miniaturize, leading to the reappearance of the  $P4bm$  phase, along with a reduction of polarization and strain (stages  $Z_4$  and  $Z_5$  in Fig. 22a, g–j). A further increase of the electric field along the negative direction increasingly drives the  $P4bm$ -to- $R3c$  transition. The formation of lamellar ferroelectric domains, whose size increases with increasing the applied field, with a consequent increase of polarization and strain, can be observed from stage  $Z_6$  to  $Z_8$  (Fig. 22a, k, l), where the prevalence of the  $R3c$  phase is re-established (Fig. 22m) [37]. The microscopic transformations here described are related to the characteristic sequence of current peaks at  $E_1$  and  $E_2$  observed in the current-electric field loops previously described relatively to Fig. 12c. Figs. 22n and 22o show the ferroelectric-type domain structure and the  $R3c$  diffraction pattern of the sample poled under 60 kV/cm for 20 min at room temperature.

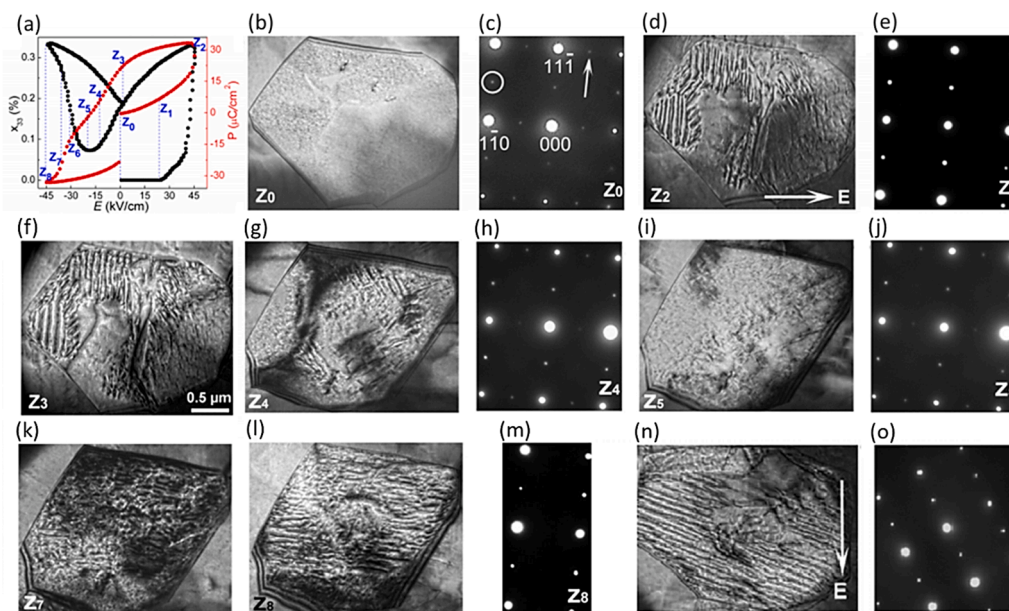


**Fig. 22.** Correlation between the ferroelectric hysteresis and microstructural evolution in  $[(\text{Bi}_{0.5}\text{Na}_{0.5})_{0.95}\text{Ba}_{0.05}]_{0.98}\text{La}_{0.02}\text{TiO}_3$ : (a) polarization- and strain-electric field hysteresis loops; (b)–(m) domain structure and electron diffraction patterns at the different points  $Z_i$  along the hysteresis loop; (n), (o) domain structure and electron diffraction pattern after poling. [Reproduced with permission from Ref. [37] <https://journals.aps.org/prb/abstract/10.1103/PhysRevB.93.174114> Copyright 2012 American Physical Society].

#### 4.6. Metastable electric field-induced domain structures

The phenomenon of metastable electric field-induced domain structure was documented by *in-situ* TEM experiments carried out on  $0.91(\text{Bi}_{0.5}\text{Na}_{0.5})\text{TiO}_3-0.06\text{BaTiO}_3-0.03(\text{K}_{0.5}\text{Na}_{0.5})\text{NbO}_3$  ( $0.91\text{BNT}-0.06\text{BT}-0.03\text{KNN}$ ) at room temperature, where the ceramics exhibit an ergodic relaxor behaviour [173]. It was observed that in absence of an applied electric field, the structure is a mixture of  $P4bm$  and  $R3c$  phases (with  $P4bm$  being predominant), with no clear presence of domains (Fig. 23a). The application of an electric field (with an actual magnitude reported as approximately 50 kV/cm) along the  $[0\ 0\ 1]$  direction induced the appearance of a rhombohedral distortion and ferroelectric lamellar domains in the TEM images along the  $[110]$  zone axis (Fig. 23b, c) [173]. During field removal, the ferroelectric domains disappeared and so did the rhombohedral distortion (Fig. 23d). The contrast in the TEM image was attributed to the strain induced by the bending of the thin sample and to the presence of dislocations (Fig. 23d) [173]. These observations suggest a reversible ergodic relaxor-to-ferroelectric transformation, which well-correlates to the hysteresis loops previously described in Fig. 12c and the presence of the current peaks at  $E_F$  and  $E_R$ .

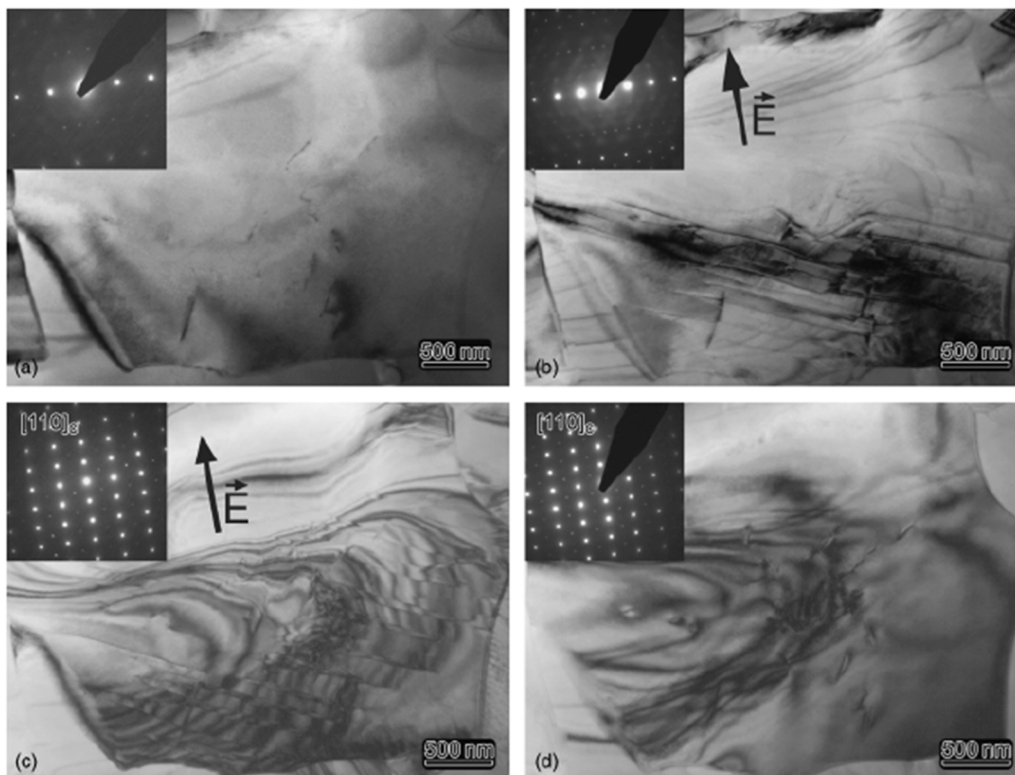


**Fig. 23.** Evolution of microstructure and electron diffraction patterns in a grain of  $0.91\text{BNT}-0.06\text{BT}-0.03\text{KNN}$  during the application of an electric field: (a) before applying the electric field no domains are present; (b), (c) at a nominal field of 25 kV/cm (actual field of about 50 kV/cm) lamellar domains are present; (d) after removing the electric field. [Reproduced with permission from Ref. [173] Copyright 2011 John Wiley and Sons].

#### 4.7. Large piezoelectricity by poling below the coercive field

In BNT-based materials, large piezoelectricity can also be obtained at electric fields much lower than the coercive field of the field-induced ferroelectric phase, as observed for the case of  $(1-x)\text{BNT}-x\text{BT}$  compositions with  $0.06 \leq x \leq 0.09$ , which present a  $P4bm$  structure in the virgin state [231]. The data in Fig. 24 are relative to  $0.93\text{BNT}-0.07\text{BT}$ . In particular, Fig. 24a shows the evolution of volumetric strain and polarization during the very first electric cycle, from which the critical field inducing the  $P4bm$ -to- $P4mm$  transformation can be identified ( $E_{cr} = 25$  kV/cm). Fig. 24b shows the loading-unloading branch of the P-E loops, which identifies the coercive field ( $E_c = 24$  kV/cm). In Fig. 24c, it can be observed that by poling at a DC electric field  $E_p = 14$  kV/cm (lower than  $E_{cr}$  and  $E_c$ ), a high piezoelectric coefficient can be obtained with a similar value to those achieved under higher poling fields. It should be underlined that for  $(1-x)\text{BNT}-x\text{BT}$  systems, this peculiar behaviour was observed only in compositions with  $P4bm$  phase, but not in those with  $R3c$  and  $P4mm$  structures [231]. The origin of this unexpected poling behaviour lies in the electric field-induced processes occurring in the  $P4bm$  phase. *In-situ* TEM experiments (Fig. 24d–f) revealed that during the very first poling cycle, the nanodomains in the  $P4bm$  phase (Fig. 24d) irreversibly coalesce into a tweed structure at the nominal field of 14 kV/cm (Fig. 24e) and subsequently grow into thin lamellar domains at 28 kV/cm nominal field (Fig. 24f), before the  $P4bm$ -to- $P4mm$  phase transition takes place above 30 kV/cm. The high piezoelectric coefficient obtained by poling at  $E_p = 14$  kV/cm can be therefore attributed to the alignment of the polarization within the coalesced nanodomains [231].

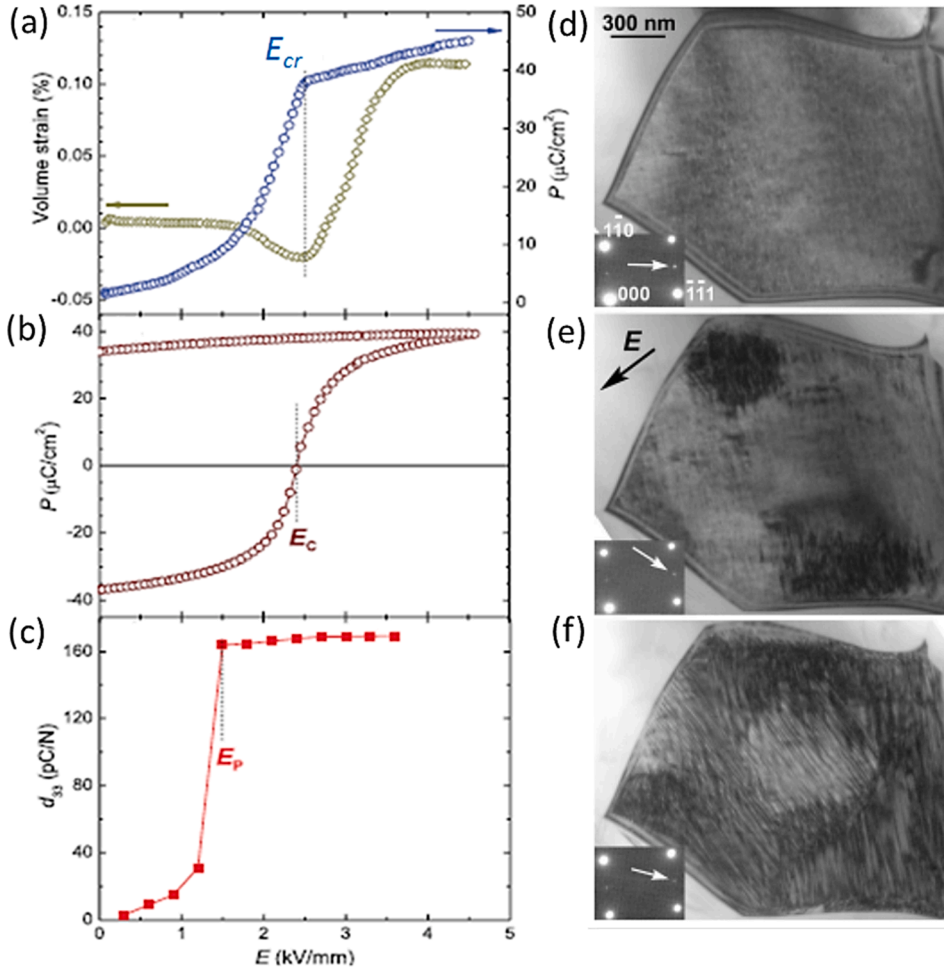


**Fig. 24.** (a) Dependence of volumetric strain and polarization on the electric field on virgin samples; (b) polarization–electric field hysteresis loop; (c) dependence of  $d_{33}$  on poling field; (d)–(f) TEM images of a representative grain along the [112] zone-axis under an applied field of 0 kV/mm (d), 1.4 kV/mm (e) and 2.8 kV/mm (f). All plots and images refer to 0.93BNT-0.07BT ceramics. [Reproduced from Ref. [231] <https://aip.scitation.org/doi/10.1063/1.4794866> with the permission of AIP Publishing].

#### 4.8. Deviations from Rayleigh-type behaviour

In ferroelectric/ferroelastic materials, Rayleigh-type behaviour is observed well below the coercive field, during the application of cyclic electric field waveforms with small amplitudes. Rayleigh-type behaviour in ferroelectrics is distinguished by hysteretic P-E loops, characterized by a parabolic dependence of the polarization on the electric field, and by a linear dependence of the dielectric permittivity on the electric field amplitude. These dependencies are described by the well-known Rayleigh law, which can be expressed by the following relationships [232,233]:

$$P = (\epsilon_e + \gamma \Delta E)E \pm \frac{\gamma}{2}(\Delta E^2 - E^2) \quad (2)$$

$$\epsilon = \epsilon_e + \gamma \Delta E \quad (3)$$

where  $\Delta E$  is the amplitude of the low electric field cycle,  $\epsilon_e$  is the permittivity extrapolated at zero electric field amplitude ( $\Delta E = 0$ ),  $\gamma$  is the rate of increment of permittivity with increasing electric field amplitude  $\Delta E$ , and  $E$  is the value of the applied field during the AC cycle. Both the Rayleigh parameters  $\epsilon_e$  and  $\gamma$  exhibit a logarithmic decrease with increasing the frequency of the AC weak field due to the decrease of the extrinsic contribution of domain wall movement with increasing frequency [233].

It has been widely accepted that in ferroelectric/ferroelastic materials, the Rayleigh-like behaviour originates from domain wall motion in presence of randomly distributed pinning centres with spatially varying strength that create local potential energy barriers. Depending on the amplitude and frequency of the weak applied field, domain walls are either reversibly displaced around equilibrium

positions within potential energy wells, or they overcome the local energy barriers and irreversibly move into another equilibrium position, giving rise to the observed Rayleigh-like dependencies [232,233]. The Rayleigh relationships have been also applied to various relaxor-ferroelectric systems [234–236], but deviations from the Rayleigh-type behaviour in relaxor-type materials have been also reported in the literature [237–239], making the general validity of the Rayleigh law in relaxor-like systems rather questionable. Regarding BNT-based materials, several compositions have shown a Rayleigh-type behaviour in their non-ergodic relaxor/ferroelectric phases, as demonstrated in various studies [240–243].

Nonetheless, substantial deviations from the Rayleigh-type behaviour may likely take place when approaching the ergodic phase during heating, as reported for the case of  $0.95[0.94(\text{Bi}_{0.5}\text{Na}_{0.45}\text{Li}_{0.05})\text{TiO}_3-0.06\text{BaTiO}_3]-0.05\text{CaTiO}_3$  (BNLT5) [238]. Fig. 25 shows the temperature dependence of the P-E loops in the low-field regime under 5 kV/cm (Fig. 25a) and 17.5 kV/cm (Fig. 25b) electric field amplitude and 5 Hz frequency. In particular, at  $T = 150^\circ\text{C}$ , the current-electric field loops of BNLT5 at 17.5 kV/cm amplitude are characterized by the presence of four visible current peaks at high fields  $\pm E_F$  and  $\pm E_R$  (as typically observed in ergodic relaxors), and by four additional current humps in the lower field regime, indicated with  $\pm E_{SRF}$  and  $\pm E_{SRR}$  in Fig. 25b (the subscript “SR” stands for short range), which appear from the very first loading cycle showing a negligible frequency dependence in the range 1 Hz–10 Hz [238]. The sequence of current humps/peaks in BNLT5 can be interpreted according to the mechanisms of electric field-induced transitions suggested by Jo et al. on the basis of *in-situ* diffraction studies carried out on  $0.94\text{Bi}_{0.5}\text{Na}_{0.5}\text{TiO}_3-0.06\text{BaTiO}_3$  [191]. It was proposed that EFITs take place via two key steps: (i) the collective rotation/alignment of polar nanoregions along the electric field direction (step (i)); and (ii) the expansion/growth of aligned polar nanoregions upon further electrical loading (step (ii)). Therefore, in BNLT5, the current humps in the low field range can be related to step I: during electrical loading, polar nanoregions are forced to rotate and align along the direction of the applied field (current humps at  $\pm E_{SRF}$ ), while upon field removal, most PNRs return to their original orientation (current humps at  $\pm E_{SRR}$ ). The current peaks in the high-field regime can be instead related to step II: during loading across

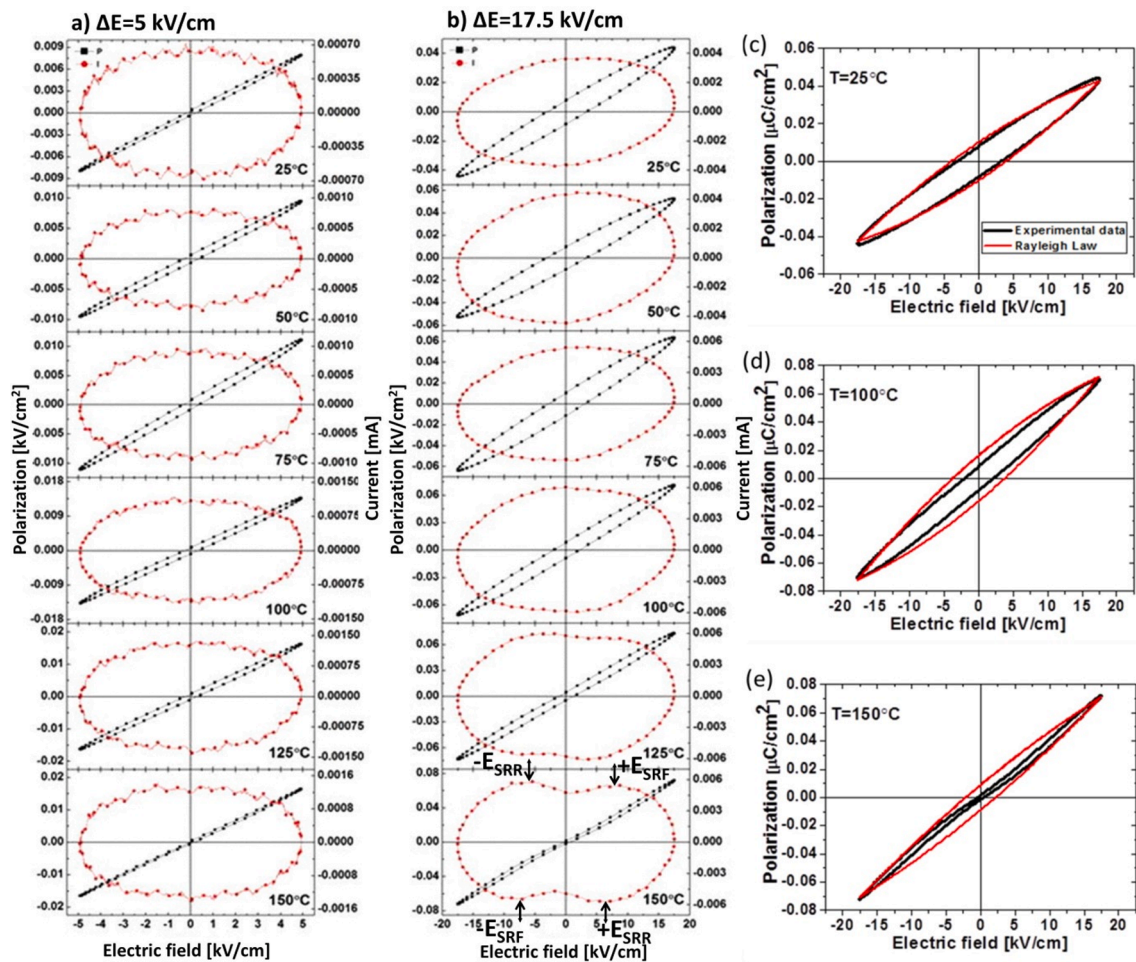


Fig. 25. Rayleigh-like loops of  $0.95[0.94(\text{Bi}_{0.5}\text{Na}_{0.45}\text{Li}_{0.05})\text{TiO}_3-0.06\text{BaTiO}_3]-0.05\text{CaTiO}_3$  ceramics in the temperature range  $25\text{--}150^\circ\text{C}$  at 5 Hz frequency: (a) current-polarization–electric field loops at 5 kV/cm electric field amplitude; and (b) current-polarization–electric field loops at 17.5 kV/cm electric field amplitude [Reproduced from Ref. [238] <https://aip.scitation.org/doi/abs/10.1063/1.4895559?ver=pdfcov&journalCode=apl> with the permission of AIP Publishing]. Fitting of the polarization–electric field loops at 17.5 kV/cm electric field amplitude and 5 Hz using the Rayleigh law at  $25^\circ\text{C}$  (c),  $100^\circ\text{C}$  (d) and  $150^\circ\text{C}$  (e).

$\pm E_F$ , the aligned PNRs grow in size and form a metastable long-range polar order, which disappears during unloading in correspondence of the current peaks at  $\pm E_R$ . The presence of the four current humps in BNLT5 is responsible for the deviation from the Rayleigh-type behaviour, evidenced by a departure from the parabolic dependence of the polarization on the electric field (Fig. 25c–e), with P-E loops characterized by a sigmoidal-type shape, with low hysteresis and nearly-zero remnant polarization (Fig. 25b at  $T = 150^\circ\text{C}$ ). The presence of humps and sharp peaks in the I-E loop has been reported also for the systems  $\text{Bi}_{0.48}(\text{Na}_x\text{K}_{1-x})_{0.48}\text{Sr}_{0.04}[(\text{Ti}_{0.977}\text{Nb}_{0.023})\text{O}_3]$  (with  $x = 0.80\text{--}0.88$ ), and similar interpretations have been given, involving the alignment of PNRs and structure transitions, respectively. For further details, the reader can consult Ref. [178].

The deviation from the classical Rayleigh-type dynamics suggests that the potential energy landscape in the ergodic relaxor state cannot be modelled as a multi-well profile with several energy minima associated with the random distribution of pinning sites of different strength, used for the derivation of the Rayleigh laws in the ferroelectric state. Instead, the potential energy profile could be described by a U-shape function with one potential energy minimum, identified by a unique stable state of nearly zero remnant polarization, in which the system would return once the external field is removed. This type of potential was applied for the case of hard ferroelectrics as discussed in Ref. [232]. The U-shape energy potential implies reversibility, which is in line with the negligible frequency dispersion of the current humps and the P-E loops. However, the underlying process responsible for the deviation from the Rayleigh-like behaviour in BNLT5 is not entirely reversible, as proved by the presence of a  $d_{33} = 1.1$  pC/N, after a cyclic field of 17.5 kV/cm and 5 Hz frequency was applied at  $150^\circ\text{C}$  on a virgin sample and by the small hysteresis displayed in the P-E loops [238]. Evidence of irreversibility of the phase transition in the ergodic phase have been also recently reported, as evidenced by the DC field-induced increase of dielectric permittivity at THz frequencies. The transition is not detected by conventional diffraction methods [244].

#### 4.9. Cascade phenomena under DC electric fields

It is well-known that ferroelectric/ferroelastic materials exhibit a time-dependent variation of polarization and strain during the application of a constant electric field. This phenomenon, commonly referred to as “creep” in the literature, has been observed in various materials, which have shown similar polarization and strain time dependences, characterized by a continuous increase over time, at a gradually decreasing rate [245–248]. The time-dependent behaviour of BNT-based materials presents specific peculiarities, as proved by a recent study conducted on 0.93BNT-0.07BT, whose P-E and S-E loops are shown in Fig. 26a and b [249]. The relevant experiments were based on electrical creep tests carried out by ramping up the electric field at different levels in the range 8–20 kV/cm and holding it for 1200 s, while simultaneously monitoring polarization and strain during the dwell time. For electric fields in the range 8–10 kV/cm and 17–20 kV/cm, the functional time dependencies of polarization (Fig. 26c) and strain (Fig. 26d) are similar to those observed in conventional ferroelastic/ferroelectric materials. Meanwhile, when the electric field was held in the range 11–16 kV/cm,

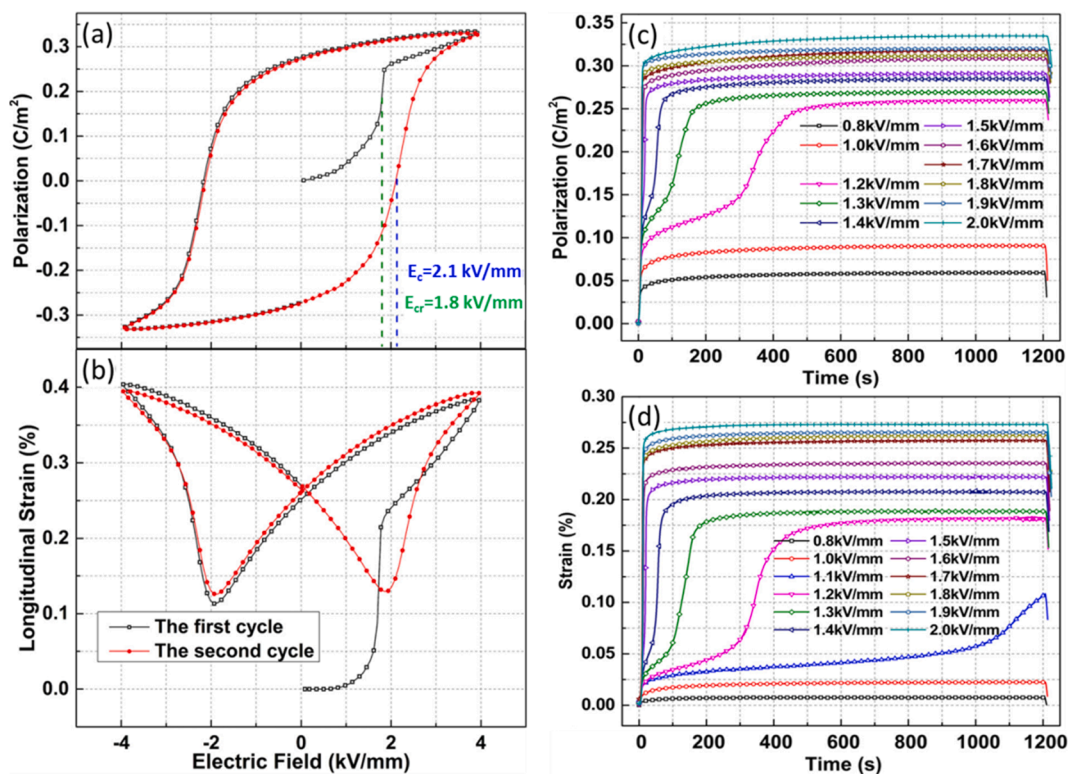


Fig. 26. Hysteresis loops and creep curves of 0.93BNT-0.07BT: (a) polarization–electric field loop; (b) strain–electric field loop; (c) polarization creep curves; and (d) strain creep curves. [Reproduced from Ref. [249] <https://aip.scitation.org/doi/10.1063/1.4978704> with the permission of AIP Publishing].

polarization and strain showed a different time evolution, characterized by three main stages. In the first stage (incubation stage), both quantities increase over time at a decreasing rate. In the second stage, polarization and strain show a rapid increase with an increasing rate over time (cascade stage). The third stage is characterized by an increase of polarization and strain during time with a decreasing rate until saturation (saturation stage) [249]. It can be noticed that the duration of the incubation stage and the cascade stage generally decreases with increasing the applied field. Similar creep behaviour, with the presence of cascade effects, was also found in non-ergodic, lead-based relaxors [250]. This time-dependent behaviour can be rationalized on the basis of an electric field-induced transition from a non-ergodic relaxor to a ferroelectric state. At low electric fields, only a limited creep process is observed because the phase transition is not yet triggered. At high fields, the creep response is also limited, since most of the transformation is driven during the loading ramp before dwelling. At intermediate fields, larger creep with cascade effects is observed because the non-ergodic relaxor-to-ferroelectric transition takes place during field dwelling. The absence of cascade-like features in the creep curves of poled specimens confirms that the described transition is irreversible.

#### 4.10. Heterogeneous electric field-induced transitions

##### 4.10.1. Effect of grain orientation

Studies carried out on 0.82BNT-0.18BKT ceramics via three-dimensional (3D)-XRD technique, which allows focusing on the response of individual grains, have demonstrated that the pathways of electric field induced-transitions in polycrystalline systems are influenced by the relative orientation of grains with respect to the applied field [251]. In the virgin state, 0.82BNT-0.18BKT possesses a pseudo-cubic structure on average, while after poling, the majority of grains transformed to a rhombohedral phase with the presence of domain texture. This was especially observed in grains having the  $[111]$  direction (polar direction in the rhombohedral structure) parallel to the applied field. Meanwhile, most grains with  $[001]$  direction oriented within  $7^\circ$  from the electric field direction either did not show any field-induced transformation or transformed to a tetragonal phase (Fig. 27) [251]. However, these differences are not only due to the different grain orientation with respect to the applied field, but also to other effects, including: (i) the variation of local stresses in neighbouring grains, caused by the highly anisotropic dielectric and piezoelectric response, and (ii) the complicated domain configuration nearby the grain boundaries arising from the minimization of the electrostatic and elastic energy at the grain boundaries. The importance of grain orientation on electric field-induced transitions has been also reported for rare earth-modified BiFeO<sub>3</sub> ceramics [252].

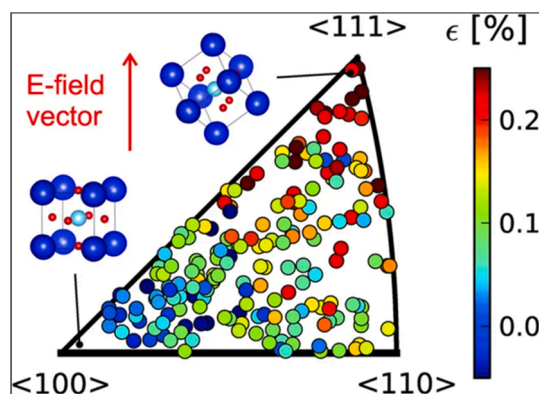
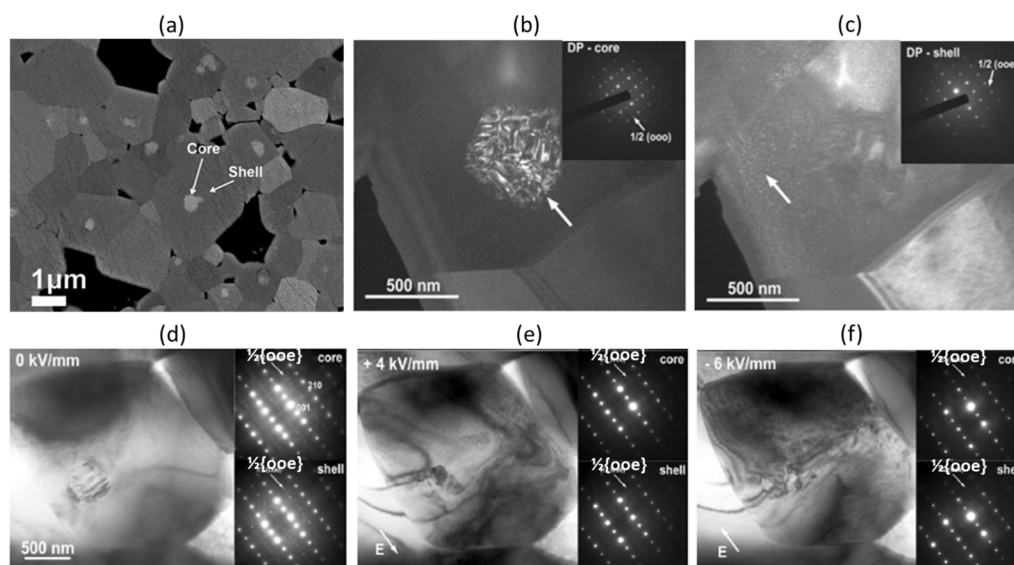


Fig. 27. Strain map in grains of 0.82BNT-0.18BKT ceramics with different orientations with respect to the applied field. Each circle represents a single grain; the position of the circle is determined by the orientation of the crystallographic directions in the pseudo-cubic unit cell with respect to the applied field. [Reproduced with permission from Ref. [251]].

##### 4.10.2. The case of core-shell microstructures

Heterogeneous EFITs have been also observed in 0.75BNT-0.25ST [253]. The microstructure with grain size of about  $2\ \mu\text{m}$  displayed core-shell features, with the core size varying in the range 180–360 nm (Fig. 28a–c) [253]. The core, depleted of Sr, displayed a prevalence of rhombohedral  $R3c$  phase in the local diffraction patterns, along with the presence of irregular patterns of domains, which smear out towards the outer part of the core, leading to semicoherent core-shell interfaces with no presence of dislocations (Fig. 28b). The shell, rich in Sr, exhibited mixed rhombohedral  $R3c$  and tetragonal  $P4bm$  phases with domains of much smaller size than those in the core (Fig. 28c) [253]. Fig. 28d–f show the field-induced evolution of the core-shell microstructure of 0.75BNT-0.25ST. It can be noticed that core and shell present different responses. The application of an electric field of 40 kV/cm on the virgin state along the  $[001]$  direction produced the reorientation of domains within the core (Fig. 28e); this is also observed during the reversal of the field at  $-60\ \text{kV/cm}$ , where domain walls appear parallel to the direction of the electric field (Fig. 28f) [253]. However, the core does not grow in size during electrical loading, but undergoes an irreversible transformation from a non-ergodic relaxor to a ferroelectric state. On the other hand, the shell presents a change in contrast during electrical loading, which disappeared during field removal, suggesting a reversible transformation from an ergodic relaxor to a ferroelectric state [253].

Fig. 29 depicts the temperature dependence of the electric field-induced transformations in the core-shell microstructure. At  $25^\circ\text{C}$



**Fig. 28.** Microstructure of 0.75BNT-0.25ST ceramics. (a) SEM image of the core–shell structure in backscattering mode; (b)–(d) TEM images and local diffraction patterns of core and shell regions along the  $[1\ 1\ 2]_{pc}$  zone axis (b, c) and  $[1\ 2\ 0]_{pc}$  zone axis (d) under no applied field; (e), (f) TEM images and local diffraction patterns of core and shell regions under 40 kV/cm and  $-60$  kV/cm, applied along the  $[0\ 0\ 1]$  direction. Superlattice reflections of the type  $\frac{1}{2}\{000\}$  and  $\frac{1}{2}\{00e\}$  are found in both core and shell. [Reproduced with permission from Ref. [253] Copyright 2015 John Wiley and Sons].

and 0 kV/cm, the core contains a prevalence of domains with strong contrast shown in black colour, while the shell presents smaller sized domains schemed as red dots (Fig. 29a) [253]. A temperature increase determines an overall miniaturization of domains in both core and shell parts. At 70 °C, a remarkable change in domain contrast can be observed in the core, with domains shrinking in size (Fig. 29b). A further temperature increase determines further miniaturization of domains (Fig. 29c, d) until 345 °C, where the domain contrast almost disappears in the core, whereas domains appear highly dispersed in the shell (Fig. 29e) [253]. The application of an electric field of 40 kV/cm at 25 °C (Fig. 29f) produces the alignment of domains along the field direction in the core and the appearance of aligned ferroelectric domains in the shell, indicating a heterogeneous electric field-induced transition in core and shell. Electrical loading at 70 °C still induces irreversible transformations in the domain structure in both core and shell, although to a smaller extent, since the field transition threshold increases with temperature (Fig. 29g). The effects of the field application diminish with a further temperature increase due to the stabilization of an ergodic relaxor state (Fig. 29h–j) [253].

Piezoresponse force microscopy (PFM) has provided further insights into the EFITs in the core–shell microstructure of 0.75BNT-0.25ST [254]. The application of +10 V voltage led to the formation of a domain with size of about  $4\ \mu\text{m}^2$  (dark area in Fig. 30a, b), and additional in-plane oriented domains visible in the lateral PFM images (Fig. 30c, d). The size of the domain induced during poling shrunk over time to the size of about  $400\ \text{nm}^2$  (the size of the non-ergodic relaxor core) 45 min after the application of the poling voltage (Fig. 30e, f), due to the relaxation of the ergodic relaxor shell region. On the other hand, the size of the in-plane oriented

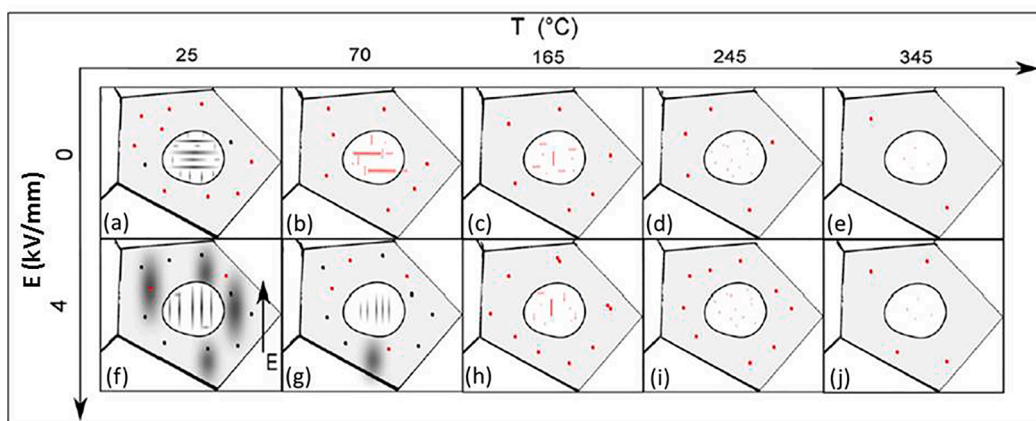


**Fig. 29.** Scheme of temperature and electric field effects on the evolution of the core–shell structure. [Reproduced with permission from Ref. [253] Copyright 2015 John Wiley and Sons].

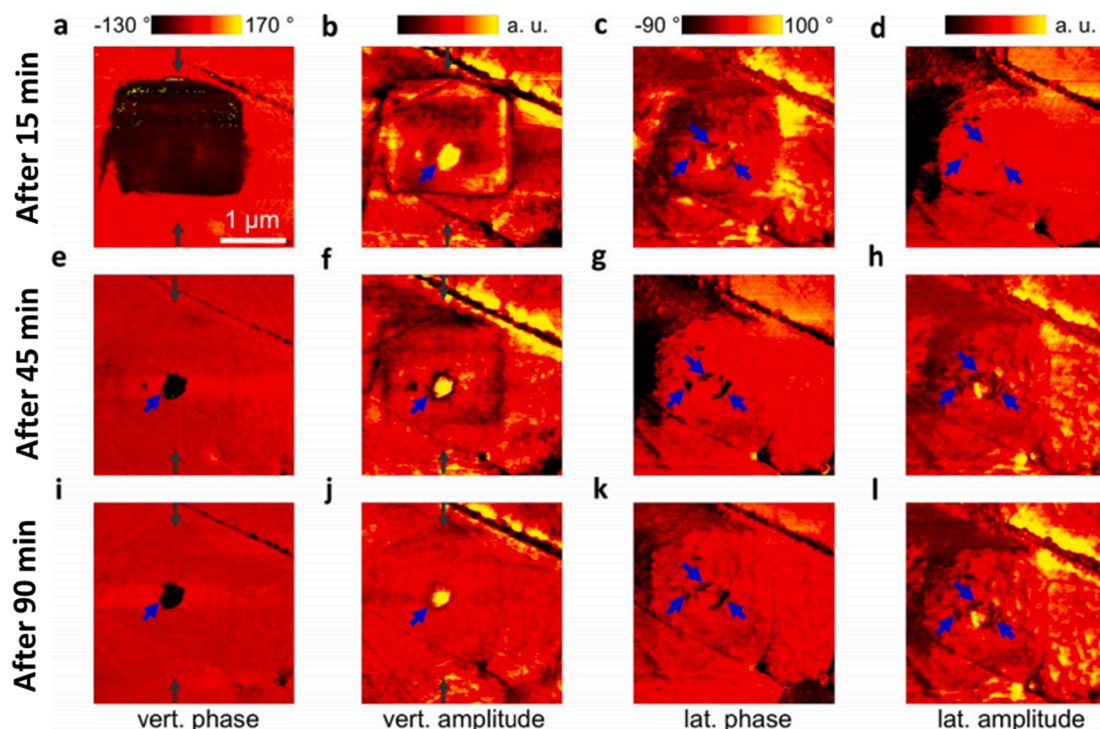


Fig. 30. Phase and amplitude images obtained by vertical and lateral piezoresponse force microscopy taken at 15 min (a–d), 45 min (e–h) and 90 min (i–l) after local poling. The blue arrows indicate the core regions. The grey arrows mark the lines along which the cross-sectional profiles showed a variable height of the core regions during time (profiles not shown here). [Reproduced with permission from Ref. [254]].

domains increased (Fig. 30g, h) [254]. The core–shell interface area displayed a stable presence of domains in the vertical and lateral PFM images 90 min after the application of the poling voltage (Fig. 30i–l). The nucleation and growth of the lateral domains with in-plane polarization were attributed to the mismatch of stress and polarization at the core–shell interface as a compensation effect [254]. During the application of an electric field, the lateral domains nucleated during poling and switched from a direction perpendicular to the direction parallel to the applied field, reducing the energy barrier for the ergodic relaxor-to-ferroelectric phase transition taking place in the shell [254].

Core-shell microstructures have been also observed in other BNT-based materials, including 0.94BNT-0.06BT, 0.89BNT-0.11BT [186],  $0.94(\text{Bi}_{0.5}\text{Na}_{0.5})\text{TiO}_3\text{-}0.06\text{Ba}(\text{Zr}_x\text{Ti}_{1-x})\text{O}_3$  ( $x = 0.1, 0.15$ ) [255] and  $(1-x)[0.94(\text{Bi}_{0.5}\text{Na}_{0.5})\text{TiO}_3\text{-}0.06\text{BaTiO}_3\text{-}x\text{LiNbO}_3$  ( $x = 0.015, 0.025$ ) [256], which are expected to share similar core–shell evolution under an applied electric field.

#### 4.11. Rotostriction, rotopolarization and polarization twist

The system 0.75BNT-0.25ST is an example of materials in which ferrodistorptive and antiferrodistorptive instabilities can mutually cooperate to enhance electric field-induced strain [257]. Ferrodistorptive instabilities are related to the softening of a polar phonon mode at the centre of the Brillouin zone that leads to the formation of spontaneous polarization and spontaneous strain, as coupled order parameters. Antiferrodistorptive instabilities produce the condensation of a non-polar mode at the Brillouin zone-boundary. This produces the tilting of the oxygen octahedra and consequently causes strain through the effect known as “*rotostriction*” [258,259].

To further elucidate the mechanisms of electric field-induced transition and the contribution of rotostriction, *in-situ* neutron diffraction experiments, in which the scattering vector ( $k$ ) was parallel or perpendicular to the applied field direction, were carried out on 0.75BNT-0.25ST ceramics (Fig. 31a, b) [257]. The comparison of diffraction patterns of the virgin (not reported here) and remnant state after electric field removal (reported in Fig. 31a) suggested that the electric field-induced transition is almost entirely reversible. The analysis of the diffraction patterns after applying an electric field of 30 kV/cm (remnant state in Fig. 31a) indicated a pseudo-cubic structure characterized by the presence of  $h00$  and  $hhh$  reflections (Fig. 31a, c), which do not shift position in grains with different orientations with respect to the applied field direction [257]. Under the application of an electric field of 30 kV/cm, the positions of the reflections vary with grain orientation including that of the  $\frac{1}{2}$  311 superstructure reflection (Fig. 31b), which is not clearly visible in absence of the applied field (Fig. 31a). The field-induced structure was identified with the rhombohedral  $R3c$  phase ( $\bar{a}\bar{a}\bar{a}$  tilting and polarization along the [111] direction), and the tetragonal  $P4mm$ . However, the additional presence of the  $P4bm$  tetragonal phase was not ruled out. Grains in which the scattering vector was parallel to the applied field ( $k//E$ ) mainly transformed to the  $P4mm$  phase, with the development of polarization and strain along the same direction in a coupled fashion [257]. The electric field-induced strain in these grains was attributed to the piezoelectric effect and electrostriction, as shown in Fig. 31d. In grains for which the condition  $k\perp E$

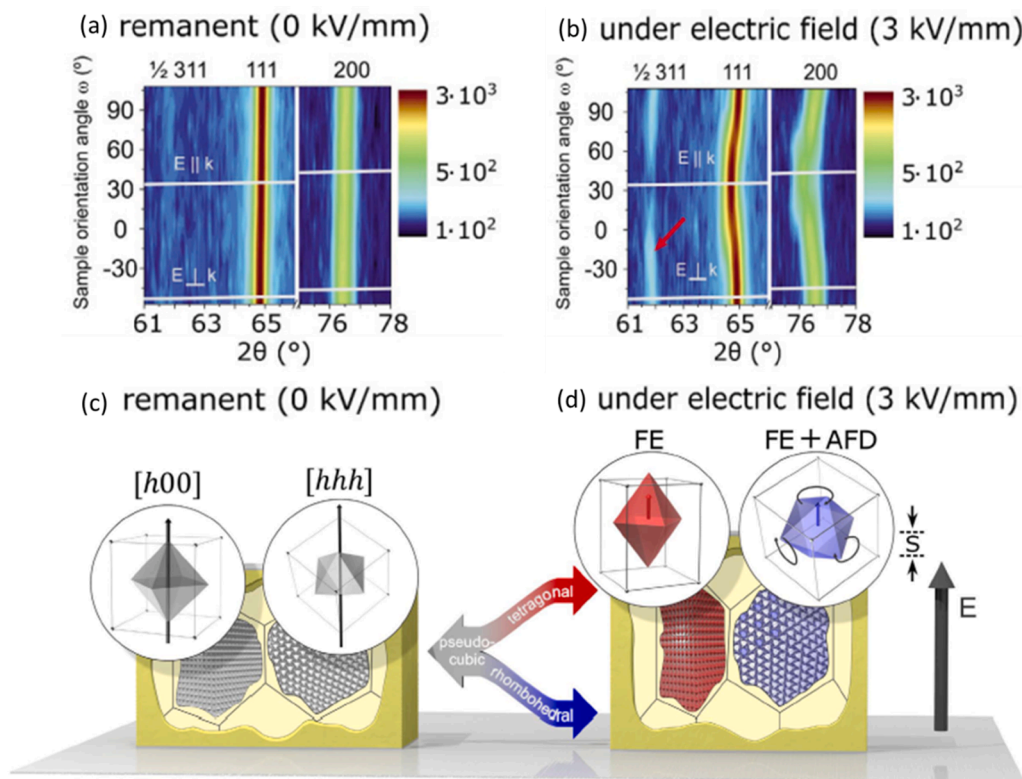


**Fig. 31.** (a)–(b) Diffraction patterns at different sample's orientation angles in the range  $-57^\circ \leq \omega \leq 108^\circ$  of remanent state at 0 kV/mm after applying an electric field of 30 kV/cm (a) and under an applied electric field of 30 kV/cm (b). The  $2\theta$  ranges selected include  $\frac{1}{2}$  311, 111 and 200 reflections. The white lines trace the patterns obtained in the conditions of  $k \parallel E$  and  $k \perp E$ . The red arrow in figure (b) indicates the maximum intensity of the  $\frac{1}{2}$  311 reflection. (c) Scheme of grains with  $[h00]$  and  $[hhh]$  in the pseudo-cubic structure in the remanent state. (d) Structural transformation of pseudo-cubic grains to tetragonal (red) and rhombohedral (blue) symmetry due to ferrodistorptive and ferrodistorptive + anti-ferrodistorptive instabilities, respectively. [Reproduced with permission from Ref. [257]].

was verified, a macroscopic shrinkage in direction perpendicular to the applied field was observed, alongside the appearance of  $\frac{1}{2}$  311 superstructure reflections (SSR), which indicated the transformation to the  $R3c$  structure. These SSR are related to changes in octahedral tilting that are coupled with polarization. In these grains, the strain is due to ferrodistorptive and antiferrodistorptive combined effects (Fig. 31d), defined as “*rotopolarization*” [257]. This synergy led to a large strain of about 2.4% under an applied field of 40 kV/cm, suggesting that the engineering of heterogeneous microstructure with core–shell features, having different polarization states and different octahedral tilting systems, could represent a breakthrough for the improvement of lead-free actuators.

The combination of polar ferrodistorptive and non-polar antiferrodistorptive effects on polarization and strain have been also reported for 0.93BNT-0.07BT single crystals [260]. *In-situ* synchrotron X-ray diffraction experiments showed that the crystal undergoes a reversible  $P4bm$ -to- $P4mm$  electric field-induced transition. The forward transition during electrical loading is triggered at an electric field around 20 kV/cm and caused a significant reduction of the superlattice reflection intensities related to the octahedral tilting of the  $P4bm$  phase. These superlattice reflections vanished at  $E = 100$  kV/cm, and the system showed only the presence of the ferroelectric tetragonal  $P4mm$  phase without octahedral tilting. During field reversal, the system returned to the  $P4bm$  phase with the reappearance of the superlattice reflections (Fig. 32a). Data extrapolated from the analysis of the diffraction experiments indicated that an electric field along the  $[0\ 0\ 1]$  direction increases the tetragonal distortion (Fig. 32b) and strain (see data points in Fig. 32c superimposed to the strain-electric field hysteresis loop) since the tilting of the  $TiO_6$  octahedra is increasingly suppressed during electrical loading [260]. Density functional theory (DFT) calculations carried out considering stoichiometric BNT show the variations of polarization due to the changes of the octahedral rotation angle induced by the electric field (Fig. 32d) in the structures of the  $T'$  phase (space group  $P4_2nm$ , which is a subgroup of the  $P4bm$  space group) and  $T$  phase (space group  $I4mm$ , which is a subgroup of the  $P4mm$  space group). The plot in the inset of Fig. 32d suggests that the polarization changes are recoverable, but hysteretic. The coupling between tilting suppression and polarization increase was coined as “*polarization twist*” [260]. It is envisaged that weakly-polar, ergodic relaxor materials with octahedral rotation would exhibit enhanced piezoelectric performance through the “*polarization twist*” effect, which adds up to polarization rotation and polarization extension mechanisms, well-known in conventional ferroelectrics.

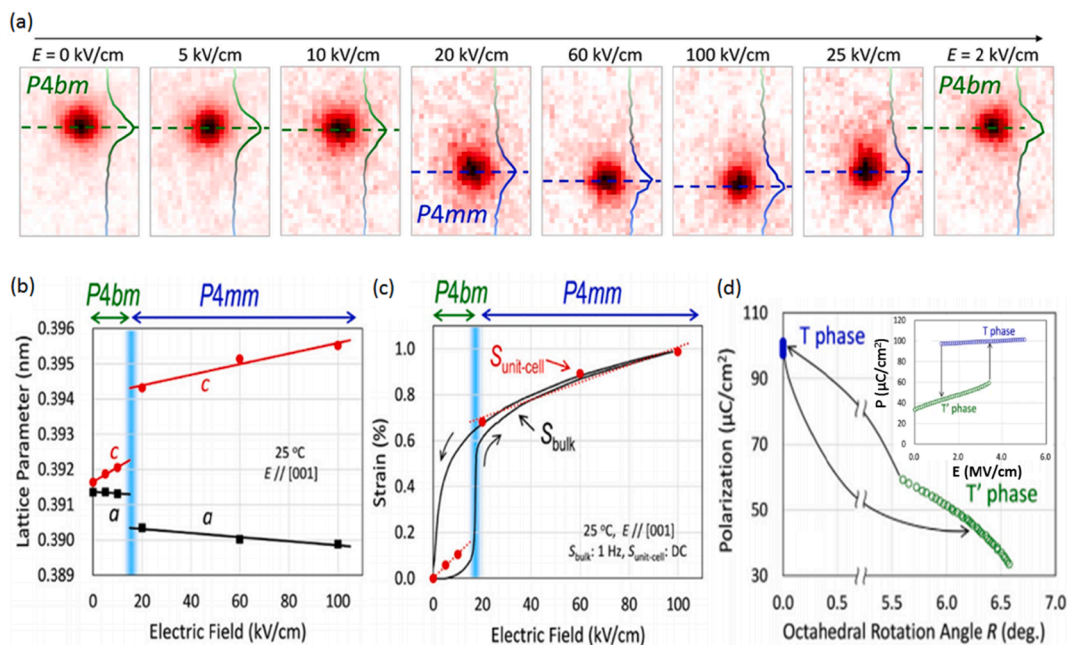


**Fig. 32.** (a) Shifts of the fundamental [138] reflection in 0.93BNT-0.07BT single crystals under different electric fields applied along the [0 0 1] direction; (b) lattice parameters change during the electric field-induced transition from  $P4bm$  to  $P4mm$  structure; (c) macroscopic strain ( $S_{\text{bulk}}$ ) and unit cell strain ( $S_{\text{unit-cell}}$ ) evolution during the application of the electric field; (d) polarization changes due to the electric field-induced changes of the octahedral rotation angle calculated by DFT simulations in the T' phase (space group  $P4_2nm$ , which is a subgroup of the  $P4bm$  space group) and T phase (space group  $I4mm$ , which is a subgroup of the  $P4mm$  space group) in stoichiometric BNT. [Reproduced with permission from Ref. [260]].

#### 4.12. Criticality phenomena

Electric field-temperature phase diagrams of non-ergodic and ergodic relaxors undergoing electric field-induced transitions often present the so-called *critical point* (CP), where the character of the electric field-driven transition changes from first order to second order. Due to different grain orientations, polycrystalline materials do not exhibit one critical point, but a smeared range of criticality, as found in various relaxor compounds [261–264]. In BNT-based materials, the existence of a critical range has been reported for 0.75BNT-0.25ST (Fig. 33a) [263] and 0.852(Bi<sub>0.5</sub>Na<sub>0.5</sub>TiO<sub>3</sub>)–0.028(BaTiO<sub>3</sub>)–0.12(Bi<sub>0.5</sub>K<sub>0.5</sub>TiO<sub>3</sub>) (Fig. 33b) [264], by measuring the latent heat involved in the electric field-induced transition at different temperatures and the relative characteristic electric fields. The latent heat ( $L$ ) was obtained from the specific heat ( $c_p$ ) and the temperature changes ( $\Delta T$ ) occurring in the sample during the EFIT:  $L = c_p \Delta T$ . It was found that the temperature of the sample increases during electrical loading, with a peak corresponding to the characteristic field driving the transition (see Fig. 33c–f relative to 0.75BNT-0.25ST) [263]. The increase of the sample's temperature due to the transition, and consequently the latent heat, reduce with increasing temperature. The extrapolation of the temperature at which the latent heat becomes zero provides the critical range of temperature (Fig. 33g, h), where the EFIT changes from first order to second order. The characteristic field of the electric field-induced transition initially decreases with increasing temperature, being minimum nearby  $T_{F-R}$ ; at  $T > T_{F-R}$ , it starts to increase again (Fig. 33h) [263]. By plotting the latent heat against the characteristic fields identified at the different temperatures, the critical range of characteristic field corresponding to  $L = 0$  can be extrapolated (Fig. 33g, 33 h), and the electric field-temperature phase diagrams can be outlined as those in Fig. 33a and b. In the absence of an applied electric field, both plots show the common temperature-induced transition from non-ergodic to ergodic relaxor phase at  $T_{F-R}$ . The application of an electric field in the non-ergodic phase causes the transition to the ferroelectric phase when the applied field matches the characteristic electric fields at the relative temperatures. The arrows pointing upward (Fig. 33b) indicate the irreversibility of this transition. In the ergodic phase, the field-induced transition to the ferroelectric state is reversible, as indicated by the arrows pointing downward (Fig. 33b) [263]. The hysteresis between the characteristic fields of the forward and backward transition decreases with increasing temperature until it vanishes at the beginning of the criticality range. It was demonstrated that the piezoelectric constant, strain actuation and electrocaloric effect are maximized nearby the temperature range of criticality, which represents an additional strategy to design materials with enhanced piezoelectric and electrocaloric properties [263].

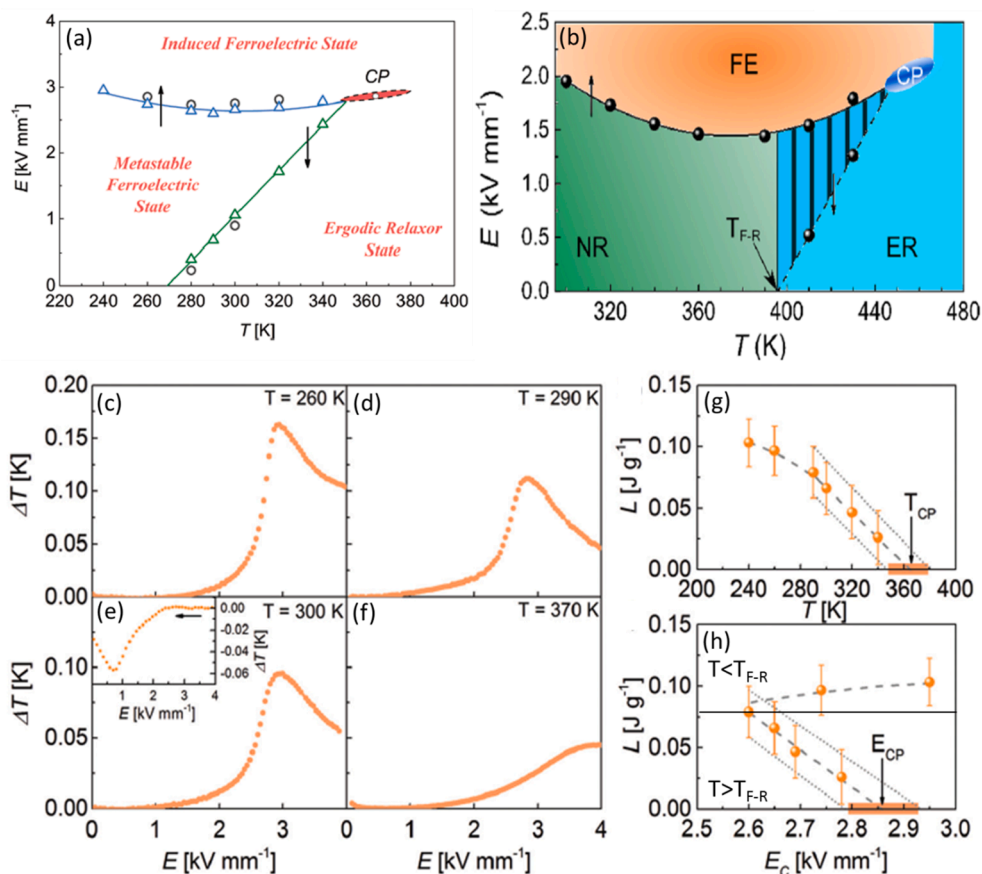


**Fig. 33.** Effects of electric field and temperature on the phase and range of critical points (CP) in 0.75BNT-0.25ST (a) and 0.852BNT-0.028BT-0.12BKT (b). [Reproduced with permission from Refs. [263] (Copyright 2016 John Wiley and Sons) and [264] (Copyright 2018 John Wiley and Sons), respectively]. (c)–(f) Temperature changes induced during electrical loading in samples of 0.75BNT-0.25ST ceramics at different external temperatures: 260 K (c), 290 K (d), 300 K (e) and 370 K (f). The inset in (e) refers to the temperature changes of the sample during electric field reversal. Extrapolation of critical points from latent heat: critical temperature points  $T_{CP}$  (g); critical electric field points  $E_{CP}$  (h). [Reproduced with permission from Ref. [263] Copyright 2016 John Wiley and Sons].

#### 4.13. Acoustic emissions during electric field-induced transformations

Acoustic emissions (AE) during the application of an electric field have been reported for ferroelectrics [265–267], relaxors [268] and antiferroelectrics [269]. For non-fatigued and non-aged ferroelectrics, acoustic emissions are usually recorded near or above the coercive field, and can have different possible origins [265,267,270,271], including (i) microcracking; (ii) structural changes; (iii) formation of new domain walls during domain nucleation; (iv) discontinuous movement of domain walls interacting with defects; (v) switching of ferroelastic domains; (vi) domain annihilation. For relaxor compositions, acoustic emissions have been detected in  $\text{Pb}_{0.905}\text{La}_{0.095}\text{Zr}_{0.65}\text{Ti}_{0.35}\text{O}_3$  and primarily attributed to microcracking [268]. For the antiferroelectric composition  $\text{Pb}_{0.97}\text{La}_{0.02}(\text{Zr}_{0.77}\text{Sn}_{0.14}\text{Ti}_{0.09})\text{O}_3$ , acoustic emissions events have been recorded at different stages of the electrical loading sequence and showed some differences depending on the grain size [269]. The first acoustic emissions appeared during the very first electrical loading cycle in both fine and coarse-grained ceramics, before the main change of strain associated with the antiferroelectric-to-ferroelectric electric field-induced transition, and were attributed to the ferroelectric domains nucleated within the antiferroelectric matrix [269]. The second type of AE events was also identified during the first loading cycle, soon after the major strain-change of the AFE-FE transition in both fine and coarse-grained samples and was imputed to different mechanisms, namely (i) the discontinuous jumps of ferroelectric domains within eight possible directions along the field direction; (ii) the annihilation of certain ferroelectric areas; (iii) microcracking. During unloading of the very first applied field, acoustic emissions were only recorded nearby zero-field in the fine-grained specimens and were attributed to the annihilation of the residual ferroelectric domains. For the subsequent cycles, acoustic emissions were also detected during the strain changes at the characteristic fields of the transition in the coarse grains, but not in the fine-grained sample. These have been attributed to overcoming the energy barriers created by the accumulation of charges in certain locations induced during the first poling cycle [269].

Acoustic emissions activity has been also monitored in different BNT-BT-KNN ceramics [272]. Fig. 34 shows that the composition 0.94BNT-0.05BT-0.01KNN presents a ferroelectric-type strain-electric field loop, with acoustic emissions around the coercive field

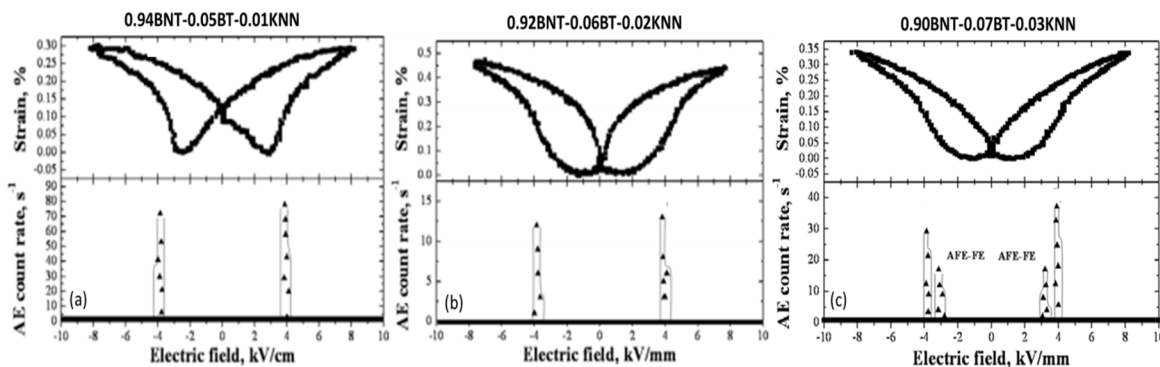


Fig. 34. Strain-electric field loops and acoustic emissions of 0.94BNT-0.05BT-0.01KNN (a), 0.92BNT-0.06BT-0.02KNN (b), and 0.90BNT-0.07BT-0.03KNN (c). [Reproduced with permission from Ref. [272] Copyright 2009 Elsevier].

(Fig. 34a), attributed to discontinuous domain wall motion. The ceramic of 0.92BNT-0.06BT-0.02KNN presents a relaxor-like strain-electric field loop, and acoustic emissions occur around 40 kV/cm (Fig. 34b). The 0.90BNT-0.07BT-0.03KNN ceramics showed the additional acoustic emissions corresponding to the electric field-induced transition from the antiferroelectric-like phase to a ferroelectric state (Fig. 34c) [272].

More recently, acoustic emissions have been detected in  $(1-x)\text{BNT}-x\text{BT}$  ( $x = 0, 0.02, 0.025, 0.0325$  and  $0.06$ ) single crystals [273], as shown in Fig. 35, which is relative to the compositions  $x = 0$  and  $x = 0.06$ . It can be noticed that undoped BNT and also compositions with  $x = 0.02-0.0325$  (not shown here) display acoustic emission events with various intensities at four different temperatures, namely  $T_d$ ,  $T_{LM}$ ,  $T_{RE}$  and  $T_m$ . The composition with  $x = 0.06$  exhibits an additional AE event, which has the largest intensity at the temperature  $T_p > T_m$ , which was attributed to the tetragonal-to-cubic phase transition [273]. The dependence of the acoustic emission intensity at  $T_{LM}$  is characterized by the presence of two maxima with increasing bias field. The first maximum is found at  $E_{pnr}$  corresponding to the steepest decrease of  $T_{LM}$  with increasing bias, while the second maximum identifies the critical point CP (see Fig. 20b).

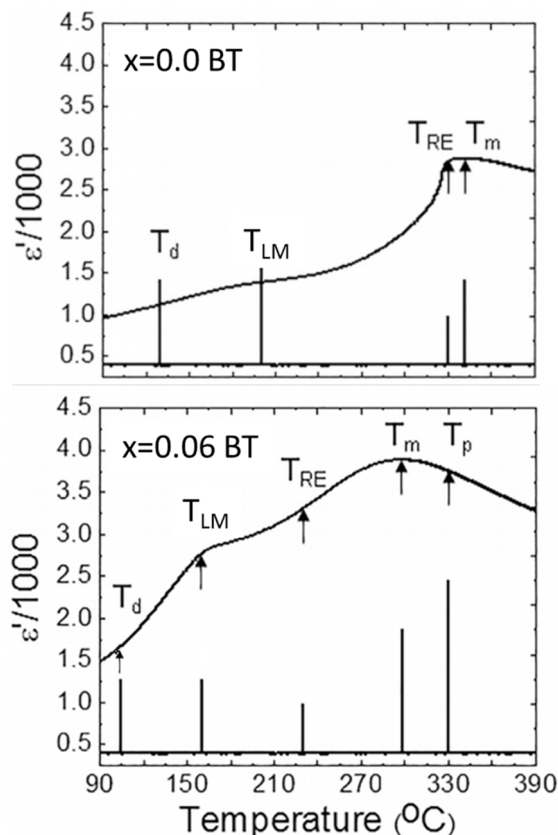
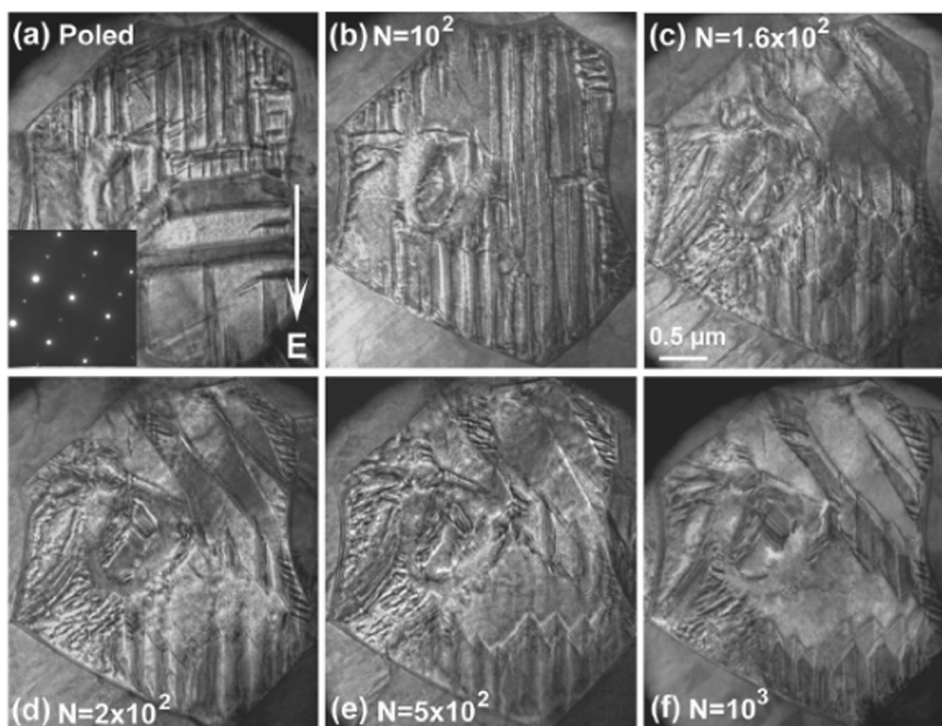


Fig. 35. Temperature dependence of dielectric permittivity and identification of characteristic temperature via acoustic emission in single crystals of BNT (a) and 0.94BNT-0.06BT (b). [Reproduced with permission from Ref. [273]].

#### 4.14. Role of electric field-induced transformations on the fatigue behaviour of BNT-based ceramics

There is a general consensus that electric field-induced phase transformations play an important role in the fatigue behaviour of relaxor-ferroelectrics [274,275]. Non-ergodic relaxors undergo irreversible electric field-induced transitions to a ferroelectric state during electrical loading and generally exhibit similar fatigue effects to conventional lead-based ferroelectrics, including a decrease of maximum polarization, strain, permittivity and piezoelectric coefficient, as well as an increase of the coercive field, as observed in 0.94BNT-0.06BT ceramics after  $10^4$  unipolar and bipolar electrical cycles [276,277]. Conversely, a slight decrease of the coercive field has been observed in other non-ergodic relaxor ceramics, including  $0.575(\text{Bi}_{0.5}\text{Na}_{0.5})\text{TiO}_3\text{-}0.4(\text{Bi}_{0.5}\text{K}_{0.5})\text{TiO}_3\text{-}0.025\text{Bi}(\text{Zn}_{0.5}\text{Ti}_{0.5})\text{O}_3$  [278] and  $0.59(\text{Bi}_{0.5}\text{Na}_{0.5})\text{TiO}_3\text{-}0.4(\text{Bi}_{0.5}\text{K}_{0.5})\text{TiO}_3\text{-}0.01\text{Bi}(\text{Mg}_{0.5}\text{Ti}_{0.5})\text{O}_3$  [279], that could be due to an increased ergodicity induced during repeated electrical cycles. The observed fatigue degradation of 0.94BNT-0.06BT under unipolar and bipolar cycles reported in Ref. [276] has been mainly attributed to domain wall pinning effects, with the additional contribution of mechanical damage after a high number of bipolar cycles, and extensive space charge accumulation during unipolar cycles. An additional fatigue mechanism was proposed by Simons et al. [280], who observed that 0.94BNT-0.06BT ceramics irreversibly transform to a ferroelectric state during the first 10 bipolar cycles; however, during subsequent cycles, the structural distortion could no longer be detected in the neutron diffraction patterns, suggesting a progressive reduction of domain size [280]. It was proposed that this domain miniaturization process is mainly due to domain wall pinning by charge carriers, and to the formation of new domain walls as a compensation effect of the hindered domain switching in pinned domains, which cause the reduction of polarization and strain during cycling [280]. Domain fragmentation was confirmed by transmission electron microscopy carried out on  $[(\text{Bi}_{0.5}\text{Na}_{0.5})_{0.95}\text{Ba}_{0.05}]_{0.98}\text{La}_{0.02}\text{TiO}_3$  non-ergodic relaxor ceramics [277].

The domain evolution during bipolar cycles is displayed in Fig. 36, which compares the domain structure in the initial poled state (Fig. 36a) and after 100 (Fig. 36b), 160 (Fig. 36c), 200 (Fig. 36d), 500 (Fig. 36e) and 1000 cycles (Fig. 36f). It can be seen that the domain configuration induced by the initial poling is significantly modified after 100 cycles, as the lamellar domains start breaking apart, and progressively split into smaller size domains during further cycling. The reduction of domain size was attributed to the pinning of charged domain walls by charge carriers during the possible multistep switching processes involved in the  $180^\circ$  polarization reversal in the rhombohedral structure [277]. Electrical bipolar cycles applied to 0.94BNT-0.06BT and 0.93BNT-0.07BT ceramics resulted in an initial increase of the tetragonal and rhombohedral phase; subsequent electrical cycles induced the predominance of rhombohedral and tetragonal phases, respectively, resulting in 57% and 66% decrease of the remnant polarization in the two respective ceramic types [281]. The addition of 1 mol% of Cu in 0.94BNT-0.06BT ceramics was found to significantly reduce the degradation of polarization and strain, and to prevent the formation of microcracks during 100 bipolar cycles [282]. The improved fatigue resistance was attributed to the suppression the electric field-induced transition from rhombohedral to tetragonal structure and



**Fig. 36.** Evolution of the domains configuration during bipolar electrical cycles in [1 1 2]-aligned grain. The images are bright field micrographs taken: a) in the initially poled state at 30 kV/cm and after (b) 100; (c) 160; (d) 200; (e) 500; and (f) 1000 cycles of bipolar electric fields. The inset in Fig. 37(a) is the diffraction pattern of the initial poled state. [Reproduced with permission from Ref. [277] Copyright 2019 John Wiley and Sons].

to the reduction of the electrical conductivity that hinders charge carriers migration and consequently domain wall pinning [282]. The influence of additional variables, such as electric field amplitude and frequency, temperature and DC bias on the fatigue process has been studied on 0.94BNT-0.06BT ceramics [283]. The effect of the electric field amplitude has been evaluated with cycles below and above the critical field that induces the relaxor-ferroelectric transition. In both regimes, the dependence on the amplitude  $E_{max}$  has been quantified using an empirical relationship of the type:  $E_{max}(N_{fail})^a = C$ , where  $N_{fail}$  represents the number of cycles that determined 10% loss of maximum polarization, and  $a$  and  $C$  represent fitting parameters. For amplitudes below the critical field, the number of cycles  $N_{fail}$  is significantly higher than the case of amplitudes larger than the critical field. For  $E_{max} < E_{cr}$ , the fatigue process is reversible and most likely controlled by domain wall pinning in the ferroelectric phase, which can be still induced below  $E_{cr}$  during cycling. For  $E_{max} > E_{cr}$ , the fatigue process based on domain wall pinning is accompanied by electrode delamination and by the formation of a thin blocking layer (about 100  $\mu\text{m}$ ), which hinders domain switching, decreasing the polarization during cycling. The hysteresis loops of unfatigued samples can be re-established by removing the blocking layer and re-coating the electrodes [283]. The effect of the frequency  $f$  on fatigue degradation was studied in the range  $E_{max} > E_{cr}$  and a non-monotonic trend has been observed. By increasing the frequency in the range 1 Hz-10 Hz, the  $N_{fail}$  value increases, according to the following relationship:  $N_{fail} = 4f^b$ , where  $b$  is a fitting parameter. This is due to the fact that higher frequency determines lower extent of domain switching, lower point defect migration and retained growth of eventual cracks. At larger frequencies, self-heating effects determine a decrease of  $N_{fail}$  values [283]. A similar effect was observed with increasing the temperature up to 70 °C ( $< T_f$ ), at  $E_{max} = 42$  kV/cm and 10 Hz. The enhanced fatigue degradation was attributed to a reduction of  $E_{cr}$  and an increased mobility of oxygen vacancies at higher temperature. The superposition of a DC bias greater than 7 kV/cm to a triangular wave of 42 kV/cm amplitude and 10 Hz frequency at room temperature determined an improved fatigue resistance, due to the suppression of domain switching [283]. A recent study on 0.94BNT-0.06BT ceramics has highlighted the impact of the surface layer (see section 2) on the fatigue properties [284]. It was found that the fatigue damage is mainly confined to the surface layer, and that the removal of the latter heals fatigue-induced degradation. Additionally, it was shown that the choice of electrodes has an effect also on the type of fatigue damage; in fact, permanent damage occurred in samples with platinum electrodes, but it was absent in samples with indium tin oxide (ITO) electrodes [284]. Platinum electrodes allow lower migration of oxygen vacancies compared to ITO electrodes; therefore, oxygen vacancies might be blocked at the ceramic-electrode interface. Additionally, disrupted concentration profiles of cations were found in fatigued ceramics with platinum electrodes, while ceramics with ITO electrodes showed similar cation profiles in unfatigued and fatigued samples [284].

BNT-based ergodic relaxors experience reversible transitions to a ferroelectric state during electrical loading and display high fatigue resistance [274]. For example, 0.91BNT-0.06BT-0.03KNN ceramics exhibited stable hysteresis loops and piezoelectric coefficient with only a reduction of permittivity under bipolar electrical loading up to  $10^6$  cycles [276]. In some cases, fatigued ergodic relaxor ceramics show even an increase of strain compared to unfatigued samples, possibly due to a higher degree of ergodicity induced during cycling [285]. Furthermore, BNT-based ergodic relaxors have shown good fatigue resistance at different temperatures [286]. The improved fatigue endurance compared to non-ergodic relaxor ceramics is mainly attributed to the absence of domain wall pinning. In ergodic relaxors, domains repeatedly appear and disappear during electrical cycles, preventing defect agglomeration to domain walls and consequent pinning [274]. Additionally, in ergodic relaxors, there is no significant strain mismatch between domains with different orientations; therefore, they are less prone to mechanical damage during polarization reversal compared to non-ergodic relaxors and ferroelectric systems [274,276,286]. On the other hand, BNT-based ergodic relaxors have been found to suffer of unipolar fatigue, as reported for the case of 0.91BNT-0.06BT-0.03KNN ceramics, which were found to display asymmetric strain-electric field loops and a slight reduction of maximum polarization [276]. The strain asymmetry is a signature of the presence of an internal bias field, created by charge carrier drift driven by the local depolarizing fields, which build-up when the polarization is increased by the external field during unipolar cycling [274,276]. Similar to non-ergodic relaxor ceramics, additional factors contributing to fatigue of ergodic relaxors are represented by electrode delamination and the formation of a blocking layer [287].

## 5. Relevance of electric field-induced transformations in technological applications of BNT-based materials

EFITs have significant technological implications in a broad range of engineering sectors. The development of high-performance BNT-derived materials based on the exploitation of EFITs is being carried out by a large number of research groups, in academia and industries. The main achievements and possible future trends have been summarized in previous review papers focused on energy storage devices [24–26], lead-free actuators [27–29,142], and electrocaloric systems [30]. In order not to reproduce the knowledge already compiled in these reviews, only specific aspects will be here summarized, for the self-consistency of this paper. Additionally, insights on compositional design and promising strategies for the development of novel materials would be provided.

### 5.1. Energy storage capacitors

It is well-known that the basic energy storage properties of a dielectric material can be obtained from the polarization vs electric field curves, from which the total energy density  $W_{tot}$ , the recoverable energy density  $W_{rec}$ , the dissipated energy density  $W_{dis}$  and the efficiency  $\eta_{es}$  can be respectively estimated as:

$$W_{tot} = \int_0^{P_{max}} E(P)dP, \quad \text{using the loading curve;} \quad (4)$$

G. Viola et al.

$$W_{rec} = \int_{P_r}^{P_{max}} E(P)dP, \quad \text{using the unloading curve;} \quad (5)$$

$$W_{dis} = W_{tot} - W_{rec}, \quad (6)$$

$$\eta_{es} = \frac{W_{rec}}{W_{tot}}. \quad (7)$$

Fig. 37 shows the recoverable energy density in linear dielectrics (Fig. 37a), ferroelectrics (Fig. 37b), relaxors (Fig. 37c) and antiferroelectrics undergoing AFE-FE electric field-induced transitions (Fig. 37d). In general, the recoverable energy density increases as shown in the figure succession for the different types of dielectrics, being usually maximized in antiferroelectrics experiencing reversible AFE-FE field-induced transitions.

Being relaxor-like in nature, BNT-based materials could represent a valid selection for energy storage capacitors in high power applications. The possibility of using BNT-related materials as lead-free materials in energy storage devices was initially recognized about a decade ago [288–290]. Since then, many different compositional variants have been developed, with the aim of achieving high recoverable energy density, high efficiency and high thermal stability. High recoverable energy density in BNT-based materials is usually obtained in the ergodic relaxor state, and it can be increased by increasing the electric breakdown strength, the characteristic fields  $E_F$  and  $E_R$  and by reducing their difference, which would also lead to increased efficiency. The thermal stability can be improved by reducing the temperature  $T_{F-R}$  and increasing the transition temperature to the paraelectric phase. An additional important parameter for energy storage materials is represented by the fatigue resistance, which has been reported to be remarkably high (up to  $10^6$  cycles) in ergodic relaxor compositions, such as 0.91BNT-0.06BNT-0.03KNN [276]. One of the largest recoverable energy densities in BNT-based bulk ceramics at room temperature has been achieved in the ceramic systems  $(1-x)\text{Bi}_{0.5}\text{Na}_{0.5}\text{TiO}_3\text{-}x\text{Sr}_{0.7}\text{La}_{0.2}\text{TiO}_3$  with  $x = 0.45$ , which has shown a recoverable energy density of  $4.14 \text{ J/cm}^3$  under an applied field of  $315 \text{ kV/cm}$ , mainly attributed to the large breakdown strength and to the stabilization of the relaxor state [291]. A recoverable energy density of  $3.2 \text{ J/cm}^3$  under an applied field of  $280 \text{ kV/cm}$  has been obtained in  $0.65\text{Bi}_{0.51}\text{Na}_{0.47}\text{Ti}_{0.9875}\text{Nb}_{0.01}\text{O}_3\text{-}0.35\text{Ba}(\text{Ti}_{0.7}\text{Zr}_{0.3})\text{O}_3$ , still mainly attributed to a large breakdown strength [292]. A separate publication has reported a recoverable energy density of  $3.08 \text{ J/cm}^3$  under an applied field of  $220 \text{ kV/cm}$  for the composition  $0.96(0.65\text{Bi}_{0.5}\text{Na}_{0.5}\text{TiO}_3\text{-}0.35\text{Sr}_{0.85}\text{Bi}_{0.1}\text{TiO}_3)\text{-}0.04\text{NaNbO}_3$  [293]. This has highlighted a potential strategy to improve energy storage properties, namely the introduction of Nb in the B-site, which has two major effects: (i) an increase of polarization due to the large intrinsic polarizability of Nb; (ii) the formation of a core-shell type microstructure, which enhances the breakdown strength [293]. Additionally, based on the high chemical complexity of these systems, there is also the possibility that the

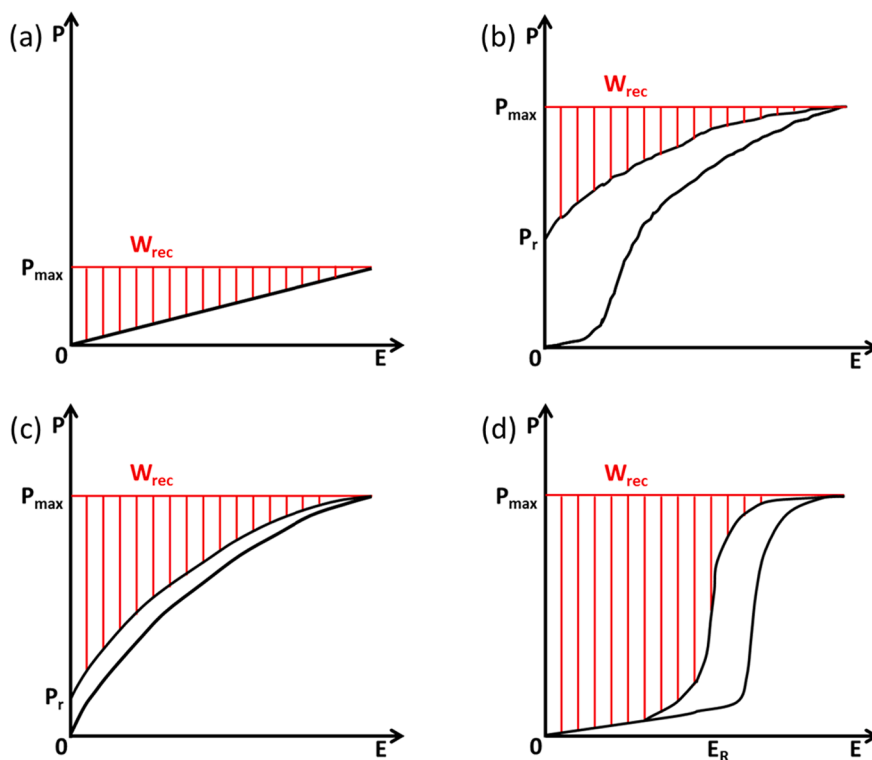


Fig. 37. Schematic polarization–electric field loops and energy density in different types of dielectrics: (a) linear dielectric; (b) ferroelectrics; (c) relaxors; and (d) antiferroelectrics.

large breakdown strength and polarizability may arise from the compositional disorder on both the A- and B-site. This hypothesis has been also discussed relatively to  $\text{Sm}_{0.03}\text{Ag}_{0.91}\text{NbO}_3$  [294] and could be worthy of further investigation also for other BNT-based materials. As far as the efficiency is concerned, one of the highest values at room temperature has been obtained in  $0.65\text{Bi}_{0.51}\text{Na}_{0.47}\text{Ti}_{0.9875}\text{Nb}_{0.01}\text{O}_3-0.35\text{Ba}(\text{Ti}_{0.7}\text{Zr}_{0.3})\text{O}_3$  ( $\eta_{es} = 93.1\%$ ) [292]. Additionally, a series of Sr-containing compounds have commonly showed high efficiency, for example  $0.62\text{Bi}_{0.5}\text{Na}_{0.5}\text{TiO}_3-0.06\text{BaTiO}_3-0.32(\text{Sr}_{0.7}\text{Bi}_{0.2})\text{TiO}_3-x\text{Mn}$  with  $x = 1 \text{ mol}\%$  ( $\eta_{es} = 92\%$ ) [295],  $0.65(0.84\text{Bi}_{0.5}\text{Na}_{0.5}\text{TiO}_3-0.16\text{Bi}_{0.5}\text{K}_{0.5}\text{TiO}_3)-0.35(\text{Sr}_{0.7}\text{Bi}_{0.2})\text{TiO}_3$  ( $\eta_{es} = 87.3\%$ ) [296]  $\text{Sr}_{0.3}(\text{Bi}_{0.7}\text{Na}_{0.67}\text{Li}_{0.03})_{0.5}\text{TiO}_3$  ( $\eta_{es} = 87.2\%$ ) [297] and  $0.55(\text{Bi}_{0.5}\text{Na}_{0.5})\text{TiO}_3 - 0.45(\text{Sr}_{0.7}\text{Bi}_{0.2})\text{TiO}_3$  multilayer capacitors ( $\eta_{es} = 92\%$ ) [298]. The large efficiency in these compositions is related to the slim P-E loops, which are due to stabilization of the ergodic relaxor state (or non-linear paraelectric state) around room temperature, most likely related to the presence of strontium in the A-site.

Two additional strategies to improve energy storage properties have been identified as: (i) the engineering of materials undergoing multiple electric field-induced transitions, as reported for the lead-based material  $(\text{Pb}_{0.98}\text{La}_{0.02})(\text{Zr}_{0.55}\text{Sn}_{0.45})_{0.995}\text{O}_3$  [299]; (ii) the design of materials according to the polarization mismatch approach, as described in a recent review [300] and applied to the system  $(1-x)\text{BaTiO}_3-x\text{Bi}(\text{Mg}_{0.5}\text{Ti}_{0.5})\text{O}_3$  ( $0.1 \leq x \leq 0.4$ ) [301].

It is believed that  $(\text{Pb}_{0.98}\text{La}_{0.02})(\text{Zr}_{0.55}\text{Sn}_{0.45})_{0.995}\text{O}_3$  undergoes a transition from the antiferroelectric to the first ferroelectric phase FE(I), and subsequently to another ferroelectric phase FE(II) with increasing the applied field. This sequence has been hypothesized based on the shape of the P-E loop shown in Fig. 38a, from which an energy density of  $10.4 \text{ J/cm}^3$  under an applied field of  $40 \text{ kV/cm}$  was estimated. The relative field-induced structures are yet to be determined [299].

The polarization mismatch approach in perovskites consists of introducing specific types of ions in the A- and B-site that would impede long-range ferroelectric order [300]. This can be for instance achieved by designing solid solutions with two end members, whose ferroelectricity is established by the hybridization between A-site cations and oxygen (A—O coupling), as well as B-site cations and oxygen (B—O coupling). Such a solid solution would be unable to establish none of these long-range ferroelectric orders, giving rise to relaxor-like characteristics, with low  $T_m$ , a U-like dependence of  $T_m$  on composition, broad dielectric peaks and slim P-E loops, which characterize the so-called *polarization-mismatched ferroelectrics* (PMFES) [300]. An example of PMFES is represented by  $(1-x)\text{BaTiO}_3-x\text{Bi}(\text{Mg}_{0.5}\text{Ti}_{0.5})\text{O}_3$ , which contains the simultaneous presence of Bi (which enhances A—O coupling-based ferroelectricity) and Ba (which disrupt ferroelectricity based on A—O type coupling) on the A-site, and of Ti (which enhances B—O coupling-based ferroelectricity) and Mg (which disrupts B—O coupling-based ferroelectricity) on the B-site. These mechanisms led to a slim P-E loop with a recoverable energy density of  $4.49 \text{ J/cm}^3$  and an efficiency of 93% for the composition with  $x = 0.4$  (Fig. 38b) [301].

Besides, the above-mentioned studies [299,301] have highlighted the importance of the rolling forming process in enhancing the breakdown strength of the ceramics. The process consists of forming a ceramic tape using two contiguous counter-rotating rollers, which apply a large force on the green body, enhancing the compaction and minimizing porosity during sintering. The breakdown strength can be also improved by producing grain texture, as recently demonstrated for the case of [111]-textured  $0.65(\text{Bi}_{0.5}\text{Na}_{0.5})\text{TiO}_3 - 0.35(\text{Sr}_{0.7}\text{Bi}_{0.2})\text{TiO}_3$  multilayer capacitors [302].

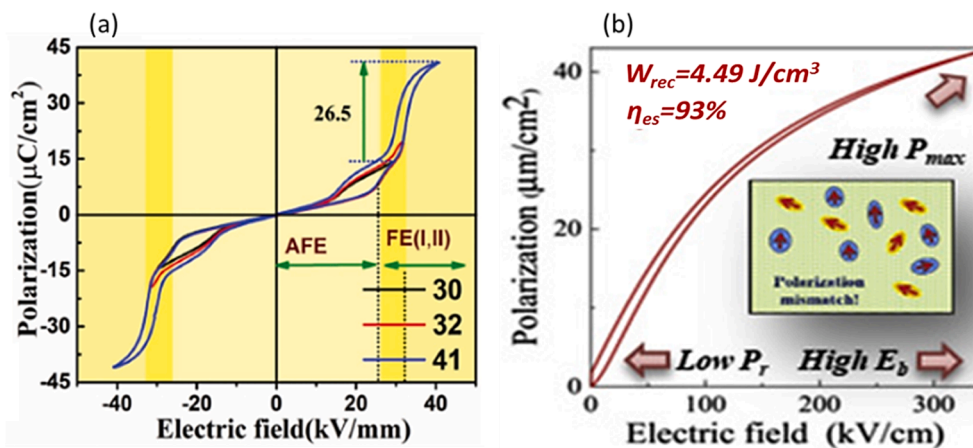


Fig. 38. Polarization-electric field hysteresis loops of  $(\text{Pb}_{0.98}\text{La}_{0.02})(\text{Zr}_{0.55}\text{Sn}_{0.45})_{0.995}\text{O}_3$  (a) and  $0.6\text{BaTiO}_3-0.4\text{Bi}(\text{Mg}_{1/2}\text{Ti}_{1/2})\text{O}_3$  [Reproduced with permission from Ref. [299] Copyright 2019 John Wiley and Sons]; (b). [Reproduced with permission Ref. [301] Copyright 2020 Elsevier].

## 5.2. Actuators

The importance of electric field-induced transitions for the development of lead-free actuators was initially recognized in 2007 by Zhang et al. [303] who obtained a strain of 0.45% for the composition  $0.92\text{Bi}_{0.5}\text{Na}_{0.5}\text{TiO}_3\text{-}0.06\text{BaTiO}_3\text{-}0.02\text{K}_{0.5}\text{Na}_{0.5}\text{NbO}_3$  at 80 kV/cm. This strain value is higher than that experienced by some typical lead zirconate titanate-based ferroelectrics (with strain typically in the range 0.2–0.35%) and is comparable to those obtained in lead-based antiferroelectrics. The large strain in  $0.92\text{BNT}\text{-}0.06\text{BT}\text{-}0.02\text{KNN}$  was ascribed to a reversible electric field-induced transition from the ergodic relaxor to the ferroelectric state, which produces only expansion along the applied field direction, from a nearly-zero remnant strain state [303]. This behaviour gives rise to strain-electric field loops with characteristic *sprout-like* shapes, as opposed to *butterfly-like* shapes displayed by conventional ferroelectrics [27]. Apart from the maximum strain  $S_{max}$ , other important parameters, such as the piezoelectric coefficient  $d_{33}^*$ , commonly defined from the unipolar tests as  $d_{33}^* = \frac{S_{max}}{E_{max}}$  (with  $E_{max}$  being the maximum applied field), the fatigue resistance, the thermal stability and the blocking force, are used to assess the performance of materials for actuators [27,29].

One of the largest  $d_{33}^*$  values has been reported for  $0.8[0.94\text{Bi}_{0.5}(\text{Na}_{0.75}\text{K}_{0.25})_{0.5}\text{TiO}_3\text{-}0.06\text{BiAlO}_3]\text{-}0.2(\text{Bi}_{0.5}\text{Na}_{0.5})\text{TiO}_3$  composites sintered at 1150 °C ( $d_{33}^* = 930$  pm/V) with a maximum strain of 0.37% at 40 kV/cm [304]. These outstanding properties were found to be sensitive to the sintering time, and were attributed to an effect of favourable grain size and chemical element distribution [304]. Subsequently, the idea of fabricating composites for actuators has been explored by adding seeds of a non-ergodic relaxor phase to an ergodic relaxor matrix [305–308]. The addition of the non-ergodic phase brings about a reduction of the critical field and improves the temperature and frequency stability of electroceramic composites by tailoring the phase fractions of matrix and seeds [305–308]. Based on a numerical model, Groh et al. identified two important selection criteria to design composites with improved actuating performance: (i) the remnant polarization of the non-ergodic seed phase should be comparable with saturation polarization of the ergodic phase of the matrix; and (ii) the coercive field of the seed phase should be lower than the critical field of the ergodic matrix [308].

More recent studies on BNT-derived solid solutions reported remarkably high  $d_{33}^*$  coefficients in  $0.74\text{Bi}_{0.5}\text{Na}_{0.5}\text{TiO}_3\text{-}0.26\text{SrTiO}_3$  ( $d_{33}^* = 1100$  pm/V) [309] and  $[(\text{Bi}_{0.5}\text{Na}_{0.5})_{0.935}\text{Ba}_{0.065}]\text{Ti}_{0.98}(\text{Fe}_{0.5}\text{Nb}_{0.5})_{0.02}\text{O}_3$  ( $d_{33}^* = 844$  pm/V) [310], which were attributed to the favourable coexistence of relaxor and relaxor-ferroelectric phases. However, according to the comparison presented in the recent review paper [29], it seems that large  $d_{33}^*$  values can be achieved in complex compositions, with the simultaneous presence of various ions on both the A- and B-site, suggesting that compositional disorder could be also beneficial for obtaining enhanced actuation properties. Recently, high unipolar strain of 0.74% was achieved combining the contributions from domain switching, field-induced transition and oxygen vacancies [311].

An additional strategy to improve the electric field-induced strain in BNT-based compounds involves grain texturing. The textured ceramics have constantly shown significantly larger  $d_{33}^*$  values than samples with randomly oriented grains [29]. Furthermore, it has been demonstrated that the electric field-induced strain in textured ceramics depends on the different template particles, which has significant effects on the structure [310]. While it is evident that the grain texture induces a notable increase of the electro-strain, the effects of grain orientation on the mechanisms of EFITs have not been comprehensively explored, and additional studies are needed to shed more light on the following aspects: (i) the effects of the processing methods and template type on the final grain texture; and (ii) the effects of grain texture on the field-induced transformations and relative properties.

## 5.3. Electrocaloric systems

EFITs taking place in BNT-based materials provide viable possibilities for the development of lead-free materials for electrocaloric applications. The electrocaloric effect in a polar dielectric involves a temperature increase during the application of an electric field under adiabatic conditions that compensates the reduction of entropy occurring during the orientation of the polarization along the applied field direction. If the dielectric is in contact with a heat sink, it cools down lowering its entropy, while the degree of polarization alignment further increases. The removal of the applied field under adiabatic conditions causes an increase in entropy since the depolarization process is compensated by an increase in temperature [312]. The electrocaloric behaviour is characterized by a temperature increase  $\Delta T_{ec}$ , which can be measured during the application of the field ( $\Delta T_{ec} > 0$ ) or during field removal ( $\Delta T_{ec} < 0$ ). Another important property often used to compare different materials is represented by the electrocaloric responsivity  $\xi$ , defined as  $\xi = \frac{\Delta T_{ec,max}}{\Delta E_{max}}$ , where  $\Delta T_{ec,max}$  is the maximum temperature difference achievable within the temperature range considered, and  $\Delta E_{max}$  is the amplitude of the applied field. According to thermodynamics laws, the expression of parameter  $\Delta T_{ec}$  during the application of an electric field  $E$  from  $E_1$  to  $E_2$  (generic values) can be derived as [30]:

$$\Delta T_{ec} = -\frac{T}{c_E} \int_{E_1}^{E_2} \left( \frac{\partial P_r(E, T)}{\partial T} + \epsilon_0 E \frac{\partial \epsilon_r(T, E)}{\partial T} \right) dE, \quad (8)$$

where  $c_E$  is the specific heat at a constant electric field,  $\epsilon_0$  the vacuum permittivity,  $\epsilon_r$  the relative permittivity,  $P_r$  the remnant polarization, and  $T$  is the temperature.

From the expression (8), one can deduce that the sign of  $\Delta T_{ec}$  depends on the relative contributions of  $\frac{\partial P_r(E, T)}{\partial T}$  and  $\frac{\partial \epsilon_r(T, E)}{\partial T}$ . For ferroelectric materials,  $\frac{\partial P_r(E, T)}{\partial T} < 0$  and  $\frac{\partial \epsilon_r(T, E)}{\partial T} > 0$  at temperatures below the Curie point, whereas above the Curie point the remnant polarization  $P_r \approx 0$  and, most commonly,  $\frac{\partial \epsilon_r(T, E)}{\partial T} < 0$ . Hence, the latter case results in a positive  $\Delta T_{ec}$  parameter. According to the definitions of  $\Delta T_{ec}$  and  $\xi$ , relaxors with electrical dipoles randomly aligned in absence of an external field, but highly ordered under weak

electric fields, could be appropriate candidates for solid-state refrigeration. In addition, BNT-based ceramics undergoing first-order EFTs would provide an additional contribution to the electrocaloric effect due to the latent heat released during the transformation [30].

The electrocaloric effect can be enhanced near the critical point (CP), where the energy barriers between the coexisting polar phases can be overcome by small electric fields [313]. Weyland et al. have reached almost 25% enhancement of the electrocaloric effect in  $0.75\text{Bi}_{0.5}\text{Na}_{0.5}\text{TiO}_3\text{-}0.25\text{SrTiO}_3$  ceramics near the critical point ( $\approx 100^\circ\text{C}$ ), yielding  $\Delta T_{ec} \approx 0.4^\circ\text{C}$  under an applied field of 40 kV/cm [263].

A separate study on  $(1-x)\text{Bi}_{0.5}\text{Na}_{0.5}\text{TiO}_3\text{-}x\text{KbNbO}_3$  solid solutions reported maximum electrocaloric effect at a temperature close to  $T_{LM}$  with  $\Delta T_{ec,max} = 1.5^\circ\text{C}$  under 70 kV/cm for compositions corresponding to the morphotropic phase boundary ( $x = 0.06$ ) [314]. The importance of the MPB composition in maximizing the electrocaloric properties has been also highlighted in subsequent studies on  $0.95[0.94(\text{Bi}_{0.5}\text{Na}_{0.5-x}\text{Li}_x)\text{TiO}_3\text{-}0.06\text{BaTiO}_3]\text{-}0.05\text{CaTiO}_3$  ( $x = 0\text{--}0.15$ ), with  $\Delta T_{ec,max} = 1.56^\circ\text{C}$  at  $115^\circ\text{C}$  under an applied field of 50 kV/cm for  $x = 0.05$  [315]. The structurally-similar system  $(1-x)\text{Bi}_{0.5}\text{K}_{0.5}\text{TiO}_3\text{-}x\text{La}(\text{Mg}_{0.5}\text{Ti}_{0.5})\text{O}_3$  showed  $\Delta T_{ec} = 1.17^\circ\text{C}$  under a field of 40 kV/cm ( $\xi = 0.029^\circ\text{C cm/kV}$ ) at room temperature for the composition with  $x = 0.01$  [316].

According to the survey by Kumar et al. [313], the highest electrocaloric properties at room temperature within the BNT-based materials family are obtained in the system  $\{[\text{Bi}_{0.5}(\text{Na}_{0.84}\text{K}_{0.16})_{0.5}]\}_{0.96}\text{Sr}_{0.04}\}(\text{Ti}_{0.975}\text{Nb}_{0.025})\text{O}_3$  (BNKST-2.5Nb) with the electrocaloric parameters  $\Delta T_{ec} = 1.85^\circ\text{C}$  and  $\xi = 0.037^\circ\text{C cm/kV}$ , as obtained by an indirect measurement around  $T_{LM}$  ( $\sim 30^\circ\text{C}$ ) [317]. It should be mentioned that although the parameter  $\Delta T_{ec}$  in BNT-based materials is usually much lower than those reported for lead-based and barium titanate-based ferroelectric materials (particularly in thin films), as well as PVDF-based ferroelectric polymers [313], the responsivity  $\xi$  parameter is often competitive [317].

A potentially novel approach for improving the electrocaloric properties relates to the development of high-entropy electroceramics based on compositional modifications of BNT. It has been recently reported that the compound  $(\text{Na}_{0.2}\text{Bi}_{0.2}\text{Ba}_{0.2}\text{Sr}_{0.2}\text{Ca}_{0.2})\text{TiO}_3$  experienced an adiabatic temperature change  $\Delta T_{ec} = 0.63^\circ\text{C}$  under an electric field of 60 kV/cm at  $40^\circ\text{C}$  [318].

#### 5.4. Photoluminescence

The phenomenon of photoluminescence (PL) essentially involves the excitation of electronic states by an external light source, resulting in the emission of light at different wavelengths [319]. The PL activity is strongly influenced by the crystal structure symmetry and the crystal field of the emitting material. Therefore, PL properties can be significantly altered by structural changes occurring during EFTs [320]. In general, crystal structures with low symmetry and high positional disorder provide more pathways for

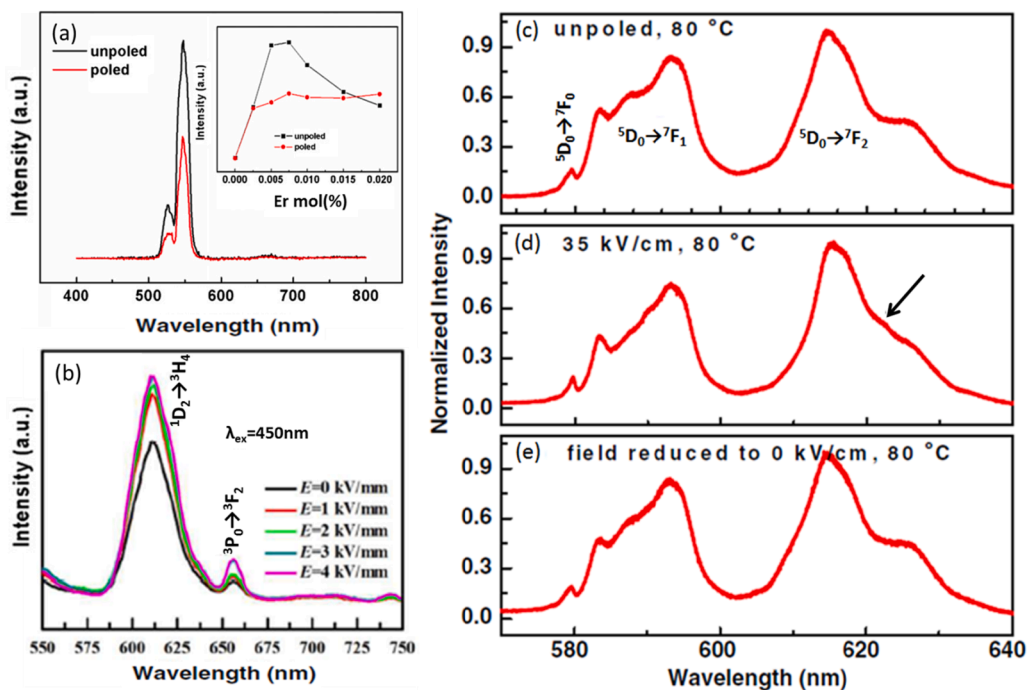


**Fig. 39.** Effects of an applied electric field on the photoluminescence properties of (a) Er-doped  $0.94\text{Bi}_{0.5}\text{Na}_{0.5}\text{TiO}_3\text{-}0.06\text{BaTiO}_3$  at room temperature [Reproduced with permission from Ref. [321] Copyright 2015 John Wiley and Sons]; and (b) Pr-doped  $0.93\text{Bi}_{0.5}\text{Na}_{0.5}\text{TiO}_3\text{-}0.07\text{BaTiO}_3$  at room temperature [Reproduced with permission from Ref. [159] Copyright 2015 American Chemical Society]. Variations of the photoluminescence spectrum of  $0.94(\text{Bi}_{0.5}\text{Na}_{0.5})\text{TiO}_3\text{-}0.06\text{BaTiO}_3$  at  $80^\circ\text{C}$  in as-sintered state (c), under an electric field of 35 kV/cm (d) and after removing the electric field (e) [Reproduced with permission from Ref. [320] <https://journals.aps.org/prl/abstract/10.1103/PhysRevLett.116.117601> Copyright 2016 American Physical Society].

radiation emission. EFITs can equally decrease or increase photoluminescence activity in certain wavelength ranges, depending on the changes of the crystal structure symmetry during the transformation. These effects have been observed in various rare-earth-modified BNT-based materials, which have shown the possibility of tailoring photoluminescence emissions depending on the type and amount of rare-earth species and on the specific structural modifications taking place during electric field-induced transformations [159,320–322].

Experimental studies on  $0.94\text{Bi}_{0.5}\text{Na}_{0.5}\text{TiO}_3\text{-}0.06\text{BaTiO}_3$  doped with erbium have shown a field-induced increase of green emission (band centred at  $\sim 550$  nm) due to  ${}^2\text{H}_{11/2}/{}^4\text{H}_{3/2} \rightarrow {}^4\text{I}_{15/2}$  transitions, as shown in Fig. 39a and inset, in compositions with 0.02% of Er [321]. The increased green emission was attributed to a structural transition from a nearly-cubic to a lower symmetry rhombohedral/tetragonal structure during poling. An enhancement of the PL activity in the range 580–680 nm (Fig. 39b) due to the field-induced transformation has been also reported for poled  $0.93(\text{Bi}_{0.5}\text{Na}_{0.5})\text{TiO}_3\text{-}0.07\text{BaTiO}_3$  ceramics doped with praseodymium [159]. More complicated poling-induced irreversible modifications of the PL spectra at room temperature have been reported for  $(\text{Bi}_{0.5}\text{Na}_{0.5})\text{TiO}_3$  and  $0.94(\text{Bi}_{0.5}\text{Na}_{0.5})\text{TiO}_3\text{-}0.06\text{BaTiO}_3$  doped with europium [320,323]. In contrast, reversible changes of the PL emissions have been observed for europium-doped  $0.94(\text{Bi}_{0.5}\text{Na}_{0.5})\text{TiO}_3\text{-}0.06\text{BaTiO}_3$  at  $80^\circ\text{C}$ , where the material is in the ergodic relaxor phase. The initial photoluminescence spectrum (Fig. 39c) is modified after the application of an electric field of 35 kV/mm; in particular, the peak relative to the  ${}^5\text{D}_0 \rightarrow {}^7\text{F}_2$  transition becomes a triplet (see black arrow in Fig. 39d). However, the initial PL spectrum is recovered after removing the field (Fig. 39e), in virtue of the reversible field-induced ergodic-ferroelectric transition [320].

## 6. Concluding remarks

In this review paper, the electric field-induced transformations taking place in bismuth sodium titanate and derived materials have been comprehensively surveyed, by compiling the current understanding of crystal structure, microstructure and their field-induced modifications, obtained from detailed studies performed by numerous researchers over the recent years. The aspects here discussed provide a deep understanding of the relationships between the microscopic mechanisms of electric field-induced transformations and macroscopic properties, as well as general guidelines for a correct interpretation of the experimental observations. Based on the present survey, the following general conclusions can be drawn.

The crystal structure of BNT is complex, and the discussion on its exact symmetry is not completely settled. However, by combining the information obtained from ab initio calculations and experimental studies on local structures and defects, it can be inferred that the rhombohedral  $R3c$  structure with *A-type* configuration would be the most energetically favoured in stoichiometric BNT and that the monoclinic  $Cc$  structure sets-in because of the presence of microstructural inhomogeneity, defects and positional disorder of A-site cations. During the application of an electric field, the  $Cc$  structure of BNT transforms to the  $R3c$  structure, mainly through irreversible modifications of the A-site local environment.

Compositional variations of BNT do not affect only the crystal structure symmetry, but also the course of its temperature- and electric field-induced transformations. Modifications of the chemical composition can strengthen or weaken the polar order and its temperature stability depending on the elements added, and could induce the formation of morphotropic phase boundaries, which increase the complexity of EFITs phenomenology, but often result in improved properties. The general effect of increasing temperature is to induce a progressive destabilization of the initial polar state, with the sequential promotion of ergodic relaxor, and paraelectric states. The characteristic temperatures of these transformations can be identified from the temperature dependence of structure, dielectric and piezoelectric properties, as well as from the characteristics of the hysteresis loops. The latter usually contain specific signatures of the underlying electric field-induced transformations, related to the position of the characteristic peaks displayed in the current-electric field loops and to the shape of polarization- and strain-electric field curves. The frequency of the applied field affects the kinetics of the EFITs, as manifested by the shift of the characteristic fields of the hysteresis loops. The observed frequency-induced shifts occur because with increasing frequency less time is given to the underlying transformations to take place.

Additionally, for BNT-based materials, a wide range of electric field-induced phenomena have been identified, and can be summarized as follows.

- (i) *Bias field-induced shifts of characteristic temperatures, such as  $T_d$  and  $T_{F-R}$* : these can be attributed to the retardation of thermal depolarization effects.
- (ii) *Electric field-induced modifications of MPB structures*: these are characterized by characteristic sequences of appearance/disappearance of phases with different symmetry.
- (iii) *Reverse transformations from a ferroelectric to a relaxor-like state during reverse electrical loading*: the field-induced ferroelectric phase can be transformed to the initial relaxor-like phase by reversing the electric field.
- (iv) *Metastable nature of the electric field-induced domains in the ergodic relaxor state*: the field-induced ferroelectric domains disappear during electric field unloading.
- (v) *Large piezoelectricity achieved under low poling field*: high piezoelectric constant can be obtained by poling fields well-below the coercive field of the field-induced ferroelectric phase.
- (vi) *Deviations from Rayleigh-type behaviour in the ergodic relaxor state*: these can be attributed to electric field-driven transitions taking place under weak electric fields.
- (vii) *Cascade phenomena as a signature of electric field-induced transitions taking place over time under DC fields*: these can be identified by monitoring the time evolution of polarization and strain during the application of constant electric fields with specific magnitude.

- (viii) *Spatial heterogeneity of electric field-induced phase transformations*: EFITs manifest themselves as spatially inhomogeneous depending on various microstructural factors, including grains orientation and core-shell features. In particular, the extent of field-induced transitions is greater in grains where the polar direction of the structure is favourably oriented with the applied field. Remarkably, the core region, in core-shell structured relaxors, has been observed to undergo irreversible transformations from a non-ergodic relaxor to a ferroelectric state, while the shell experiences a reversible transformation from an ergodic relaxor to a ferroelectric state.
- (ix) *Rotostriction, rotopolarization, polarization twist mechanisms*: rotostriction is based on the coupling between octahedral and strain, while rotopolarization and polarization twist indicate the coupling between octahedral tilting and polarization. These couplings exist in specific microstructures and temperature conditions, where polar and weakly-polar phases coexist, due to the competition between ferrodistorptive (polar) and antiferrodistorptive (non-polar) instabilities. These mechanisms mediate the electric field-induced transformations and can be exploited to improve piezoelectric properties.
- (x) *Diffuse criticality phenomena*: due to the presence of grains with different orientations, EFITs often present a diffuse range of critical points, where their character changes from first order to second order (vanishing hysteresis between the characteristic fields of the forward and backward transitions). Piezoelectric and electrocaloric properties are maximized nearby the temperature range of criticality, indicating that chemical compositions and microstructures can be opportunely tuned to shift the criticality range and maximize desired properties in specific temperature ranges.
- (xi) *Acoustic emissions*: recording acoustic emissions can be useful to identify characteristic temperatures and electric field thresholds in cases where these cannot be clearly distinguished in the temperature dependence of dielectric and piezoelectric properties and in the hysteresis loops.

Electric field induced-transformations have a significant influence on the electrical fatigue behaviour. Non-ergodic BNT-based relaxors undergoing irreversible transitions to a ferroelectric state exhibit similar fatigue mechanisms observed in conventional ferroelectrics. The improved fatigue resistance of BNT-based ergodic relaxors is consensually attributed to the absence of stable domains structures, and to the low strain mismatch between polar regions with different orientations.

Electric field induced-transformations play a very important role in the design of materials for various applications, particularly for energy storage capacitors, actuators, electrocaloric systems and photoluminescent devices. The comparison of the relevant properties in different compositions allowed promising novel strategies to be outlined in order to improve specific functionalities, provided hints and guidelines for future materials development. Opportune compositional modifications that enhance the recoverable energy density and efficiency have been identified with the addition of strontium and niobium in A- and B-site and the introduction of compositional disorder therein. Specific processing techniques such as rolling forming process and grain textured microstructure can further enhance breakdown strength. Strain actuation properties can be improved by achieving an optimum level of ergodicity, which leads to sprout-like S-E loops with large strain (over 0.4%). This can be obtained in single phase materials with specific compositions, in relaxor composites realized by appropriate additions of non-ergodic phase seeds into an ergodic relaxor matrix, and in ceramics with appropriate grain texture. Electrocaloric properties increase near the temperature range of critical points, in compounds with the presence of polar/weakly-polar MPBs and in high-entropy compositions, which is one of the latest strategies reported. Photoluminescence properties can be increased by rare earth additions in BNT-based materials, and reversible changes can be obtained in the ergodic relaxor state.

## 7. Outlook

Despite great progress has been made on understanding the behaviour of BNT-based materials, there are still considerable challenges lying ahead, mainly related to the achievement of reproducible properties and the development of mass-scale production routes. In order to exploit the commercialization of BNT-based products, it would be opportune to systematically investigate the influence of all relevant processing variables to outline standard processing recipes that would ensure reliability of structures, microstructures and properties. More conclusive agreements on average and local structures can be reached by relying on reproducible samples and combining various investigative techniques, including advanced diffraction, high-resolution microscopy and spectroscopic techniques. Further insights into the mechanisms of electric field-induced transformations could be obtained by increasing the use of *in-situ* experiments for real-time observations of structural and microstructural evolution during the application of external electric fields. Systematic *in-situ* studies focused on the effects of composition should be carried out to better understand how to control the kinetics of EFITs and how to further tailor their macroscopic effects through refined compositional design criteria. The possibility of developing BNT-based materials undergoing multiple EFITs recently detected in lead-based systems should be further explored, as an interesting avenue to attain improved energy density and strain actuation properties. The validity of the polarization mismatch approach should be verified and further rationalized for similar purposes. A better synergy between experimental research and theoretical approaches shall be established to improve the current capabilities in predicting field-induced variations of key properties and their complex dependence on structural and microstructural features, including domain structure and grain morphology. In order to reliably evaluate the effects of EFITs on relevant properties, standard testing protocols are needed to ensure that the experiments are consistently run and that the results are correctly interpreted.

As future perspectives for EFITs, it can be envisaged that the scientific interest on EFITs will further increase, also due to their potential in controlling multifunctional properties, including electrical transport and magnetoelectric behaviour, as reported in recent studies. It has been found that electric field-induced transformations allow modulating chemical, electronic, magnetic and optical properties of SrIrO<sub>3</sub>/La<sub>0.2</sub>Sr<sub>0.8</sub>MnO<sub>3</sub> superlattices, by voltage-driven transfers of ions [324]. Additionally, it has been noticed that

electric fields can advantageously tune defect complexes in various systems (see Ref. [325] and references therein), and can induce local stoichiometry modifications that enable controlled changes of magnetic functionalities, as recently observed in  $\text{SrCo}_{1-x}\text{Fe}_x\text{O}_{3-6}$  thin films [326]. These studies provide broader perspectives on the exploitation of EFITs for the development of multifunctional electronic and spintronic devices in novel high-tech applications.

### Declaration of Competing Interest

The authors declare that they have no known competing financial interests or personal relationships that could have appeared to influence the work reported in this paper.

### Acknowledgements

Authors thank for the financial support by EPSRC, MASSIVE Project No. EP/L017695/1. The Royal Society is thanked for a Newton Advanced Fellowship award (NAF\R\201126). V. Koval acknowledges the Grant Agency of the Slovak Academy of Sciences (Grant No. 2/0038/20).

### References

- [1] Franzbach D. Field Induced Phase Transitions in Ferroelectric Materials. Doctoral dissertation. Technical University of Darmstadt; 2013.
- [2] Acosta M, Novak N, Rojas V, Patel S, Vaish R, Koruza J, et al. BaTiO<sub>3</sub>-based piezoelectrics: fundamentals, current status, and perspectives. *Appl Phys Rev* 2017; 4:41305.
- [3] Bao Q, Zhang H, Pan C. Electric-field-induced microstructural transformation of carbon nanotubes. *Appl Phys Lett* 2006;89:063124.
- [4] You JW, Bongu SR, Bao Q, Panoui NC. Nonlinear optical properties and applications of 2D materials: theoretical and experimental aspects. *Nanophotonics* 2019;8(1):63–97.
- [5] Yadlovker D, Berger S. Reversible electric field induced nonferroelectric to ferroelectric phase transition in single crystal nanorods of potassium nitrate. *Appl Phys Lett* 2007;91:173104.
- [6] Panciera F, Norton MM, Alam SB, Hofmann S, Molhave K, Ross FM. Controlling Nanowire Growth Through Electric Field-Induced Deformation of the Catalyst Droplet. *Nat Commun* 2016;7:12271.
- [7] Li Z, Wang Y, Tian G, Li P, Zhao L, Zhang F, et al. High-density array of ferroelectric nanodots with robust and reversibly switchable topological domain states. *Sci Adv* 2017;3:e1700919.
- [8] Lipovskii A, Melekhin V, Petrov M, Svirko Y, Zhurikhina V. Bleaching versus poling: comparison of electric field induced phenomena in glasses and glass-metal nanocomposites. *Appl Phys Rev* 2011;109:011101.
- [9] McLaren C, Heffner W, Tessarollo R, Raj R, Jain H. Electric field-induced softening of alkali silicate glasses. *Appl Phys Lett* 2015;107:184101.
- [10] Andrienko D. Introduction to liquid crystals. *J Mol Liq* 2018;267:520–41.
- [11] Hirotsu S. Electric-field-induced phase transition in polymer gels. *Jpn J Appl Phys* 1985;24:388–96.
- [12] Bruggeman PJ, Kushner MJ, Locke BR, Gardeniens JGE, Graham WG, Graves DB, et al. Plasma-liquid interactions: a review and roadmap. *Plasma Sources Sci Technol* 2016;25(5):053002.
- [13] Tao R. Electric-field-induced phase transition in electrorheological fluids. *Phys Rev E* 1993;47:423–6.
- [14] Mhatre S, Vivacqua V, Ghadiri M, Abdullah AM, Al-Marri MJ, Hassanpour A, et al. Electrostatic phase separation: a review. *Chem Eng Res Des* 2015;96: 177–95.
- [15] Swan JW, Vasquez PA, Whitson PA, Fincke EM, Wakata K, Magnus SH, et al. Multi-scale kinetics of a field-directed colloidal phase transition. *PNAS* 2012;109 (40):16023–8.
- [16] Beebe SJ. Bioelectrics in basic science and medicine: impact of electric fields on cellular structures and functions. *Journal of Nanomedicine and Nanotechnology* 2013;4(2):163–70.
- [17] Adrjanowicz K, Paluch M, Richert R. Formation of new polymorphs and control of crystallization in molecular glass-formers by electric field. *PCCP* 2018;20: 925–31.
- [18] Alexander LF, Radacsi N. Application of electric fields for controlling crystallization. *Cryst Eng Comm* 2019;21:5014–31.
- [19] Amundson K, Helfand E, Quan X, Smith SD. Alignment of lamellar block copolymer microstructure in an electric field. 1. Alignment kinetics. *Macromolecules* 1993;26(11):2698–703.
- [20] Amundson K, Helfand E, Quan X, Smith SD. Alignment of lamellar block copolymer microstructure in an electric field. 2. Mechanisms of alignment. *Macromolecules* 1994;27(22):6559–70.
- [21] Niksiar P, Su FY, Frank MB, Ogdan TA, Naleway SE, Meyers MA, et al. External Field Assisted Freeze Casting Ceramics 2019;2:208–34.
- [22] Hammadi Z, Velesler S. New approaches on crystallization under electric fields. *Progr Biophys Mol Biol* 2009;101:38–44.
- [23] Edwards AMJ, Brown CV, Newton MI, Mchale G. Dielectrowetting: The Past, Present and Future. *Curr Opin Colloid Interface Sci* 2018;36:28–36.
- [24] Hao X. A review on the dielectric materials for high energy-storage application. *Journal Advanced Dielectrics* 2013;3(1):1330001.
- [25] Li F, Zhai J, Shen B, Zeng H. Recent progress of ecofriendly perovskite-type dielectric ceramics for energy storage applications. *Journal Advanced Dielectrics* 2018;8:1830005.
- [26] Yang L, Kong X, Li F. Perovskite lead-free dielectrics for energy storage applications. *Prog Mater Sci* 2019;102:72–108.
- [27] Jo W, Dittmer R, Acosta M, Zang J, Groh C, Sapper E, et al. Giant electric-field-induced strains in lead-free ceramics for actuator applications-status and perspective. *J Electroceram* 2012;29(1):71–93.
- [28] Ahn CW, Hong CH, Choi BY, Kim HP, Han HS, Hwang Y, et al. A brief review on relaxor ferroelectrics and selected issues in lead-free relaxors. *J Korean Phys Soc* 2016;68:1481–94.
- [29] Hao J, Li W, Zhai J, Chen H. Progress in high-strain perovskite piezoelectric ceramics. *Mater Sci Eng R* 2019;135:1–57.
- [30] Suchanek G, Pakhomov O, Gerlach, G. Refrigeration-electrocaloric cooling. Rijeka: InTech; 2017. p. 19–43.
- [31] Dissado LA. "Dielectric Response" in *Springer Handbook of Electronic and Photonic Materials*, Wurzburg: Springer-Science, vol. XXXII; 2017. p. 219–244.
- [32] Damjanovic D. Ferroelectric, dielectric and piezoelectric properties of ferroelectric thin films and ceramics. *Rep Prog Phys* 1998;61:1267–324.
- [33] Kleemann W. Random fields in relaxor ferroelectrics-a jubilee review. *Journal of Advanced Dielectrics* 2012;2(2):1241001.
- [34] Kong LB, Li S, Zhang TS, Zhai JW, Boey FYC, Ma J. Electrically tunable dielectric materials and strategies to improve their performances. *Prog Mater Sci* 2010; 55:840–93.
- [35] Liu YK, Yin YW, Li XG. Colossal Magnetoresistance in Manganites and Related Prototype Devices. *Chin Phys B* 2013;22(8):087502.
- [36] Ortega N, Kumar A, Scott JF, Katiyar RS. Multifunctional magnetoelectric materials for device applications. *J Phys: Condens Matter* 2015;27:504002.
- [37] Guo H, Liu X, Xue F, Chen L, Hong W, Tan X. Disrupting long-range polar order with an electric field. *Phys Rev B* 2016;93:174114.
- [38] Ghosh D, Akito S, Jared C, Thomas PA, Han H, Nino JC, et al. Domain wall displacement is the origin of superior permittivity and piezoelectricity in BaTiO<sub>3</sub> at intermediate grain sizes. *Adv Funct Mater* 2014;24(7):885–96.

- [39] Kalyani AK, Krishnan H, Sen A, Senyshyn A, Ranjan R. Metastable monoclinic and orthorhombic phases and electric field induced irreversible phase transformation at room temperature in the lead-free classical ferroelectric BaTiO<sub>3</sub>. *Phys Rev B* 2015;91:104104.
- [40] Brajesh K, Abebe M, Ranjan R. Structural transformations in morphotropic-phase-boundary composition of the lead-free piezoelectric system Ba(Ti<sub>0.8</sub>Zr<sub>0.2</sub>)O<sub>3</sub>-(Ba<sub>0.7</sub>Ca<sub>0.3</sub>)TiO<sub>3</sub>. *Phys Rev B* 2016;94(104108).
- [41] Jo W, Daniels JE, Jones JL, Tan X, Thomas PA, Damjanovic D, et al. Evolving morphotropic phase boundary in lead-free (Bi<sub>1/2</sub>Na<sub>1/2</sub>)TiO<sub>3</sub>-BaTiO<sub>3</sub> piezoceramics. *Journal of Appl Phys* 2011;109:014110.
- [42] Tan X, Ma C, Frederick J, Beckman S, Webber KG. The antiferroelectric↔ferroelectric phase transition in lead-containing and lead-free perovskite ceramics. *J Am Ceram Soc* 2011;94(12):4091–107.
- [43] Tian Y, Jin L, Zhang HF, Xu Z, Wei XY, Politova ED, et al. High energy density in silver niobate ceramics. *J Mater Chem A* 2016;4:17279–87.
- [44] Tian Y, Jin L, Zhang HF, Xu Z, Wei XY, Viola G, et al. Phase transitions in bismuth-modified silver niobate ceramics for high power energy storage. *J Mater Chem A* 2017;5:17525–31.
- [45] Tian Y, Jin Li HuQ, Yu K, Zhuang Y, Viola G, et al. Phase transitions in tantalum-modified silver niobate ceramics for high power energy storage. *J Mater Chem A* 2019;7(2):834–42.
- [46] Zhao L, Liu Q, Gao J, Zhang S, Li JF. Lead-free antiferroelectric silver niobate tantalate with high energy storage performance. *Adv Mater* 2017;29:1701824.
- [47] Zhao L, Gao J, Qing L, Zhang S, Li JF. Silver Niobate Lead-Free Antiferroelectric Ceramics: Enhancing Energy Storage Density by B-Site Doping. *ACS Appl Mater Interfaces* 2018;10(1):819–26.
- [48] Yang D, Gao J, Shu L, Liu YX, Yu J, Zhang Y, et al. Lead-free antiferroelectric niobates AgNbO<sub>3</sub> and NaNbO<sub>3</sub> for energy storage applications. *J Mater Chem A* 2020;8:23724–37.
- [49] Walker J, Bryant P, Kurusingal V, Sorrell C, Kuscer D, Drazic G, et al. Synthesis-phase-composition relationship and high electric-field-induced electromechanical behavior of samarium-modified BiFeO<sub>3</sub> ceramics. *Acta Mater* 2015;83:149–59.
- [50] Walker J, Simons H, Alikin D, Turygin AP, Shur VY, Kholkin AL, et al. Dual strain mechanisms in a lead-free morphotropic phase boundary ferroelectric. *Sci Rep* 2016;6:19630.
- [51] Walker J, Ursic H, Bencan A, Malic B, Simons H, Reaney I, et al. Temperature dependent piezoelectric response and strain-electric-field hysteresis of rare-earth modified bismuth ferrite ceramics. *J Mater Chem C* 2016;4:7859.
- [52] Smolenskii GA, Isupov VA, Agranovskaya AI, Krainik NN. New ferroelectrics of complex composition IV. *Sov Phys Solid State* 1961;2:2651–4.
- [53] Takenaka T, Maruyama K, Sakata K. (Bi<sub>1/2</sub>Na<sub>1/2</sub>)TiO<sub>3</sub>-BaTiO<sub>3</sub> System for Lead-Free Piezoelectric Ceramics. *Jpn J Appl Phys* 1991;30:2236–9.
- [54] Rodel J, Jo W, Seifert KTP, Anton EM, Granzow T, Damjanovic D. Perspective on the Development of Lead-Free Piezoceramics. *J Am Ceram Soc* 2009;92:1153–77.
- [55] Uchida K, Kikuchi T. Subsolidus Phase Equilibria in the System Na<sub>2</sub>O-Bi<sub>2</sub>O<sub>3</sub>-TiO<sub>2</sub> at 1000°C. *J Am Ceram Soc* 1978;61(1–2):5–8.
- [56] Spreitzer M, Valant M, Suvorov D. Sodium deficiency in Na<sub>0.5</sub>Bi<sub>0.5</sub>TiO<sub>3</sub>. *J Mater Chem* 2007;17:185–92.
- [57] Kim CY, Sekino T, Niihara K. Synthesis of Bismuth Sodium Titanate Nanosized Powders by Solution/Sol–Gel Process. *J Am Ceram Soc* 2003;86(9):1464–7.
- [58] Kim CY, Sekino T, Yamamoto Y, Niihara K. The Synthesis of Lead-Free Ferroelectric Bi<sub>1/2</sub>Na<sub>1/2</sub>TiO<sub>3</sub> Thin Film by Solution-Sol–Gel Method. *J Sol-Gel Sci Technol* 2005;33:307–14.
- [59] Kanie K, Sakai H, Tani J, Takahashi H, Muramatsu A. Synthesis of Bismuth Sodium Titanate Fine Particles with Different Shapes by the Gel-Sol Method. *Mater Trans* 2007;48:2174–8.
- [60] Zhang H, Jiang S, Kajiyoshi K. Preparation and characterization of sol–gel derived sodium–potassium bismuth titanate powders and thick films deposited by screen printing. *J Alloy Compd* 2010;495(1):173–80.
- [61] Halim NA, Velayutham TS, Abd. Majid WH. Pyroelectric, ferroelectric, piezoelectric and dielectric properties of Na<sub>0.5</sub>Bi<sub>0.5</sub>TiO<sub>3</sub> ceramic prepared by sol-gel method. *Ceram Int* 2016;42(14):15664–70.
- [62] Zhang J, Hao S, Fu D, Mi N, Wang F. Preparation of pure and Sm-doped Na<sub>0.5</sub>Bi<sub>0.5</sub>TiO<sub>3</sub> nanosized powders by sol–gel method and their electrical properties. *Res Chem Intermed* 2016;42:963–75.
- [63] Christensen M, Einarsrud MA, Grande T. Fabrication of Lead-Free Bi<sub>0.5</sub>Na<sub>0.5</sub>TiO<sub>3</sub> Thin Films by Aqueous Chemical Solution Deposition. *Materials* 2017;10(2):213.
- [64] Pookmanee P, Rujijanagul G, Ananta S, Heilmann RB, Phanichphant S. Effect of sintering temperature on microstructure of hydrothermally prepared bismuth sodium titanate ceramics. *J Eur Ceram Soc* 2002;24(2):517–20.
- [65] Ma X, Zhang W, Xue L, Yin S, Wan L, Yan Y. Hydrothermal synthesis of bismuth sodium titanate particles with different morphologies. *J Mater Sci* 2013;48:6878–84.
- [66] Zhang XL, Tang WP, Wu HY, Zhang BB, Zheng XC. Effect of hydrothermal temperatures on the structure of Bi<sub>0.5</sub>Na<sub>0.5</sub>TiO<sub>3</sub> nanomaterials. *Adv Mater Res* 2012;482–484:2573–6.
- [67] Hao J, Wang X, Chen R, Li L. Synthesis of (Bi<sub>0.5</sub>Na<sub>0.5</sub>)TiO<sub>3</sub> nanocrystalline powders by stearic acid gel method. *Mater Chem Phys* 2005;90(2–3):282–5.
- [68] Ma X, Xue L, Wan L, Yin S, Zhou Q, Yan Y. Synthesis, sintering, and characterization of BNT perovskite powders prepared by the solution combustion method. *Ceram Int* 2013;39:8147–52.
- [69] Cilaveni G, Ashok Kumar KV, Raavi SSK, Subrahmanyam C, Athana S. Control over relaxor, piezo-photocatalytic and energy storage properties in Na<sub>0.5</sub>Bi<sub>0.5</sub>TiO<sub>3</sub> via processing methodologies. *J Alloy Compd* 2019;798:540–52.
- [70] Li M, Zhang H, Cook SN, Li L, Kilner JA, Reaney IM, et al. Dramatic Influence of A-Site Nonstoichiometry on the Electrical Conductivity and Conduction Mechanisms in the Perovskite Oxide Na<sub>0.5</sub>Bi<sub>0.5</sub>TiO<sub>3</sub>. *Chem Mater* 2015;27(2):629–34.
- [71] Mahajan A, Zhang H, Wu J, Ramana EV, Yu C, Tarakina NV, et al. Effect of processing on the structures and properties of bismuth sodium titanate compounds. DOI: 10.1557/s43578-020-00040-1.
- [72] Park SE, Chung ITK, Hong KS. Nonstoichiometry and the Long-Range Cation Ordering in Crystals of (Na<sub>1/2</sub>Bi<sub>1/2</sub>)TiO<sub>3</sub>. *J Am Ceram Soc* 1994;77(10):2641–7.
- [73] Spreitzer M. The synthesis of Na<sub>0.5</sub>Bi<sub>0.5</sub>TiO<sub>3</sub> ceramics. *Materiali in tehnologije* 2004;38(6):313–6.
- [74] Li M, Pietrowski MJ, De Souza RA, Zhang H, Reaney IM, Cook SN, et al. A family of oxide ion conductors based on the ferroelectric perovskite Na<sub>0.5</sub>Bi<sub>0.5</sub>TiO<sub>3</sub>. *Nat Mater* 2014;13:31–5.
- [75] Naderer M, Schütz D, Kainz T, Reichmann K, Mittermayr F. The formation of secondary phases in Bi<sub>0.5</sub>Na<sub>0.375</sub>K<sub>0.125</sub>TiO<sub>3</sub> ceramics. *J Eur Ceram Soc* 2012;32(10):2399–404.
- [76] Mishra A, Khatua DK, De A, Ranjan R. Off-stoichiometry, structural-polar disorder and piezoelectricity enhancement in pre-MPB lead-free Na<sub>0.5</sub>Bi<sub>0.5</sub>TiO<sub>3</sub>-BaTiO<sub>3</sub> piezoceramic. *J Appl Phys* 2019;125:214101.
- [77] Jeong IK, Sung Y, Song T, Kim MH, Llobet A. Structural evolution of bismuth sodium titanate induced by A-site non-stoichiometry: Neutron powder diffraction studies. *J Korean Phys Soc* 2015;67(9):1583–7.
- [78] Sung YS, Kim JM, Cho JH, Song TK, Kim MH, Chong HH, et al. Effects of Na nonstoichiometry in Bi<sub>0.5</sub>Na(0.5+x)TiO<sub>3</sub> ceramics. *Appl Phys Lett* 2010;96:022901.
- [79] Sung YS, Kim JM, Cho JH, Song TK, Kim MH, Park TG. Effects of Bi nonstoichiometry in (Bi<sub>0.5</sub>+xNa)TiO<sub>3</sub> ceramics. *Appl Phys Lett* 2011;98(1):012902.
- [80] Yang F, Li M, Li L, Wu P, Pradal-Velázquez E, Sinclair DC. Defect chemistry and electrical properties of sodium bismuth titanate perovskite. *J Mater Chem A* 2018;6(13):5243–54.
- [81] Sung YS, Kim MH. In: Nonstoichiometry in (Bi<sub>0.5</sub>Na<sub>0.5</sub>)TiO<sub>3</sub> Ceramics. Chapter 12 in “Lead-free Piezoelectrics”. New York: Springer; 2012. p. 353–70.
- [82] Hiruma Y, Nagata H, Takenaka T. Thermal depoling process and piezoelectric properties of bismuth sodium titanate ceramics. *J Appl Phys* 2009;105(8):084112.
- [83] Naderer M, Kainz T, Schütz D, Reichmann K. The influence of Ti-nonstoichiometry in Bi<sub>0.5</sub>Na<sub>0.5</sub>TiO<sub>3</sub>. *J Eur Ceram Soc* 2014;34(3):663–7.
- [84] Reichmann K, Feteira A, Li M. Bismuth sodium titanate based materials for piezoelectric actuators. *Materials* 2015;8(12):8467–95.
- [85] Shibata K, Wang R, Tou T, Koruza J. Applications of lead-free piezoelectric materials. *MRS Bull* 2018;43(8):612–6.

- [86] Rödel J, Webber KG, Dittmer R, Jo W, Kimura M, Damjanovic D. Transferring lead-free piezoelectric ceramics into application. *J Eur Ceram Soc* 2015;35(6):1659–81.
- [87] Koruza J, Bell AJ, Frömling T, Webber KG, Wang K, Rödel J. Requirements for the transfer of lead-free piezoceramics into application. *J Materomics* 2018;4(1):13–26.
- [88] Smolenskii GA, Isupov VA, Agranovskaya AI, Popov SN. Ferroelectrics with diffuse phase transitions. *Sov Phys Solid State* 1961;2:2584–94.
- [89] Bührer CF. Some Properties of Bismuth Perovskites. *J Chem Phys* 1962;36:798–803.
- [90] Ivanova V, Kapyshev A, Venetsev YN, Zhdanov G. X-ray determination of the symmetry of elementary cells of the ferroelectric materials  $(K_{0.5}Bi_{0.5})TiO_3$  and  $(Na_{0.5}Bi_{0.5})TiO_3$  and of high-temperature phase transitions in  $(K_{0.5}Bi_{0.5})TiO_3$ . *Izv Akad Nauk SSSR Seriya Fiz* 1962;26:354–6.
- [91] Zvirgzds JA, Kapostin PP, Zvirgzde JV, Kruzina TV. X-ray study of phase transitions in ferroelectric  $Na_{0.5}Bi_{0.5}TiO_3$ . *Ferroelectrics* 1982;40:75–7.
- [92] Vakhrushev S, Ivanitskij B, Kvyatkovskij B, Majstrenko A, Malysheva R, Okuneva N, et al. Neutron-diffraction study on sodium-bismuth titanate. *Sov Phys Solid State* 1983;25:1504–6.
- [93] Jones GO, Thomas PA. Investigation of the structure and phase transitions in the novel A-site substituted distorted perovskite compound  $Na_{0.5}Bi_{0.5}TiO_3$ . *Acta Crystallogr Sect B* 2002;58:168–78.
- [94] Jones GO, Kreisel J, Thomas PA. A Structural Study of the  $(Na_{1-x}K_x)_{0.5}Bi_{0.5}TiO_3$  Perovskite Series as a Function of Substitution (x) and Temperature. *Powder Diffr* 2002;17(4):301–19.
- [95] Isuyov VA, Pronin IP, Kruzina TV. Temperature dependence of biringence and opalescence of the sodium-bismuth titanate crystals. *Ferroelectr Lett Sect* 1984;2:205–8.
- [96] Aleksandrova IP, Sukhovskiy AA, Ivanov YN, Yablonskaya YE, Vakhrushev SB.  $^{23}Na$  NMR study of the local order in the  $Na_{1/2}Bi_{1/2}TiO_3$  structure in a weak magnetic field. *Phys Solid State* 2008;50(3):496–501.
- [97] Gorfman S, Thomas PA. Evidence for a non-rhombohedral average structure in the lead-free piezoelectric material  $Na_{0.5}Bi_{0.5}TiO_3$ . *J Appl Crystallogr* 2010;43:1409–14.
- [98] Aksel E, Forrester JS, Jones JL, Thomas PA, Page K, Suchomel MR. Monoclinic crystal structure of polycrystalline  $Na_{0.5}Bi_{0.5}TiO_3$ . *Appl Phys Lett* 2011;98:152901.
- [99] Rao BN, Ranjan R. Electric-field-driven monoclinic-to-rhombohedral transformation in  $Na_{1/2}Bi_{1/2}TiO_3$ . *Phys Rev B* 2012;86:134103.
- [100] Ma C, Guo H, Tan X. A new phase boundary in  $(Bi_{1/2}Na_{1/2})TiO_3$ – $BaTiO_3$  revealed via a novel method of electron diffraction analysis. *Adv Funct Mater* 2013;23:5261–6.
- [101] Aksel E, Forrester JS, Kowalski B, Jones JL, Thomas PA. Phase transition sequence in sodium bismuth titanate observed using high-resolution X-ray diffraction. *Appl Phys Lett* 2011;99:222901.
- [102] Rao BN, Fitch AN, Ranjan R. Ferroelectric-ferroelectric phase coexistence in  $Na_{1/2}Bi_{1/2}TiO_3$ . *Phys Rev B* 2013;87:060102.
- [103] Zhou C, Zhang Y, Wang Y, Li Q, Xu J, Chen G, et al. An intermediate metastable ferroelectric state induced giant functional responses in  $Bi_{0.5}Na_{0.5}TiO_3$  ceramics. *J Mater Chem C* 2019;7:8255–60.
- [104] Gorfman S, Glazer AM, Noguchi Y, Miyayama M, Luo H, Thomas PA. Observation of a low-symmetry phase in  $Na_{0.5}Bi_{0.5}TiO_3$  crystals by optical birefringence microscopy. *J Appl Crystallogr* 2012;45:444–52.
- [105] Pan J, Niranjan MK, Waghmare UV. Aliovalent cation ordering, coexisting ferroelectric structures, and electric field induced phase transformation in lead-free ferroelectric  $Na_{0.5}Bi_{0.5}TiO_3$ . *J Appl Phys* 2016;119:124102.
- [106] Mohanty HS, Dam T, Borkar H, Pradhan DK, Mishra KK, et al. Structural transformations and physical properties of  $(1-x)Na_{0.5}Bi_{0.5}TiO_3$ – $xBaTiO_3$  solid solutions near a morphotropic phase boundary. *J Phys: Condens Matter* 2019;31:075401.
- [107] Kreisel J, Glazer AM, Jones GO, Thomas PA, Abello L, Lucazeau G. An x-ray diffraction and Raman spectroscopy investigation of A-site substituted perovskite compounds: the  $(Na_{1-x}K_x)_{0.5}Bi_{0.5}TiO_3$  ( $0 < x < 1$ ) solid solution. *J Phys: Condens Matter* 2000;12:3267–80.
- [108] Siny IG, Husson E, Beny JM, Lushnikov SG, Rogacheva EA, Syrnikov PP. Raman scattering in the relaxor-type ferroelectric  $Na_{1/2}Bi_{1/2}TiO_3$ . *Ferroelectrics* 2000;248(14):57–78.
- [109] Kreisel J, Bouvier P, Dkhil B, Thomas PA, Glazer AM, Welberry TR, et al. High-pressure X-ray scattering of oxides with a nanoscale local structure: Application to  $Na_{1/2}Bi_{1/2}TiO_3$ . *Phys Rev B* 2003;68:014113.
- [110] Luo H, Ke H, Zhang H, Zhang L, Li F, Cao L, et al. Bi-fluctuation in  $Na_{0.5}Bi_{0.5}TiO_3$  Ferroelectric Ceramics with Abnormal Relaxor Behaviour. *Phil Mag* 2019;99(21):2661.
- [111] Burton BP, Cockayne E. Unexpected ground state structures in relaxor ferroelectrics. *Ferroelectrics* 2002;270:173–8.
- [112] Dorcet V, Trolliard G. A transmission electron microscopy study of the A-site disordered perovskite  $Na_{0.5}Bi_{0.5}TiO_3$ . *Acta Mater* 2008;56:1753–61.
- [113] Beanland R, Thomas PA. Imaging planar tetragonal sheets in rhombohedral  $Na_{0.5}Bi_{0.5}TiO_3$  using transmission electron microscopy. *Scr Mater* 2011;65:440–3.
- [114] Levin I, Reaney IM. Nano- and mesoscale structure of  $Na_{1/2}Bi_{1/2}TiO_3$ : A TEM perspective. *Adv Funct Mater* 2012;22:3445–52.
- [115] Groszewicz PB, Grötting M, Breitzke H, Jo W, Albe K, Buntkowsky G, et al. Reconciling Local Structural Disorder and the Relaxor State in  $(Bi_{1/2}Na_{1/2})TiO_3$ – $BaTiO_3$ . *Sci Rep* 2016;6:31739.
- [116] Ge W, Devreugd CP, Phelan D, Zhang Q, Ahart M, Li J, et al. Lead-free and lead-based  $ABO_3$  perovskite relaxors with mixed-valence A-site and B-site disorder: comparative neutron scattering structural study of  $(Na_{1/2}Bi_{1/2})TiO_3$  and  $Pb(Mg_{1/3}Nb_{2/3})O_3$ . *Phys Rev B* 2013;88:174115.
- [117] Aksel E, Forrester JS, Nino JC, Page K, Shoemaker DP, Jones JL. Local atomic structure deviation from average structure of  $Na_{0.5}Bi_{0.5}TiO_3$ : Combined X-ray and neutron total scattering study. *Phys Rev B* 2013;87:104113.
- [118] Keeble DS, Barney ER, Keen DA, Tucker MG, Kreisel J, Thomas PA. Bifurcated polarization rotation in bismuth-based piezoelectrics. *Adv Funct Mater* 2012;23:185–90.
- [119] Rao BN, Datta R, Chandrashekar SS, Mishra DK, Sathe V, Senyshyn A, et al. Local structural disorder and its influence on the average global structure and polar properties in  $Na_{0.5}Bi_{0.5}TiO_3$ . *Phys Rev B* 2013;88:224103.
- [120] Beanland R, Thomas PA. Symmetry and defects in rhombohedral single-crystalline  $Na_{0.5}Bi_{0.5}TiO_3$ . *Phys Rev B* 2014;89:174102.
- [121] Kreisel J, Glazer AM, Bouvier P, Lucazeau G. High-pressure Raman study of a relaxor ferroelectric: the  $Na_{0.5}Bi_{0.5}TiO_3$  perovskite. *Phys Rev B* 2001;63:174106.
- [122] Rao BN, Olivi L, Sathe V, Ranjan R. Electric field and temperature dependence of the local structural disorder in the lead-free ferroelectric  $Na_{0.5}Bi_{0.5}TiO_3$ : An EXAFS study. *Phys Rev B* 2016;93:024106.
- [123] Khatua DK, Mehrotra T, Mishra A, Majumdar B, Senyshyn A, Ranjan R. Anomalous influence of grain size on the global structure, ferroelectric and piezoelectric response of  $Na_{0.5}Bi_{0.5}TiO_3$ . *Acta Mater* 2017;134:177–87.
- [124] Yashima M. Size effect on the crystal structure of barium titanate nanoparticles. *J Appl Phys* 2005;98:014313.
- [125] Kong S, Kumar N, Checchia S, Cazorla C, Daniels J. Defect-Driven Structural Distortions at the Surface of Relaxor Ferroelectrics. *Adv Funct Mater* 2019;29(27):1900344.
- [126] Trolliard G, Dorcet V. Reinvestigation of phase transitions in  $Na_{0.5}Bi_{0.5}TiO_3$  by TEM. Part II: Second order orthorhombic to tetragonal phase transition. *Chem Mater* 2008;20:5074–82.
- [127] Vakhrushev S, Okuneva N, Plachenova E, Syrnikov P. Phase transitions in sodium-bismuth titanate. *JETP Lett* 1982;35:134–7.
- [128] Matsuura M, Iida H, Hirota K, Ohwada K, Noguchi Y, Miyayama M. Damped soft phonons and diffuse scattering in  $(Bi_{1/2}Na_{1/2})TiO_3$ . *Phys Rev B* 2013;87:06410.
- [129] Suchanicz J, Kwapulinski J. X-ray diffraction study of the phase transitions in  $Na_{0.5}Bi_{0.5}TiO_3$ . *Ferroelectrics* 1995;165:249–53.
- [130] Petzelt J, Kamba S, Fabry J, Noujni D, Porokhonskyy V, Pashkin A, et al. Infrared, Raman and High-Frequency Dielectric Spectroscopy and the Phase Transitions in  $Na_{1/2}Bi_{1/2}TiO_3$ . *J Phys: Condens Matter* 2004;16:2719–31.
- [131] Balagurov AM, Koroleva EY, Naberezhnov AA, Sakhnenko VP, Savenko BN, Ter-Oganessian NV, et al. The rhombohedral phase with incommensurate modulation in  $Na_{1/2}Bi_{1/2}TiO_3$ . *Phase Transitions* 2006;79(1–2):163–73.

- [132] Petzelt J, Nuzhnyy D, Bovtun V, Paściak M, Kamba S, Dittmer R, et al. Peculiar Bi-ion dynamics in  $\text{Na}_{0.5}\text{Bi}_{0.5}\text{TiO}_3$  from terahertz and microwave dielectric spectroscopy. *Phase Transitions* 2014;87:953–65.
- [133] Vakhrushev SB, Kvyatkovskii BE, Okuneva NM, Plachenova EL, Szymik PP. Soft mode and central peak in  $\text{Na}_0.5\text{Bi}_0.5\text{TiO}_3$ . *Fiz Tverd Tela (Leningrad)* 1983; 25: 2529 [Sov. Phys. Solid State 25, 1456 (1983)].
- [134] Isupov VA. Ferroelectric  $\text{Na}_{0.5}\text{Bi}_{0.5}\text{TiO}_3$  and  $\text{K}_{0.5}\text{Bi}_{0.5}\text{TiO}_3$ . *Perovskites and Their Solid Solutions*. *Ferroelectrics* 2005;315:123–47.
- [135] Jin YM, Wang YU, Khachatryan AG, Li JF, Viehland D. Adaptive ferroelectric states in systems with low domain wall energy: Tetragonal microdomains. *J Appl Phys* 2003;94:3629.
- [136] Adhikary GD, Khatua DK, Senyshyn A, Ranjan R. Random lattice strain and its relaxation towards the morphotropic phase boundary of  $\text{Na}_{0.5}\text{Bi}_{0.5}\text{TiO}_3$ -based piezoelectrics: impact on the structural and ferroelectric properties. *Phys Rev B* 2019;99:174112.
- [137] Karthik T, Radhakrishnan D, Narayana C. Nature of electric field driven ferroelectric phase transition in lead-free  $\text{Na}_{1/2}\text{Bi}_{1/2}\text{TiO}_3$ : in-situ temperature dependent ferroelectric hysteresis and Raman scattering studies. *J Alloy Compd* 2018;732:945–51.
- [138] Usher TM, Levin I, Daniels JE, Jones JL. Electric-Field Induced Local and Mesoscale Structural Changes in Polycrystalline Dielectrics and Ferroelectrics. *Sci Rep* 2015;5:14678.
- [139] Usher TM, Forrester JF, McDonnell M, Neufeind J, Page K, Peterson PF, et al. Time-of-flight neutron total scattering with applied electric fields: Ex situ and in situ studies of ferroelectric materials. *Rev Sci Instrum* 2018;89:092905.
- [140] Shvartsman VV, Lupascu DC. Lead-Free Relaxor Ferroelectrics. *J Am Ceram Soc* 2012;95:1–26.
- [141] Hong C-H, Kim H-P, Choi B-Y, Han H-S, Son JS, Ahn CW, et al. Lead-free piezoceramics where to move on? *J Materomics* 2016;2(1):1–24.
- [142] Zheng T, J.G. Wu JG, Xiao DQ, Zhu JG. Recent development in lead-free perovskite piezoelectric bulk materials. *Prog Mater Sci* 2018; 98: 552–624.
- [143] Paterson AR, Nagata H, Tan X, Daniels JE, Hinterstein M, Ranjan R, et al. Relaxor-ferroelectric transitions: Sodium bismuth titanate derivatives. *MRS Bull* 2018;43:600–6.
- [144] Ranjan R.  $\text{Na}_{1/2}\text{Bi}_{1/2}\text{TiO}_3$ -based lead-free piezoceramics: a review of structure-property correlation. *Curr Sci* 2020;118(10):1507.
- [145] Ma C, Tan X, Kleebe HJ. In situ transmission electron microscopy study on the phase transitions in lead-free  $(1-x)(\text{Bi}_{1/2}\text{Na}_{1/2})\text{TiO}_3-x\text{BaTiO}_3$  ceramics. *Journal of the American Ceramic Society* 2011; 94: (11) 4040–4.
- [146] Leontsev SO, Eitel RE. Progress in engineering high-strain lead-free piezoelectric ceramics. *Sci Technol Adv Mater* 2010;11:044302.
- [147] Liu LJ, Knapp M, Ehrenberg H, Fang L, Schmitt LA, Fuess H, et al. The phase diagram of  $\text{K}_{0.5}\text{Na}_{0.5}\text{NbO}_3\text{-Bi}_{1/2}\text{Na}_{1/2}\text{TiO}_3$ . *J Appl Crystallogr* 2016;49:574–84.
- [148] Rout D, Moon KS, Kang SJL, Kim IW. Dielectric and Raman Scattering Studies of Phase Transitions in the  $(100-x)\text{Na}_{0.5}\text{Bi}_{0.5}\text{TiO}_3-x\text{SrTiO}_3$  System. *J Appl Phys* 2010;108:084102.
- [149] Kim S, Choi H, Han S, Park JS, M.H. Lee MH, Song TK, Kim MH, Do D, Kim WJ. A correlation between piezoelectric response and crystallographic structural parameter observed in lead-free  $(1-x)(\text{Bi}_{0.5}\text{Na}_{0.5})\text{TiO}_3-x\text{SrTiO}_3$  piezoelectrics. *J Eur Ceram Soc* 2017; 37: 1379–86.
- [150] Bai W, Li L, Wang W, Shen B, Zhai J. Phase diagram and electrostrictive effect in BNT-based ceramics. *Solid State Commun* 2015;206:22–5.
- [151] Hao J, Shen B, Zhai J, Liu C, Li X, Gao X. Switching of morphotropic phase boundary and large strain response in lead-free ternary  $(\text{Bi}_{0.5}\text{Na}_{0.5})\text{TiO}_3\text{-}(\text{K}_{0.5}\text{Bi}_{0.5})\text{TiO}_3\text{-}(\text{K}_{0.5}\text{Na}_{0.5})\text{NbO}_3$  system. *J Appl Phys* 2013;113:114106.
- [152] Hiruma Y, Nagata H, Takenaka T. Formation of morphotropic phase boundary and electrical properties of  $(\text{Bi}_{1/2}\text{Na}_{1/2})\text{TiO}_3\text{-Ba}(\text{Al}_{1/2}\text{Nb}_{1/2})\text{O}_3$  solid solution ceramics. *Jpn J Appl Phys* 2009;48(9):8K–9K.
- [153] Daniels JE, Jo W, Rödel J, Rytz D, Donner W. Structural origins of relaxor behaviour in a  $0.96(\text{Bi}_{1/2}\text{Na}_{1/2})\text{TiO}_3\text{-}0.04\text{BaTiO}_3$  single crystal under electric field. *Appl Phys Lett* 2011;98:252904.
- [154] Ge W, Yao J, De Vreugd C, Li J, Viehland D, Zhang Q, et al. Electric field dependent phase stability and structurally bridging orthorhombic phase in  $\text{Na}_{0.5}\text{Bi}_{0.5}\text{TiO}_3\text{-}x\%\text{BaTiO}_3$  crystals near the MPB. *Solid State Commun* 2011;151(1):71–4.
- [155] Simons H, Daniels J, Jo W, Dittmer R, Studer A, Avdeev M, et al. Electric-field-induced strain mechanisms in lead-free  $94\%(\text{Bi}_{1/2}\text{Na}_{1/2})\text{TiO}_3\text{-}6\%\text{BaTiO}_3$ . *Appl Phys Lett* 2011;98(8):082901.
- [156] Daniels JE, Jo W, Rödel J, Jones JL. Electric-field-induced phase transformation at a lead-free morphotropic phase boundary: case study in a  $93\%(\text{Bi}_{0.5}\text{Na}_{0.5})\text{TiO}_3\text{-}7\%\text{BaTiO}_3$  piezoelectric ceramic. *Appl Phys Lett* 2009;95(3):032904.
- [157] Daniels JE, Jo W, Rödel J, Honkimäki V, Jones JL. Electric-field-induced phase-change behavior in  $(\text{Bi}_{0.5}\text{Na}_{0.5})\text{TiO}_3\text{-BaTiO}_3\text{-}(\text{K}_{0.5}\text{Na}_{0.5})\text{NbO}_3$ : a combinatorial investigation. *Acta Mater* 2010;58(6):2103–11.
- [158] Anthoniappan J, Lin CH, Tu CS, Chen PY, Chen CS, Chiu SJ, et al. Enhanced piezoelectric and dielectric responses in  $92.5\%(\text{Bi}_{0.5}\text{Na}_{0.5})\text{TiO}_3\text{-}7.5\%\text{BaTiO}_3$  ceramics. *J Am Ceram Soc* 2014;97(6):1890–4.
- [159] Yao Q, Wang F, Xu F, Leung CM, Wang T, Tang Y, et al. Electric field-induced giant strain and photoluminescence-enhancement effect in rare-earth modified lead-free piezoelectric ceramics. *ACS Appl Mater Inter* 2015;7(9):5066–75.
- [160] Fan Q, Zeng W, Zhou C, Cen Z, Yuan C, Xiao J, et al. Effect of reoriented nanodomains on crystal structure and piezoelectric properties of polycrystalline ferroelectric ceramics. *J Electron Mater* 2015;44:3843–8.
- [161] Yang L, Xu J, Li Q, Zeng W, Zhou CR, Yuan C, et al. High piezoelectricity associated with crossover from nonergodicity to ergodicity in modified  $\text{Bi}_{0.5}\text{Na}_{0.5}\text{TiO}_3$  relaxor ferroelectrics. *J Electroceram* 2016;37:23–8.
- [162] Xu J, Li Q, Zhou C, Zeng W, Xiao J, Ma J, et al. High Piezoelectric Response in  $(\text{Li}_{0.5}\text{Sm}_{0.5})^{2+}$ -Modified  $0.93\text{Bi}_{0.5}\text{Na}_{0.5}\text{TiO}_3\text{-}0.07\text{BaTiO}_3$  Near the Nonergodic-Ergodic Relaxor Transition. *J Electron Mater* 2016;45:2967–73.
- [163] Liu X, Guo H, Tan X. Evolution of structure and electrical properties with lanthanum content in  $[(\text{Bi}_{1/2}\text{Na}_{1/2})_{0.95}\text{Ba}_{0.05}]_{1-x}\text{La}_x\text{TiO}_3$  ceramics. *J Eur Ceram Soc* 2014;34(12):2997–3006.
- [164] Maqbool A, Hussain A, Malik RA, Rahman JU, Zaman A, Song TW, et al. Evolution of phase structure and giant strain at low driving fields in Bi-based lead-free incipient piezoelectrics. *Mater Sci Eng, B* 2015;109:105–12.
- [165] Bai W, Li P, Li L, Zhang J, Shen B, Zhai J. Structure evolution and large strain response in BNT-BT lead-free piezoceramics modified with  $\text{Bi}(\text{Ni}_{0.5}\text{Ti}_{0.5})\text{O}_3$ . *J Alloys Compd* 2015;649:772–81.
- [166] Jin CC, Wang FF, Wei LL, Tang J, Li Y, Yao QR, et al. Influence of B-site complex-ion substitution on the structure and electrical properties in  $\text{Bi}_{0.5}\text{Na}_{0.5}\text{TiO}_3$ -based lead-free solid solutions. *J Alloys Compd* 2014;585:185–91.
- [167] Hao J, Xu Z, Chu R, Li W, Fu P, Du J. Field-induced large strain in lead-free  $(\text{Bi}_{0.5}\text{Na}_{0.5})_{1-x}\text{Ba}_x\text{Ti}_{0.98}\text{Fe}_{0.02}\text{O}_3$  piezoelectric ceramics. *J Alloys Compd* 2016;677:96–104.
- [168] Hao J, Xu Z, Chu R, Li W, Du J, Li G. Ultrahigh strain response with fatigue-free behavior in  $(\text{Bi}_{0.5}\text{Na}_{0.5})\text{TiO}_3$ -based lead-free piezoelectric ceramics. *J Phys D Appl Phys* 2015;48(47):472001.
- [169] Bai W, Chen D, Huang Y, Shen B, Zhai J, Ji Z. Electromechanical properties and structure evolution in  $\text{BiAlO}_3$ -modified  $\text{Bi}_{0.5}\text{Na}_{0.5}\text{TiO}_3\text{-BaTiO}_3$  lead-free piezoceramics. *J Alloy Compd* 2016;667:6–17.
- [170] Chen C, Zhao X, Wang Y, Zhang H, Deng H, Li X, et al. Giant strain and electric-field-induced phase transition in lead-free  $(\text{Na}_{1/2}\text{Bi}_{1/2})\text{TiO}_3\text{-BaTiO}_3\text{-}(\text{K}_{1/2}\text{Na}_{1/2})\text{NbO}_3$  single crystal. *Appl Phys Lett* 2016;108(2):022903.
- [171] Hinterstein M, Knapp M, Holzel M, Jo W, Cervellino A, Ehrenberg H, et al. Field-induced phase transition in  $\text{Bi}_{1/2}\text{Na}_{1/2}\text{TiO}_3$ -based lead-free piezoelectric ceramics. *J Appl Crystallogr* 2010;43:1314–21.
- [172] Schmitt LA, Kleebe HJ. Single grains hosting two space groups—a transmission electron microscopy study of a lead-free ferroelectric. *Funct Mater Lett* 2010;03: 55–8.
- [173] Kling J, Tan X, Jo W, Kleebe H, Fuess H, Rödel J. In situ transmission electron microscopy of electric field-triggered reversible domain formation in Bi-based lead-free piezoceramics. *J Am Ceram Soc* 2010;93(9):2452–5.
- [174] Royles AJ, Bell AJ, Jephcoat AP, Kleppe AK, Milne SJ, Comyn TP. Electric-field-induced phase switching in the lead free piezoelectric potassium sodium bismuth titanate. *Appl Phys Lett* 2010;97:132909.

G. Viola et al.

- [175] Rao BN, Senyshyn A, Olivi L, Sathe V, Ranjan R. Maintaining local displacive disorders in  $\text{Na}_{0.5}\text{Bi}_{0.5}\text{TiO}_3$  piezoceramics by  $\text{K}_{0.5}\text{Bi}_{0.5}\text{TiO}_3$  substitution. *J Eur Ceram Soc* 2016;36:1961–72.
- [176] Dinh TH, Han HS, Lee JS, Ahn CW, Kim IW, Bafandeh MR. Ergodicity and nonergodicity in La-doped  $\text{Bi}_{1/2}(\text{Na}_{0.82}\text{K}_{0.18})_{1/2}\text{TiO}_3$  relaxors. *J Korean Phys Soc* 2015;66:1077–81.
- [177] Dinh TH, Bafandeh MR, Kang J, Hong C, Jo W, Lee J. Comparison of structural, ferroelectric, and strain properties between A-site donor and acceptor doped  $\text{Bi}_{1/2}(\text{Na}_{0.82}\text{K}_{0.18})_{1/2}\text{TiO}_3$  ceramics. *Ceram Int* 2015;41:S458–63.
- [178] Feng W, Wang X, Cen Z, Luo B, Zhao Q, Shen Z, et al. Enhancement of strain by electrically-induced phase transitions in BNKT-based ceramics. *J Alloy Compd* 2018;744:535–43.
- [179] Bai W, Chen D, Huang Y, Zheng P, Zhong J, Ding M, et al. Temperature-insensitive large strain response with a low hysteresis behavior in BNT-based ceramics. *Ceram Int* 2016;42(6):7669–80.
- [180] Ullah A, Malik RA, Ullah A, Lee DS, Jeong SJ, Lee JS, et al. Electric-field-induced phase transition and large strain in lead-free Nb-doped BNKT-BST ceramics. *J Eur Ceram Soc* 2014;34:29–35.
- [181] Ullah A, Ullah A, Kim I, Lee DS, Jeong SJ, Ahn CW. Large electromechanical response in lead-free La-doped BNKT-BST piezoelectric ceramics. *J Am Ceram Soc* 2014;97:2471–8.
- [182] Dittmer R, Gobeljic D, Jo W, Shvartsman VV, Lupascu DC, Jones JL, et al. Ergodicity reflected in macroscopic and microscopic field-dependent behavior of BNT-based relaxors. *J Appl Phys* 2014;115:084111.
- [183] Dittmer R, Jo W, Daniels J, Schaab S, Rödel J. Relaxor characteristics of morphotropic phase boundary  $(\text{Bi}_{1/2}\text{Na}_{1/2})\text{TiO}_3$ - $(\text{Bi}_{1/2}\text{K}_{1/2})\text{TiO}_3$  modified with  $\text{Bi}(\text{Zn}_{1/2}\text{Ti}_{1/2})\text{O}_3$ . *J Am Ceram Soc* 2011;94(12):4283–90.
- [184] Glaum J, Simons H, Hudspeth J, Acosta M, Daniels JE. Temperature dependent polarization reversal mechanism in  $0.94(\text{Bi}_{1/2}\text{Na}_{1/2})\text{TiO}_3$ - $0.06\text{Ba}(\text{Zr}_{0.02}\text{Ti}_{0.98})\text{O}_3$  relaxor ceramics. *Appl Phys Lett* 2015;107(23):232906.
- [185] Glaum J, Simons H, Acosta M, Hoffman M. Tailoring the piezoelectric and relaxor properties of  $(\text{Bi}_{1/2}\text{Na}_{1/2})\text{TiO}_3$ - $\text{BaTiO}_3$  via zirconium doping. *J Am Ceram Soc* 2013;96(9):2881–6.
- [186] Ma C, Tan X, Dul'kin E, Roth M. Domain structure-dielectric property relationship in lead-free  $(1-x)(\text{Bi}_{1/2}\text{Na}_{1/2})\text{TiO}_3$ - $x\text{BaTiO}_3$  ceramics. *J Appl Phys* 2010;108(10):104105.
- [187] Jo W, Schaab S, Sapper E, Schmitt LA, Kleebe H, Bell AJ, et al. On the phase identity and its thermal evolution of lead free  $(\text{Bi}_{1/2}\text{Na}_{1/2})\text{TiO}_3$ -6mol%  $\text{BaTiO}_3$ . *J Appl Phys* 2011;110(7):074106.
- [188] Li F, Chen G, Liu X, Zhai J, Shen B, Li S, et al. Type-I pseudo-first-order phase transition induced electrocaloric effect in lead-free  $\text{Bi}_{0.5}\text{Na}_{0.5}\text{TiO}_3$ - $0.06\text{BaTiO}_3$  ceramics. *Appl Phys Lett* 2017;110:182904.
- [189] Viehland D, Jang SJ, Cross LE, Wuttig M. Freezing of the polarization fluctuations in lead magnesium niobate relaxors. *J Appl Phys* 1990;68:2916.
- [190] Tagantsev AK. Vogel-Fulcher relationship for the dielectric permittivity of the relaxor ferroelectric. *Phys Rev Lett* 1994;72:1100.
- [191] Jo W, Daniels J, Damjanovic D, Kleemann W, Rödel J. Two-stage processes of electrically induced-ferroelectric to relaxor transition in  $0.94(\text{Bi}_{1/2}\text{Na}_{1/2})\text{TiO}_3$ - $0.06\text{BaTiO}_3$ . *Appl Phys Lett* 2013;102(19):192903.
- [192] Martin A, Khansur NH, Riess K, Webber KG. Frequency dependence of the relaxor-to-ferroelectric transition under applied electrical and mechanical fields. *J Eur Ceram Soc* 2019;39:1031–41.
- [193] Anton E, Jo W, Damjanovic D, Rödel J. Determination of depolarization temperature of  $(\text{Bi}_{1/2}\text{Na}_{1/2})\text{TiO}_3$ -based lead-free piezoceramics. *J Appl Phys* 2011;110:094108.
- [194] Peng P, Nie H, Cheng G, Liu Z, Wang G, Dong X. Thermal-induced structural transition and depolarization behavior in  $(\text{Bi}_{0.5}\text{Na}_{0.5})\text{TiO}_3$ - $\text{BiAlO}_3$  ceramics. *J Appl Phys* 2018;123:114102.
- [195] Schütz D, Deluca M, Krauss W, Feteira A, Jackson T, Reichmann K. Lone-pair-induced covalency as the cause of temperature-and field-induced instabilities in bismuth sodium titanate. *Adv Funct Mater* 2012;22:2285–94.
- [196] Glaum J, Heo Y, Acosta M, Sharma P, Seidel J, Hinterstein M. Revealing the role of local stress on the depolarization of BNT-BT-based relaxors. *Physical Review Materials* 2019;3:054406.
- [197] Chen S, Dong X, Zeng T, Zhang Y, Mao C. Thermal Depolarization and Ferroelectric Properties of  $(\text{Bi}_{0.5}\text{Na}_{0.5})_{1-x}\text{Ba}_x\text{TiO}_3$  Ceramics. *Ferroelectrics* 2008;363:199–208.
- [198] Davies M, Aksel E, Jones JL. Enhanced High-Temperature Piezoelectric Coefficients and Thermal Stability of Fe- and Mn-Substituted  $\text{Na}_{0.5}\text{Bi}_{0.5}\text{TiO}_3$  Ceramics. *J Am Ceram Soc* 2011;94(5):1314–6.
- [199] Zhang J, Pan Z, Guo FF, Liu WC, Ning H, Chen YB, et al. Semiconductor/relaxor 0–3 type composites without thermal depolarization in  $\text{Bi}_{0.5}\text{Na}_{0.5}\text{TiO}_3$ -based lead-free piezoceramics. *Nature Commun* 2015;6:6615.
- [200] Mahajan A, Zhang H, Wu J, Ramana EV, Reece MJ, Yan H. Effect of phase transitions on thermal depoling in lead-free  $0.94(\text{Bi}_{0.5}\text{Na}_{0.5}\text{TiO}_3)$ - $0.06(\text{BaTiO}_3)$  based piezoelectrics. *J Phys Chem C* 2017;121:5709–18.
- [201] Venkataraman LK, Zhu T, Salazar MP, Hofmann K, Waidha AI, Jaud JC, et al. Thermal depolarization and electromechanical hardening in  $\text{Zn}^{2+}$ -doped  $\text{Na}_{1/2}\text{Bi}_{1/2}\text{TiO}_3$ - $\text{BaTiO}_3$ . *J Am Ceram Soc* 2021;104:2201–12.
- [202] Khatua DK, Mishra A, Kumar N, Adhikary GD, Shankar U, Majumdar B, et al. A coupled microstructural-structural mechanism governing thermal depolarization delay in  $\text{Na}_{0.5}\text{Bi}_{0.5}\text{TiO}_3$ -based piezoelectrics. *Acta Mater* 2019;15:49–60.
- [203] Muramatsu H, Nagata H, Takenaka T. Quenching effects for piezoelectric properties on lead-free  $(\text{Bi}_{1/2}\text{Na}_{1/2})\text{TiO}_3$  ceramics. *Jpn J Appl Phys* 2016;55:10TB07.
- [204] Miura T, Nagata H, Takenaka T. Quenching effects on piezoelectric properties and depolarization temperatures of  $(\text{Bi}_{0.5}\text{Na}_{0.5})\text{TiO}_3$ -based solid solution systems. *Jpn J Appl Phys* 2017;56:10PD05.
- [205] Viola G, Ning H, Wei X, et al. Dielectric relaxation, lattice dynamics and polarization mechanisms in  $\text{Bi}_{0.5}\text{Na}_{0.5}\text{TiO}_3$ -based lead-free ceramics. *J Appl Phys* 2013;114:014107.
- [206] Viola G, Mckinnon R, Koval V, Adomkevicius A, Dunn S, Yan H. Lithium-induced phase transitions in lead-free  $\text{Bi}_{0.5}\text{Na}_{0.5}\text{TiO}_3$  based ceramics. *J Phys Chem C* 2014;118:8564–70.
- [207] Sapper E, Novak N, Jo W, Granzow T, Rödel J. Electric-field-temperature phase diagram of the ferroelectric relaxor system  $(1-x)\text{Bi}_{1/2}\text{Na}_{1/2}\text{TiO}_3$ - $x\text{BaTiO}_3$  doped with manganese. *J Appl Phys* 2014;115:194104.
- [208] Hong CH, Guo H, Tan X, Daniels JE, Jo W. Polarization reversal via a transient relaxor state in nonergodic relaxors near freezing temperature. *J Materiomics* 2019;5:634–40.
- [209] Yao Y, Sun Z, Ji Y, et al. Evolution of the tetragonal to rhombohedral transition in  $(1-x)(\text{Bi}_{1/2}\text{Na}_{1/2})\text{TiO}_3$ - $\text{BaTiO}_3$  ( $x < 7\%$ ). *Sci Tech Adv Mater* 2013;14:035008.
- [210] Cordero F, Craciun F, Trequatrini F, et al. Phase transitions and phase diagram of the ferroelectric perovskite  $(\text{Na}_{0.5}\text{Bi}_{0.5})_{1-x}\text{Ba}_x\text{TiO}_3$  by anelastic and dielectric measurements. *Phys Rev B* 2010;81:144124.
- [211] Young SE, Guo HZ, Ma C, Kessler MR, Tan X. Thermal analysis of phase transitions in perovskite electroceramics. *J Therm Anal Calorim* 2013;115:587–93.
- [212] Vögler M, Novak N, Schader FH, Rödel J. Temperature dependent volume fraction of polar nanoregions in lead-free  $(1-x)(\text{Bi}_{0.5}\text{Na}_{0.5})\text{TiO}_3$ - $x\text{BaTiO}_3$  ceramics. *Phys Rev B* 2017;95:024104.
- [213] Chong KB, Guiu F, Reece MJ. Thermal Activation of Ferroelectric Switching. *J Appl Phys* 2008;103(1):014101.
- [214] Zhou D, Wang R, Kamlah M. Determination of reversible and irreversible contributions to the polarization and strain response of soft PZT using the partial unloading method. *J Eur Ceram Soc* 2010;30:2603–15.
- [215] Dittmer R, Jo W, Aulbach E, Granzow T, Rödel J. Frequency-dependence of large-signal properties in lead-free piezoceramics. *J Appl Phys* 2012;112:014101.
- [216] Xu YH, Hong W, Feng YJ, Tan XL. Antiferroelectricity induced by electric field in  $\text{NaNbO}_3$ -based lead-free ceramics. *Appl Phys Lett* 2014;104:052903.
- [217] Guo H, Tan X. Direct observation of the recovery of an antiferroelectric phase during polarization reversal of an induced ferroelectric phase. *Phys Rev B* 2015;91(1–6):144104.

- [218] Zhao W, Zuo R, Zheng D, Li L. Dielectric Relaxor Evolution and Frequency-Insensitive Giant Strains in  $(\text{Bi}_{0.5}\text{Na}_{0.5})\text{TiO}_3$ -Modified  $\text{Bi}(\text{Mg}_{0.5}\text{Ti}_{0.5})\text{O}_3$ - $\text{PbTiO}_3$  Ferroelectric Ceramics. *J Am Ceram Soc* 2014;97(6):1855–60.
- [219] Groh C, Jo W, Rodel J. Frequency and temperature dependence of actuating performance of  $\text{Bi}_{1/2}\text{Na}_{1/2}\text{TiO}_3$ - $\text{BaTiO}_3$  based relaxor/ferroelectric composites. *J Appl Phys* 2014;115:234017.
- [220] Royles AJ, Bell AJ, Daniels JE, Milne SJ, Comyn TP. Observation of a time-dependent structural phase transition in potassium sodium bismuth titanate. *Appl Phys Lett* 2011;98:182904.
- [221] Lee KY, Shi X, Kumar N, Ho M, Etter M, Checchia S, et al. Electric-Field-Induced Phase Transformation and Frequency-Dependent Behavior of Bismuth Sodium Titanate-Barium Titanate. *Materials* 2020;13:1054.
- [222] Zhang M, McKinnon RA, Viola G, Yang B, Zhang D, Reece MJ, Abrahams I, Yan H. Ultrafast Electric Field-Induced Phase Transition in Bulk  $\text{Bi}_0.5\text{Na}_0.5\text{TiO}_3$  under High-Intensity Terahertz Irradiation. *ACS Photonics*; <https://dx.doi.org/10.1021/acsp Photonics.0c01559>.
- [223] Shi J, Fan H, Liu X, Li Q. Ferroelectric hysteresis loop scaling and electric-field-induced strain of  $\text{Bi}_{0.5}\text{Na}_{0.5}\text{TiO}_3$ - $\text{BaTiO}_3$  ceramics. *Phys Status Solidi A* 2014; 211:2388–93.
- [224] Wang C-M, Lau K, Wang Q. Dynamic hysteresis and scaling behaviours of lead-free  $0.94\text{Bi}_{0.5}\text{Na}_{0.5}\text{TiO}_3$ - $0.06\text{BaTiO}_3$  bulk ceramics. *RSC Adv* 2016;6(36): 30148–53.
- [225] Peng P, Nie HC, Liu Z, Wang G, Dong X, Zhang Y, et al. Scaling behavior for  $(\text{Bi}_{0.5}\text{Na}_{0.5})\text{TiO}_3$  based lead-free relaxor ferroelectric ceramics. *J Appl Phys* 2017; 122:064102.
- [226] Wang J, Zhou C, Li Q, Zeng W, Xu J, Chen G, et al. Unusual dynamic polarization response and scaling behaviors in  $\text{Bi}_{1/2}\text{Na}_{1/2}\text{TiO}_3$  ceramics. *Mater Res Bull* 2019;109:134–40.
- [227] Sapper E, Schaab S, Jo W, Granzow T, Rödel J. Influence of electric fields on the depolarization temperature of Mn-doped  $(1-x)\text{Bi}_{1/2}\text{Na}_{1/2}\text{TiO}_3$ - $x\text{BaTiO}_3$ . *J Appl Phys* 2012;111:014105.
- [228] Dul'kin E, Tiagunova J, Mojaev E, Roth M. Non-trivial behavior of the low temperature maximum of dielectric constant and location of the end critical point in  $\text{Na}_{0.5}\text{Bi}_{0.5}\text{TiO}_3$ - $0.06\text{BaTiO}_3$  lead free relaxor ferroelectrics crystals detected by acoustic emission. *J Appl Phys* 2018;123(4):044103.
- [229] Raevski IP, Prosandeev SA, Emelyanov AS, Raevskaya SI, Colla EV, Viehland D, et al. Bias-field effect on the temperature anomalies of dielectric permittivity in  $\text{PbMg}_{1/3}\text{Nb}_{2/3}\text{O}_3$ - $\text{PbTiO}_3$  single crystals. *Phys Rev B* 2005;72:184104.
- [230] Ma C, Guo H, Beckman SP, Tan X. Creation and destruction of morphotropic phase boundaries through electrical poling: a case study of lead-free  $(\text{Bi}_{1/2}\text{Na}_{1/2})\text{TiO}_3$ - $\text{BaTiO}_3$  piezoelectrics. *Phys Rev Lett* 2012;109(10):107602.
- [231] Guo H, Ma C, Liu X, Tan X. Electrical poling below coercive field for large piezoelectricity. *Appl Phys Lett* 2013;102:092902.
- [232] Damjanovic D. Hysteresis in piezoelectric and ferroelectric materials *The Science of Hysteresis*, edited by I. Mayergoyz and G Bertotti 2006;3:337–465.
- [233] Hall DA. Review Nonlinearity in piezoelectric ceramics. *J Mater Sci* 2001;36:4575–601.
- [234] Ma B, Hu Z, Liu S, Tong S, Narayanan M, Koritala RE, et al. Temperature-dependent dielectric nonlinearity of relaxor ferroelectric  $\text{Pb}_{0.92}\text{La}_{0.08}\text{Zr}_{0.52}\text{Ti}_{0.48}\text{O}_3$  thin films. *Appl Phys Lett* 2013;102:202901.
- [235] Cai BY, Schwarzkopf J, Hollmann E, Braun D, Schmidbauer M, Grellmann T, et al. Electronic characterization of polar nanoregions in relaxor-type ferroelectric  $\text{NaNbO}_3$  films. *Phys Rev B* 2015;93:224107.
- [236] Shetty S, Damodaran A, Wang K, Yuan Y, Gopalan V, Martin L, et al. Relaxor Behavior in Ordered Lead Magnesium Niobate. *Adv Funct Mater* 2019;29: 1804258.
- [237] Tagantsev AK, Glazunov AE. Mechanism of polarization response and dielectric non-linearity of  $\text{PbMg}_{1/3}\text{Nb}_{2/3}\text{O}_3$  relaxor ferroelectric. *Phase Transitions* 1998; 65(1–4):117–39.
- [238] Viola G, Tan Y, McKinnon RA, Wei X, Yan H, Reece MJ. Short range polar state transitions and deviation from Rayleigh-type behaviour in  $\text{Bi}_{0.5}\text{Na}_{0.5}\text{TiO}_3$ -based perovskites. *Appl Phys Lett* 2014;105:102906.
- [239] Dai Y, Schubert J, Hollmann E, Wördenweber R. Electric field induced relaxor behavior in anisotropically strained  $\text{SrTiO}_3$  films. *Phys B* 2016;485:78–83.
- [240] Zhang HB, Jiang SL, Kajiyoshi K. Nonlinear dielectric properties of  $(\text{Bi}_0.5\text{Na}_0.5)\text{TiO}_3$ -based lead-free piezoelectric thick films. *Appl Phys Lett* 2011;98:072908.
- [241] Huang JQ, Zhang YY, Jiang HC, Fan PY, Xiao JZ, Zhang HB. Non-180 degrees domain contributions in  $\text{Bi}_{0.5}(\text{Na}_{0.82}\text{K}_{0.18})_{0.5}\text{TiO}_3$  lead-free piezoelectric thick films. *Ceram Int* 2015;41:10506–11.
- [242] Qiao XS, Chen XM, Lian HL, Chen WT, Zhou JP, Liu P. Microstructure and Electrical Properties of Nonstoichiometric  $0.94(\text{Na}_{0.5}\text{Bi}_{0.5+x})\text{TiO}_3$ - $0.06\text{BaTiO}_3$  Lead-Free Ceramics. *J Am Ceram Soc* 2016;99:198–205.
- [243] Wang T, Chen XM, Qiu YZ, Lian HL, Chen WT. Microstructure and electrical properties of  $(1-x)[0.8\text{Bi}_{0.5}\text{Na}_{0.5}\text{TiO}_3$ - $0.2\text{Bi}_{0.5}\text{K}_{0.5}\text{TiO}_3$ ]- $x\text{BiCoO}_3$  lead-free ceramics. *Mater Chem Phys* 2017;186:407–14.
- [244] Wu J, Sun W, Meng N, Zhang H, Koval V, Yan Zhang Y, et al. Terahertz Probing Irreversible Phase Transitions Related to Polar Clusters in  $\text{Bi}_{0.5}\text{Na}_{0.5}\text{TiO}_3$ -Based Ferroelectric. *Adv Electron Mater* 2020;6(1901373).
- [245] Zhou D, Kamlah M. Determination of room-temperature creep of soft lead zirconate titanate piezoceramics under static electric fields. *J Appl Phys* 2005;98: 104107.
- [246] Zhou D, Kamlah M. Room-temperature creep of soft PZT under static electrical and compressive stress loading. *Acta Mater* 2006;54:1389–96.
- [247] Liu QD, Huber JE. Creep in ferroelectrics due to unipolar electrical loading. *J Eur Ceram Soc* 2006;26:2799–806.
- [248] Viola G, Chong KB, Guiu F, Reece MJ. Role of internal field and exhaustion in ferroelectric switching. *J Appl Phys* 2014;115(3):034106.
- [249] Chen D, Ayrikyan A, Webber KG, Kamlah M. Time-dependent electromechanical response of  $0.93(\text{Na}_{1/2}\text{Bi}_{1/2})\text{TiO}_3$ - $0.07\text{BaTiO}_3$  lead-free piezoceramic under constant electric field. *J Appl Phys* 2017;121:114106.
- [250] Liu QD, Fleck NA, Huber JE, Chu DP. Birefringence measurements of creep near an electrode tip in transparent PLZT. *J Eur Ceram Soc* 2009;29:2289–96.
- [251] Daniels JE, Majkut M, Cao Q, Schmidt S, Wright JP, Oddershede J. Heterogeneous grain-scale response in ferroic polycrystals under electric field. *Sci Rep* 2016; 6:22820.
- [252] Ormstrup J, Makarovic M, Majkut M, Rojac T, Walker J, Simons H. Dynamics and grain orientation dependence of the electric field induced phase transformation in Sm modified  $\text{BiFeO}_3$  ceramics. *J Mater Chem C* 2018;6(36):7635–41.
- [253] Acosta M, Schmitt LA, Molina-Luna L, Scherrer MC, Brilz M, Webber KG, et al. Core-shell lead-free piezoelectric ceramics: current status and advanced characterization of the  $\text{Bi}_{1/2}\text{Na}_{1/2}\text{TiO}_3$ - $\text{SrTiO}_3$  system. *J Am Ceram Soc* 2015;98(11):3405–22.
- [254] Liu N, Acosta M, Wang S, Xu BX, Stark RW, Dietz C. Revealing the core-shell interactions of a giant strain relaxor ferroelectric  $0.75\text{Bi}_{1/2}\text{Na}_{1/2}\text{TiO}_3$ - $0.25\text{SrTiO}_3$ . *Sci Rep* 2016;6:36910.
- [255] Glaum J, Zakhozheva M, Acosta M, Aksel E, Kleebe H, Hoffman M, et al. Influence of B-site disorder on the properties of unpoled  $\text{Bi}_{1/2}\text{Na}_{1/2}\text{TiO}_3$ - $0.06\text{Ba}(\text{Zr},\text{Ti})_{1-x}\text{O}_3$  piezoceramics. *J Am Ceram Soc* 2016;99(8):2801–8.
- [256] Chen J, Wang Y, Zhang Y, Yang Y, Jin R. Giant electric-field-induced strain at room temperature in  $\text{LiNbO}_3$ -doped  $0.94(\text{Bi}_{0.5}\text{Na}_{0.5})\text{TiO}_3$ - $0.06\text{BaTiO}_3$ . *J Eur Ceram Soc* 2017;37(6):2365–71.
- [257] Acosta M, Schmitt LA, Cazorla C, Studer A, Zintler A, Glaum J, et al. Piezoelectricity and rotostriction through polar and non-polar coupled instabilities in bismuth-based piezoceramics. *Sci Rep* 2016;6:28742.
- [258] Haun MJ, Furman E, Halemene TR, Cross LE. Thermodynamic theory of the lead zirconate-titanate solid solution system, part IV: Tilting of the oxygen octahedra. *Ferroelectrics* 1989;99:55–62.
- [259] Gopalan V, Litvin DB. Rotation-reversal symmetries in crystals and handed structures. *Nat Mater* 2011;10:376–81.
- [260] Kitanaka Y, Hirano K, Ogino M, Noguchi Y, Miyayama M, Moriyoshi C, et al. Polarization twist in perovskite ferroelectrics. *Sci Rep* 2016;6:32216.
- [261] Kutnjak Z, Petzelt J, Blinc R. The giant electromechanical response in ferroelectric relaxors as a critical phenomenon. *Nature* 2006;441:956.
- [262] Novak N, Piric R, Kutnjak Z. Diffuse critical point in PLZT ceramics. *Europhys Lett* 2013;102:17003.
- [263] Weyland F, Acosta M, Koruza J, Breckner P, Rödel J, Novak N. Criticality: concept to enhance the piezoelectric and electrocaloric properties of ferroelectrics. *Adv Funct Mater* 2016;26(40):7326–33.

- [264] Weyland F, Zhang HB, Novak N. Enhancement of energy storage performance by criticality in lead-free relaxor ferroelectrics. *Phys Status Solidi RRL* 2018;12:1800165.
- [265] Nuffer J, Lupascu DC, Rödel J. Damage evolution in ferroelectric PZT induced by bipolar electric cycling. *Acta Mater* 2000;48:3783–94.
- [266] Hoffmann MJ, Hammer M, Endriss A, Lupascu DC. Correlation between microstructure, strain behavior, and acoustic emission of soft PZT ceramics. *Acta Mater* 2001;49:1301–10.
- [267] Hatano K, Kobayashi K, Hagiwara T, Shimizu H, Doshida Y, Mizuno Y. Polarization System and Phase Transition on (Li, Na, K)NbO<sub>3</sub> Ceramics. *Jpn J Appl Phys* 2010;49:09MD11.
- [268] Lupascu DC. Microcracking and discontinuous fast switching as acoustic emission sources in 8/65/35 and 9.5/65/35 PLZT relaxor ferroelectrics. *J Eur Ceram Soc* 2001;21:1429–32.
- [269] Zhou LJ, Lupascu DC, Zimmermann A, Zhang Y. Discontinuous switching in antiferroelectric ceramics monitored by acoustic emissions. *J Appl Phys* 2005;97:124106.
- [270] Lupascu DC, Utschig T, Shur VY, Shur AG. The dynamics of domain walls determined from acoustic emission measurements. *Ferroelectrics* 2003;290:207–15.
- [271] Lupascu DC, Hammer M. “Elastic Discontinuities During Switching of Ferroelectric Ceramics. *Phys Status Solid A-Appl Res* 2002;191(2):643–57.
- [272] Dul'kin E, Mojaev E, Roth M, Jo W, Granzow T. Acoustic emission study of domain wall motion and phase transition in (1-x-y)Bi<sub>0.5</sub>Na<sub>0.5</sub>TiO<sub>3</sub>-xBaTiO<sub>3</sub>-yK<sub>0.5</sub>Na<sub>0.5</sub>NbO<sub>3</sub> lead-free piezoceramics. *Scripta Mater* 2009; 60: 251–3.
- [273] Dulkin E, Suchanicz J, Kania A, Roth M. Peculiar Properties of Phase Transitions in Na<sub>0.5</sub>Bi<sub>0.5</sub>TiO<sub>3</sub>-xBaTiO<sub>3</sub> (0<x<6) Lead-free Relaxor Ferroelectrics Seen Via Acoustic Emission. *Mater Res* 2018;21(3):e20170953.
- [274] Glaum J, Hoffman M. Electric fatigue of lead-free piezoelectric materials. *J Am Ceram Soc* 2014;97(3):665–80.
- [275] Genenko YA, Glaum J, Hoffmann MJ, Albe K. Mechanisms of aging and fatigue in ferroelectrics. *Mater Sci Eng, B* 2015;192:52–82.
- [276] Luo Z, Granzow T, Glaum J, Jo W, Rödel J, Hoffman M. Effect of Ferroelectric Long-Range Order on the Unipolar and Bipolar Electric Fatigue in Bi<sub>1/2</sub>Na<sub>1/2</sub>TiO<sub>3</sub>-Based Lead-Free Piezoceramics. *J Am Ceram Soc* 2011;94(11):3927–33.
- [277] Guo H, Liu X, Rödel J, Tan X. Nanofragmentation of Ferroelectric Domains During Polarization Fatigue. *Adv Funct Mater* 2015;25:270–7.
- [278] Patterson EA, Cann DP. Bipolar piezoelectric fatigue of Bi(Zn<sub>0.5</sub>Ti<sub>0.5</sub>)O<sub>3</sub>-(Bi<sub>0.5</sub>K<sub>0.5</sub>)TiO<sub>3</sub>-(Bi<sub>0.5</sub>Na<sub>0.5</sub>)TiO<sub>3</sub> Pb-free ceramics. *Applied Physics Letters* 2012; 101:042905.
- [279] Kumar N, Cann DP. Electromechanical strain and bipolar fatigue in Bi(Mg<sub>1/2</sub>Ti<sub>1/2</sub>)O<sub>3</sub>-(Bi<sub>1/2</sub>K<sub>1/2</sub>)TiO<sub>3</sub>-(Bi<sub>1/2</sub>Na<sub>1/2</sub>)TiO<sub>3</sub> ceramics. *J Appl Phys* 2013;114:054102.
- [280] Simons H, Glaum J, Daniels JE, Studer AJ, Liess A, Rödel J, et al. Domain fragmentation during cyclic fatigue in 94%(Bi<sub>1/2</sub>Na<sub>1/2</sub>)TiO<sub>3</sub>-6%BaTiO<sub>3</sub>. *J Appl Phys* 2012;112:044101.
- [281] Hinterstein M, Schmitt LA, Hoelzel M, Jo W, Rödel J, Kleebe HJ, et al. Cyclic electric field response of morphotropic Bi<sub>1/2</sub>Na<sub>1/2</sub>TiO<sub>3</sub>-BaTiO<sub>3</sub> piezoceramics. *Appl Phys Lett* 2015;106:222904.
- [282] Ehmke M, Glaum J, Jo W, Granzow T, Rödel J. Stabilization of the Fatigue-Resistant Phase by CuO Addition in (Bi<sub>1/2</sub>Na<sub>1/2</sub>)TiO<sub>3</sub>-BaTiO<sub>3</sub>. *J Am Ceram Soc* 2011;94(8):2473–8.
- [283] Kumar N, Shi X, Jones J, Hoffman M. Electrical fatigue failure in (Na<sub>1/2</sub>Bi<sub>1/2</sub>)TiO<sub>3</sub>-BaTiO<sub>3</sub> relaxor ceramics. *J Am Ceram Soc* 2019;102:5997–6007.
- [284] Shi X, Kumar N, Hoffman M. Electrical fatigue in 0.94Na<sub>0.5</sub>Bi<sub>0.5</sub>TiO<sub>3</sub>-0.06BaTiO<sub>3</sub>: Influence of the surface layer. *Appl Phys Lett* 2020;117:022905.
- [285] Shi J, Tian W, Liu X, Fan H. Electric-field induced phase transition and fatigue behaviors of (Bi<sub>0.5+x/2</sub>Na<sub>0.5-x/2</sub>)<sub>0.94</sub>Ba<sub>0.06</sub>Ti<sub>1-x</sub>Fe<sub>x</sub>O<sub>3</sub> ferroelectrics. *J Am Ceram Soc* 2017;100:1080–90.
- [286] Kong Y, Li X, Li Z, Hao J. Temperature independent fatigue-free behavior in sodium bismuth titanate-based lead-free ceramics. *Scr Mater* 2021;194:113678.
- [287] Shi X, Kumar N, Hoffman M. Electrical fatigue behavior of NBT-BT-xKNN ferroelectrics: effect of ferroelectric phase transformations and oxygen vacancies. *J Mater Chem C* 2020;8:3887.
- [288] Gao F, Dong X, Mao C, Liu W, Zhang H, Yang L, et al. Energy-storage properties of 0.89Bi<sub>0.5</sub>Na<sub>0.5</sub>TiO<sub>3</sub>-0.06BaTiO<sub>3</sub>-0.05K<sub>0.5</sub>Na<sub>0.5</sub>NbO<sub>3</sub> lead-free antiferroelectric ceramics. *J Am Ceram Soc* 2011;94(12):4382–6.
- [289] Gao F, Dong X, Mao C, Cao F, Wang G. c/a Ratio-dependent energy-storage density in (0.9-x)Bi<sub>0.5</sub>Na<sub>0.5</sub>TiO<sub>3</sub>-xBaTiO<sub>3</sub>-0.1K<sub>0.5</sub>Na<sub>0.5</sub>NbO<sub>3</sub> ceramics. *J Am Ceram Soc* 2011;94(12):4162–4.
- [290] Viola G, Ning H, Reece MJ, Wilson R, Correia TM, Weaver P, et al. Reversibility in electric field-induced transitions and energy storage properties of bismuth-based perovskite ceramics. *J Phys D Appl Phys* 2012;45:355302.
- [291] Qiao X, Zhang F, Wu D, Chen B, Zhao X, Peng Z, et al. Superior comprehensive energy storage properties in Bi<sub>0.5</sub>Na<sub>0.5</sub>TiO<sub>3</sub>-based relaxor ferroelectric ceramics. *Chem Eng J* 2020;388:124158.
- [292] Huang Y, Guo Q, Hao H, Liu H, Zhang S. Tailoring properties of (Bi<sub>0.5</sub>Na<sub>0.47</sub>)TiO<sub>3</sub>-based dielectrics for energy storage applications. *J Eur Ceram Soc* 2019;39:4752–60.
- [293] Wu YC, Fan YZ, Liu NT, Peng P, Zhou MX, Yan SG, et al. Enhanced energy storage properties in sodium bismuth titanate-based ceramics for dielectric capacitor applications. *J Mater Chem C* 2019;7:6222–30.
- [294] Luo N, Han K, Zhuo F, Xu C, Zhang G, Liu L, et al. Aliovalent A-site engineered AgNbO<sub>3</sub> lead-free antiferroelectric ceramics toward superior energy storage density. *J Mater Chem A* 2019;7:14118–28.
- [295] Li F, Zhai JW, Shen B, Liu X, Zeng HR. Simultaneously high energy storage density and responsivity in quasi-hysteresis-free Mn-doped Bi<sub>0.5</sub>Na<sub>0.5</sub>TiO<sub>3</sub>-BaTiO<sub>3</sub>-(Sr<sub>0.7</sub>Bi<sub>0.2</sub>)TiO<sub>3</sub> ergodic relaxor ceramics. *Mater Res Lett* 2018;6:345–52.
- [296] Hu D, Pan ZB, Zhang X, Ye HR, He ZY, Wang MK, et al. Greatly enhanced discharge energy density and efficiency of novel relaxation ferroelectric BNT-BKT-based ceramics. *J Mater Chem C* 2020;8:591–601.
- [297] Wu JY, Mahajan A, Riekehr L, Zhang HF, Yang B, Meng N, et al. Perovskite Sr<sub>x</sub>(Bi<sub>1-x</sub>Na<sub>0.97-x</sub>Li<sub>0.03</sub>)<sub>0.5</sub>TiO<sub>3</sub> ceramics with polar nano regions for high power energy storage. *Nano Energy* 2018;50:723–32.
- [298] Li J, Li F, Xu Z, Zhang S. Multilayer Lead-Free Ceramic Capacitors with Ultrahigh Energy Density and Efficiency. *Adv Mater* 2018;30(32):1802155.
- [299] Wang H, Liu Y, Yang T, Zhang S. Ultrahigh energy-storage density in antiferroelectric ceramics with field-induced multiphase transitions. *Adv Funct Mater* 2019;29(7):1807321.
- [300] Hu Q, Wei X. Abnormal phase transition and polarization mismatch phenomena in BaTiO<sub>3</sub>-based relaxor ferroelectrics. *J Adv Dielectr* 2019;9:1930002.
- [301] Hu Q, Tian Y, Zhu Q, Bian J, Jin L, Du H, et al. Achieve ultrahigh energy storage performance in BaTiO<sub>3</sub>-Bi(Mg<sub>1/2</sub>Ti<sub>1/2</sub>)O<sub>3</sub> relaxor ferroelectric ceramics via nano-scale polarization mismatch and reconstruction. *Nano Energy* 2020;67:104264.
- [302] Li J, Shen Z, Chen X, Yang S, Zhou W, Wang M, et al. Grain-orientation-engineered multilayer ceramic capacitors for energy storage applications. *Nat Mater* 2020;19:999–1005.
- [303] Zhang ST, Kounga AB, Aulbach E. Giant strain in lead-free piezoceramics Bi<sub>0.5</sub>Na<sub>0.5</sub>TiO<sub>3</sub>-BaTiO<sub>3</sub>-K<sub>0.5</sub>Na<sub>0.5</sub>NbO<sub>3</sub>. *Appl Phys Lett* 2007;91:112906.
- [304] Lee DS, Jeong SJ, Kim MS, Kim KH. Effect of sintering time on strain in ceramic composite consisting of 0.94Bi<sub>0.5</sub>(Na<sub>0.75</sub>K<sub>0.25</sub>)<sub>0.5</sub>TiO<sub>3</sub>-0.06BiAlO<sub>3</sub> with (Bi<sub>0.5</sub>Na<sub>0.5</sub>)TiO<sub>3</sub>. *Jpn J Appl Phys* 2013;52:021801.
- [305] Su Lee D, Jong Jeong S, Soo Kim M, Hyuk Koh J. Electric field induced polarization and strain of Bi-based ceramic composites. *J Appl Phys* 2012;112:124109.
- [306] Groh C, Jo W, Rödel J. Tailoring Strain Properties of (0.94-x)Bi<sub>1/2</sub>Na<sub>1/2</sub>TiO<sub>3</sub>-0.06BaTiO<sub>3</sub>-xK<sub>0.5</sub>Na<sub>0.5</sub>NbO<sub>3</sub> Ferroelectric/Relaxor Composites. *J Am Ceram Soc* 2014;97(5):1465–70.
- [307] Groh C, Jo W, Rödel J. Frequency and temperature dependence of actuating performance of Bi<sub>1/2</sub>Na<sub>1/2</sub>TiO<sub>3</sub>-BaTiO<sub>3</sub> based relaxor/ferroelectric composites. *J Appl Phys* 2014;115:234107.
- [308] Groh C, Franzbach DJ, Jo W, Webber KG, Kling J, Schmitt LA, et al. Relaxor/ferroelectric composites: a solution in the quest for practically viable lead-free incipient piezoceramics. *Adv Funct Mater* 2014;24:356–62.
- [309] Li H, Liu Q, Zhou J, Wang K, Li J, Liu H, et al. Grain size dependent electrostrain in Bi<sub>1/2</sub>Na<sub>1/2</sub>TiO<sub>3</sub>-SrTiO<sub>3</sub> incipient piezoceramics. *J Eur Ceram Soc* 2016;36(11):2849–53.

G. Viola et al.

- [310] Cheng R, Xu Z, Chua R, Hao J, Du J, Li G. Electric field-induced ultrahigh strain and large piezoelectric effect in  $\text{Bi}_{1/2}\text{Na}_{1/2}\text{TiO}_3$ -based leadfree piezoceramics. *J Eur Ceram Soc* 2016;36:489–96.
- [311] Wu J, Zhang H, Huang CH, Tseng CW, Meng N, Koval V, et al. Ultrahigh field-induced strain in lead-free ceramics. *Nano Energy* 2020;76:105037.
- [312] Scott JF. Electrocaloric materials. *Annu Rev Mater Res* 2011;41:229–40.
- [313] Kumar A, Thakre A, Jeong DY, Ryu J. Prospects and challenges of the electrocaloric phenomenon in ferroelectric ceramics. *J Mater Chem C* 2019;7:6836–59.
- [314] Le Goupil F, Alford NM. Upper limit of the electrocaloric peak in lead-free ferroelectric relaxor ceramics. *APL Mater* 2016;4:064104.
- [315] Le Goupil F, McKinnon R, Koval V, Viola G, Dunn S, Berenov A, et al. Tuning the electrocaloric enhancement near the morphotropic phase boundary in lead-free ceramics. *Sci Rep* 2016;6:28251.
- [316] Li F, Lu B, Zhai J, Shen B, Zeng H, Lu S, et al. Enhanced piezoelectric properties and electrocaloric effect in novel lead-free  $(\text{Bi}_{0.5}\text{K}_{0.5})\text{TiO}_3\text{-La}(\text{Mg}_{0.5}\text{Ti}_{0.5})\text{O}_3$  ceramics. *J Am Ceram Soc* 2018;101:5503–13.
- [317] Fan Z, Liu X, Tan X. Large electrocaloric responses in  $[\text{Bi}_{1/2}(\text{Na}, \text{K})_{1/2}]\text{TiO}_3$ -based ceramics with giant electro-strains. *J Am Ceram Soc* 2017;100:2088–97.
- [318] Pu Y, Zhang Q, Li R, Chen M, Du X, Zhou S. Dielectric properties and electrocaloric effect of high-entropy  $(\text{Na}_{0.2}\text{Bi}_{0.2}\text{Ba}_{0.2}\text{Sr}_{0.2}\text{Ca}_{0.2})\text{TiO}_3$  ceramic. *Appl Phys Lett* 2019;115:223901.
- [319] Shionoya S. Photoluminescence. In: *Luminescence of Solids*; Plenum Press: New York, NY, USA, 1998; 95-133.
- [320] Khatua DK, Kalaskar A, Ranjan R. Tuning photoluminescence response by electric field in the lead-free piezoelectric  $\text{Na}_{1/2}\text{Bi}_{1/2}\text{TiO}_3\text{-BaTiO}_3$ . *Phys Rev Lett* 2016;116:117601.
- [321] Hu B, Pan Z, Dai M. Photoluminescence and Temperature Dependent Electrical Properties of Er-Doped  $0.94\text{Bi}_{0.5}\text{Na}_{0.5}\text{TiO}_3\text{-}0.06\text{BaTiO}_3$  Ceramics. *J Am Ceram Soc* 2015;97:3877–82.
- [322] Khatua DK, Agarwal A, Kumar N, Ranjan R. Probing local structure of the morphotropic phase boundary composition of  $\text{Na}_{0.5}\text{Bi}_{0.5}\text{TiO}_3\text{-BaTiO}_3$  using rare-earth photoluminescence as a technique. *Acta Mater* 2018;145:429–36.
- [323] Kalaskar A, Rao BN, Thomas T, Ranjan R. Electric field induced short range to long range structural ordering and its influence on the  $\text{Eu}^{+3}$  photoluminescence in the lead-free ferroelectric  $\text{Na}_{1/2}\text{Bi}_{1/2}\text{TiO}_3$ . *J Appl Phys* 2015;117:244106.
- [324] Yi D, Wang Y, van 't Erve OMJ, Xu L, Yuan H, Veit MJ, et al. Emergent Electric Field Control of Phase Transformation in Oxide Superlattices. *Nature Commun* 2020;11:902.
- [325] Li W, Shi J, Zhang KHL, MacManus-Driscoll JL. Defects in complex oxide thin films for electronics and energy applications: challenges and opportunities. *Mater Horiz* 2020;7:2832–59.
- [326] Ning S, Zhang Q, Occhialini C, Comin R, Zhong X, Ross CA. Voltage Control of Magnetism above Room Temperature in Epitaxial  $\text{SrCo}_{1-x}\text{Fe}_x\text{O}_{3-\delta}$ . *ACS Nano* 2020;14(7):8949–57.